

AD-A124 305

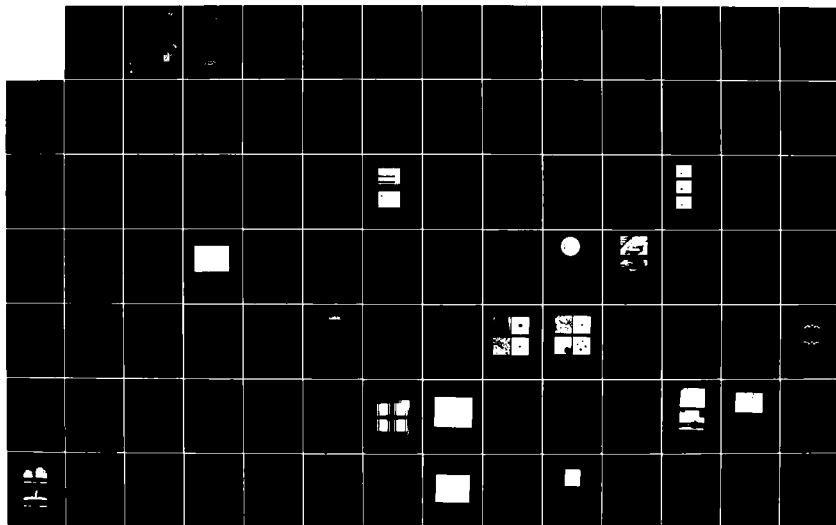
SOLID STATE RESEARCH(U) MASSACHUSETTS INST OF TECH
LEXINGTON LINCOLN LAB A L MCWORTER 22 NOV 82 1982-3
ESD-TR-82-086 F19828-80-C-0002

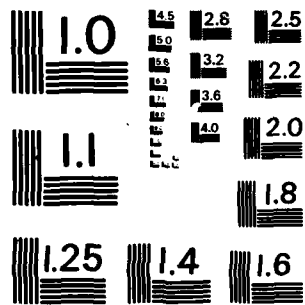
1/2

UNCLASSIFIED

F/O 20/12

NL





MICROCOPY RESOLUTION TEST CHART
NATIONAL BUREAU OF STANDARDS-1963-A

1

ADA 124305

Solid State Research

1982

DTIC



**MASSACHUSETTS INSTITUTE OF TECHNOLOGY
LINCOLN LABORATORY**

SOLID STATE RESEARCH

QUARTERLY TECHNICAL SUMMARY REPORT

1 MAY — 31 JULY 1982

ISSUED 22 NOVEMBER 1982

Approved for public release; distribution unlimited.

LEXINGTON

MASSACHUSETTS

ABSTRACT

This report covers in detail the solid state research work of the Solid State Division at Lincoln Laboratory for the period 1 May through 31 July 1982. The topics covered are solid state device research, quantum electronics, materials research, microelectronics, and analog device technology. Funding is primarily provided by the Air Force, with additional support provided by the Army, DARPA, Navy, NASA, and DOE.

Accession For	
NTIS GRA&I	<input checked="" type="checkbox"/>
DTIC TAB	<input type="checkbox"/>
Unannounced	<input type="checkbox"/>
Justification	
By	
Distribution/	
Availability Codes	
Dist	Availability
A	



CONTENTS

Abstract	iii
Summary	vii
Reports on Solid State Research	xi
Organization	xix
 1. SOLID STATE DEVICE RESEARCH	 1
1.1 Coherently Coupled Waveguide Bends	1
1.2 Effect of Threading Dislocations on the Dark Current of InP APDs	5
1.3 Spatial Light Modulation Using Electroabsorption in a GaAs Charge-Coupled Device	9
 2. QUANTUM ELECTRONICS	 11
2.1 Simultaneous Heterodyne and Direct Detection CO ₂ Lidar Measurements	11
2.2 Ti:Al ₂ O ₃ - A New Solid State Tunable Laser	15
2.3 Laser Microchemical Deposition of Conducting Links for Restructurable VLSI	21
2.4 Single Mode Waveguide Multiplication and Mixing at Submillimeter Frequencies	27
 3. MATERIALS RESEARCH	 29
3.1 Lateral Epitaxial Overgrowth of GaAs by Organometallic Chemical Vapor Deposition	29
3.2 Liquid-Encapsulated Czochralski Growth of InP Crystals from In-Rich Melts	35
3.3 Simultaneous Formation of a Shallow Silicon p-n Junction and a Shallow Silicide/Silicon Ohmic Contact by an Ion Implantation Technique	40
3.4 Effects of Ionizing Radiation on n-Channel MOSFETs Fabricated in Zone-Melting-Recrystallized Si Films on SiO ₂ -Coated Si Substrates	48

4.	MICROELECTRONICS	55
4.1	Charge-Coupled Devices: Time-Integrating Correlator	55
4.2	Dry Etching of Gold Using SF ₆	58
5.	ANALOG DEVICE TECHNOLOGY	67
5.1	MNOS Nonvolatile Analog Memory	67
5.2	Low Loss Substrates for Superconductive Circuits	74
5.3	Considerations for an Integrated Optical Spectrum Analyzer (IOSA)	80

SUMMARY

1. SOLID STATE DEVICE RESEARCH

Low bending losses have been achieved in single-mode Ti:LiNbO_3 channel waveguides by utilizing coherent coupling effects between closely spaced abrupt bends. Losses as low as 0.08 dB per coupled 1° abrupt bend, as compared with 0.8 dB per isolated 1° abrupt bend, have been measured. Low-loss waveguide bends are needed for the efficient interconnection of optical components in integrated optical circuits.

Threading dislocations were found not to influence the dark current of high-performance InP avalanche photodiodes formed using liquid phase epitaxially grown $n\text{-p}^+$ junctions on moderate-dislocation-density substrates. This result is in marked contrast to the previously reported effect of dislocations on diodes formed by diffused junctions. It is hypothesized that when the junction is formed by diffusion, the dislocations act as channels for enhanced diffusion.

High-speed one- and two-dimensional light modulation may be carried out using the electroabsorption (Franz-Keldysh) effect in a GaAs buried channel charge-coupled device (CCD). For photon energies slightly lower than the energy gap, the transmission through or along the surface of a CCD structure may be controlled by the signal charge in the wells through the change of electric field with charge. Experimental measurements on a GaAs CCD structure designed with semitransparent gates have verified the predicted performance.

2. QUANTUM ELECTRONICS

A dual-wavelength, dual- CO_2 -laser, differential-absorption LIDAR system has been developed which permits simultaneous heterodyne detection and direct detection of the same LIDAR returns. Differences in signal-to-noise ratios and statistical and temporal characteristics for LIDAR returns from topographic targets have been measured.

A new, high-gain, solid-state tunable laser, $\text{Ti:Al}_2\text{O}_3$, has been demonstrated. Pulsed operation with up to 1 mJ of output energy and tuning from 718 to 770 nm have been observed.

Preliminary experiments have been conducted to adapt recently developed laser direct-write techniques to the discretionary deposition of conducting links in VLSI circuits. Both photochemical and thermal laser-deposition techniques have produced low-resistance links on simple single-level, metal-gap structures.

In order to generate tunable radiation at power levels suitable for use as a heterodyne local oscillator, a submillimeter crossed-guide frequency doubler has been developed which operates up to 600 GHz in the fundamental mode. This doubler also yields excellent performance when used for both harmonic and fundamental mixing.

3. MATERIALS RESEARCH

In the first demonstration of lateral epitaxial overgrowth by organometallic chemical vapor deposition (OMCVD), ratios of lateral-to-vertical growth rates greater than five have been achieved for the deposition of GaAs. To show the applicability of OMCVD to the CLEFT (cleavage of lateral epitaxial films for transfer) process, a continuous epitaxial GaAs layer 3 μm thick has been grown over a patterned mask on a GaAs substrate, then bonded to a glass substrate, and cleaved intact from the GaAs substrate.

Nominally undoped, n-type crystals of InP grown by the liquid-encapsulated Czochralski method from In-rich melts exhibit a marked decrease in carrier concentration and increase in mobility at 77 K compared with those grown from stoichiometric melts. Measurements of the Hall coefficient at room temperature as a function of magnetic field up to 15 T indicate that this improvement in electrical properties is due to a reduction in donor concentration rather than to measurement anomalies resulting from the presence of In inclusions.

An ion-implantation technique has been developed for use in the fabrication of metal-oxide-semiconductor field-effect transistors (MOSFETs) for large-scale integrated circuits. In an initial demonstration of this technique, a p-type wafer was coated with a thin layer of W and then with alternating layers of Si and W, after which it was implanted with As^+ ions. Thermal annealing produced a shallow WSi_2/Si ohmic contact and simultaneously activated the implanted As donors to form a shallow p-n junction located directly below the contact.

A study has been made of the effects of irradiation with 1.5-MeV electrons and Co-60 γ -rays on the electrical characteristics of n-channel MOSFETs, with either complete-island-etch or local-oxidation-of-Si isolation, that were fabricated in zone-melting-recrystallized Si films on SiO_2 -coated Si substrates. As in a previous study, which was limited to electron irradiation of complete-island-etch devices, it was found that radiation effects can be largely suppressed by applying a moderate negative bias to the substrates during irradiation and device operation.

4. MICROELECTRONICS

An all-CCD time-integrating correlator has been built by combining on a single chip binary-analog charge multiplication, charge integration, and subtraction of the integrated bias charge. All the design functions of the chip have been verified at a 5-MHz clock rate; modifications of the chip layout will be made to achieve the 25-MHz clock rate potential of the CCD.

Sulfur hexafluoride has been used in a reactive ion etching system to etch both Au and GaAs. Straight walls with no undercut are achieved when etching Au with SF_6 at lower power densities and bias levels than with Ar sputter etching, and the resulting etched surfaces are smoother for SF_6 etching. Minimal damage is introduced to etched GaAs when using SF_6 , as evidenced by ideality factor measurements on diodes fabricated on etched and unetched surfaces.

5. ANALOG DEVICE TECHNOLOGY

Test results on 32-sample MNOS/CCD nonvolatile analog memories show that the devices immediately after writing are linear over a 5-V window with an rms fixed pattern deviation of 28 mV, thus providing a 39-dB linear dynamic range. After 10^5 erase/write (E/W) cycles, signal retention is unchanged, but significant degradation occurs after 10^7 E/W cycles. Design, fabrication, and initial testing of a 256-sample MNOS/CCD analog memory have also been carried out.

To fully realize the potential of superconductive microwave filters for analog signal processing, there has been a need for a rugged, readily available, isotropic substrate material having a very low ($<10^{-4}$) dielectric loss tangent and low dispersion at 1- to 10-GHz frequencies. Measurements of niobium-on-silicon stripline resonators have shown that the silicon substrate possesses all the desirable properties.

An improved configuration for an integrated optical spectrum analyzer is proposed which utilizes an amplitude-weighted, oblique-incidence-grating input lens, a bulk-acoustic-wave Bragg cell excited by a quadrature-fed planar phased array, a Fresnel output lens, and an integrated Si detector array that is fed through channel waveguides. The optical energy is confined by low-loss glass waveguides on passivated Si except in the Bragg cell.

REPORTS ON SOLID STATE RESEARCH

15 May through 15 August 1982

PUBLISHED REPORTS

Journal Articles

<u>JA No.</u>			
5250	A Calculation of the Capacitance-Voltage Characteristics p^+ -InP/n-InGaAsP Photodiodes	J.P. Donnelly	Solid-State Electron. <u>25</u> , 669 (1982)
5274	Photodeposition of Metal Films with Ultraviolet Laser Light	D.J. Ehrlich R.M. Osgood, Jr. T.F. Deutsch	J. Vac. Sci. Technol. <u>21</u> , 23 (1982)
5305	Amorphous-Crystalline Boundary Dynamics in cw Laser Crystallization	H.J. Zeiger J.C.C. Fan B.J. Palm R.L. Chapman R.P. Gale	Phys. Rev. B <u>25</u> , 4002 (1982)
5314	Laser Remote Sensing of Hydrazine, MMH, and UDMH Using a Differential-Absorption CO ₂ Laser	N. Menyuk D.K. Killinger W.E. DeFeo	Appl. Opt. <u>21</u> , 2275 (1982)
5316	Tantalum Oxide Capacitors for GaAs Monolithic Integrated Circuits	M.E. Elta A. Chu L.J. Mahoney R.T. Cerretani W.E. Courtney	IEEE Electron Device Lett. <u>EDL-3</u> , 127 (1982)
5319	Microsecond Carrier Lifetimes in Films Prepared on SiO ₂ -Coated Si Substrates by Zone-Melting Recrystallization and by Subsequent Epitaxial Growth	B-Y. Tsaur J.C.C. Fan M.W. Geis	Appl. Phys. Lett. <u>41</u> , 83 (1982)
5325	Integrated Optical Temperature Sensor	L.M. Johnson F.J. Leonberger G.W. Pratt*	Appl. Phys. Lett. <u>41</u> , 134 (1982)
5328	Stimulated Surface-Plasma-Wave Scattering and Growth of a Periodic Structure in Laser-Photodeposited Metal Films	S.R.J. Brueck D.J. Ehrlich	Phys. Rev. Lett. <u>48</u> , 1678 (1982)
5330	Zone-Melting Recrystallization of 3-in.-diam Si Films on SiO ₂ -Coated Si Substrates	J.C.C. Fan B-Y. Tsaur R.L. Chapman M.W. Geis	Appl. Phys. Lett. <u>41</u> , 186 (1982)

*Author not at Lincoln Laboratory.

<u>JA No.</u>			
5341	Submicrometer-Linewidth Doping and Relief Definition in Silicon by Laser-Controlled Diffusion	D.J. Ehrlich J.Y. Tsao	Appl. Phys. Lett. <u>41</u> , 297 (1982)
5342	Effects of Ionizing Radiation on n-Channel MOSFET's Fabricated in Zone-Melting-Recrystallized Si Films on SiO ₂	B-Y. Tsaur J.C.C. Fan G.W. Turner D.J. Silversmith	IEEE Electron Device Lett. <u>EDL-3</u> , 195 (1982)
5344	Direct-Write Metallization of Silicon MOSFET's Using Laser Photodeposition	J.Y. Tsao D.J. Ehrlich D.J. Silversmith R.W. Mountain	IEEE Electron Device Lett. <u>EDL-3</u> , 164 (1982)
5355	Remote Sensing Conference Focuses on Technological Advances in Measurement	N. Menyuk	Laser Focus <u>18</u> , 12 (1982)
5364	Optically-Induced Microstructures in Laser Photodeposited Metal Films	R.M. Osgood, Jr. D.J. Ehrlich	Opt. Lett. <u>7</u> , 385 (1982)

Meeting Speeches

<u>MS No.</u>			
5760	Transient Heating with Graphite Heaters for Semiconductor Processing	J.C.C. Fan B-Y. Tsaur M.W. Geis	In <u>Laser and Electron-Beam Interactions with Solids</u> , B.R. Appleton and G.K. Celler, Eds. (Elsevier North Holland, Amsterdam, 1982), pp. 751-758
5763	Preparation of Oriented GaAs Bicrystal Layers by Vapor-Phase Epitaxy Using Lateral Overgrowth	J.P. Salerno R.W. McClelland P. Vohl J.C.C. Fan W. Macropoulos C.O. Bozler A.F. Witt*	In <u>Grain Boundaries in Semiconductors</u> , H.J. Leamy, G.E. Pike, and C.H. Seager, Eds. (Elsevier North Holland, Amsterdam, 1982), p. 77
5767	Silicon-on-Insulator MOSFETs Fabricated in Zone-Melting-Recrystallized Poly-Si Films on SiO ₂	B-Y. Tsaur M.W. Geis J.C.C. Fan D.J. Silversmith R.W. Mountain	In <u>Laser and Electron-Beam Interactions with Solids</u> , B.R. Appleton and G.K. Celler, Eds. (Elsevier North Holland, Amsterdam, 1982), pp. 585-590
5899A	Raman Scattering as a Probe of Thin-Films	S.R.J. Brueck	Proc. Workshop on Diamond Like Carbon Coatings, Albuquerque, New Mexico, 19-20 April 1982

*Author not at Lincoln Laboratory.

MS No.

- | | | | |
|------|---|---|---|
| 5925 | Heterodyne Experiments from Millimeter Wave to Optical Frequencies Using GaAs MESFETs Above f_T | A. Chu
H.R. Fetterman
D.D. Peck
P.E. Tannenwald | Microwave and Millimeter Wave Symposium Digest, Dallas, Texas, 16-18 June 1982, p. 25 |
| 5927 | A Two-Stage Monolithic IF Amplifier Utilizing a Ta_2O_5 Capacitor | A. Chu
L.J. Mahoney
M.E. Elta
W.E. Courtney
M.C. Finn
W.J. Piacentini
J.P. Donnelly | Microwave and Millimeter Wave Symposium Digest, Dallas, Texas, 16-18 June 1982, p. 61 |

* * * * *

UNPUBLISHED REPORTS

Journal ArticlesJA No.

- | | | | |
|------|---|--|---|
| 5346 | Low-Dislocation-Density GaAs Epilayers Grown on Ge-Coated Si Substrates by Means of Lateral Epitaxial Overgrowth | B-Y. Tsauro
R.W. McClelland
J.C.C. Fan
R.P. Gale
J.P. Salerno
B.A. Vojak
C.O. Bozler | Accepted by Appl. Phys. Lett. |
| 5347 | High-Speed UV- and X-Ray-Sensitive InP Photoconductive Detectors | T.F. Deutsch
F.J. Leonberger
A.G. Foyt
D. Mills* | Accepted by Appl. Phys. Lett. |
| 5352 | Graphoepitaxy of Germanium on Gratings with Square Wave and Sawtooth Profiles | M.W. Geis
B-Y. Tsauro
D.C. Flanders | Accepted by Appl. Phys. Lett. |
| 5354 | Deep-UV Spatial-Period-Division Using an Excimer Laser | A.M. Hawryluk*
H.I. Smith*
R.M. Osgood, Jr.*
D.J. Ehrlich | Accepted by Opt. Lett. |
| 5361 | Limitations of Signal Averaging Due to Temporal Correlation in Laser Remote Sensing Measurements | N. Menyuk
D.K. Killinger
C.R. Menyuk* | Accepted by Appl. Opt. |
| 5362 | Analysis of Integrated-Optics Y-Junction and Mach-Zehnder Interferometric Modulator Using Four-Port Scattering Matrix | R.H. Rediker
F.J. Leonberger | Accepted by IEEE J. Quantum Electron., Special Issue Guided-Wave Technology |

*Author not at Lincoln Laboratory.

<u>JA No.</u>			
5363	Wideband Monolithic Acousto-electric Memory Correlators	R.A. Becker R.W. Ralston P.V. Wright	Accepted by IEEE Trans. Sonics Ultrason
5369	Spatial Light Modulation Using Electroabsorption in a GaAs CCD	R.H. Kingston B.E. Burke K.B. Nichols F.J. Leonberger	Accepted by Appl. Phys. Lett.
5370	Lateral Epitaxial Overgrowth of GaAs by Organometallic Chemical Vapor Deposition	R.P. Gale R.W. McClelland J.C.C. Fan C.O. Bozler	Accepted by Appl. Phys. Lett.
5377	Time-Resolved Measurements of Stimulated Surface Polarization Wave Scattering and Grating Formation in Pulsed-Laser-Annealed Germanium	D.J. Ehrlich S.R.J. Brueck J.Y. Tsao	Accepted by Appl. Phys. Lett.
5378	2-Bit 1 Gigasample/sec Electron-optic Guided-Wave Analog-to-Digital Converter	R.A. Becker F.J. Leonberger	Accepted by IEEE J. Quantum Electron.

Meeting Speeches[†]

<u>MS No.</u>			
5653C	Frequency Stability and Control Characteristics of (GaAl)As Semiconductor Lasers	A. Mooradian D. Welford	Frequency Control Symp., Philadelphia, Pennsylvania, 2-4 June 1982
5707H	Laser Photophysics of Surface Adlayers	D.J. Ehrlich T.F. Deutsch	XIIth International Quantum Electronics Conference, Munich, Germany, 22-25 June 1982
5805	Advances in Tunable Transition-Metal Lasers	P.F. Moulton	
5904	Optical Exclusive OR Gate	H.A. Haus* A. Lattes* E.P. Ippen* F.J. Leonberger	

*Author not at Lincoln Laboratory.

[†]Titles of Meeting Speeches are listed for information only. No copies are available for distribution.

MS No.			
5905	Doubly Degenerate Four-Wave Mixing in LiNbO_3 Waveguides	H.A. Haus* A. Lattes* C. Gabriel* E.P. Ippen* F.J. Leonberger	XIIth International Quantum Electronics Conference, Munich, Germany, 22-25 June 1982
5910	Fundamental Line Broadening Mechanisms of Single-Frequency CW (GaAl)As Diode Lasers	D. Welford A. Mooradian	
6018A	Stimulated Surface Plasma Waves and the Formulation of Periodic Structures by Laser Irradiation of Surfaces	D.J. Ehrlich S.R.J. Brueck J.Y. Tsao	
5805A	Advances in Tunable Transition-Metal Lasers	P.F. Moulton	SPIE Technical Symposium East, Arlington, Virginia 3-7 May 1982
5837	A High-Speed CCD Two-Dimensional Correlator	B.E. Burke A.M. Chiang W.H. McGonagle G.R. McCully J.F. Melia	
5883A	Performance Characteristics of a 4-Bit 828-Megasample/s Electrooptic Analog-to-Digital Converter	F.J. Leonberger R.A. Becker	
5821D	Millimeter-Wave Monolithic Circuits	A. Chu	IEEE Intl. Microwave Symp., Dallas, Texas, 15-17 June 1982
5908	Passive Superconducting Microwave Circuits for 2-20 GHz Bandwidth Analog Signal Processing	J.T. Lynch A.C. Anderson R.S. Withers P.V. Wright S.A. Reible	
5829A	Analog Processing with Superconducting Circuits	E. Stern	
5866A	MNOS/CCD Nonvolatile Analog Memory	R.W. Ralston R.S. Withers	Industrial Liaison Seminar, M.I.T., 20 May 1982
5869	Zone-Melting Recrystallization of Three-Inch-Diameter Silicon Films on SiO_2 -Coated Substrates	J.C.C. Fan R.L. Chapman B-Y. Tsaur M.W. Geis	The Electrochemical Society Mtg., Montreal, Canada 9-14 May 1982

*Author not at Lincoln Laboratory.

MS No.

5870	Properties of Zone-Melting-Recrystallized Si Films on Insulators	B-Y. Tsaur J.C.C. Fan M.W. Geis D.J. Silversmith R.W. Mountain	The Electrochemical Society Mtg., Montreal, Canada, 9-14 May 1982
5891	Dry Etching of Gold Using SF ₆	S.M. Cabral M.E. Elta A. Chu L.J. Mahoney	
5893	The Mechanism of Orientation of Si Graphoepitaxy Using a Strip-Heater Oven	H.I. Smith* M.W. Geis	
5919A	Remote Sensing of Hydrazine Compounds Using a Dual Mini-TEA CO ₂ Laser DIAL System	N. Menyuk D.K. Killinger W.E. DeFeo	JANAF Remote Sensing of Propellants, NBS, Washington, DC, 21 July 1982
5935	Limitations of Signal Averaging of DIAL Measurements Due to Temporal Correlation	N. Menyuk D.K. Killinger C.R. Menyuk*	11th International Laser Radar Conference, Madison Wisconsin, 21-25 June 1982
5946	Simultaneous Heterodyne and Direct Detection CO ₂ DIAL Measurements	D.K. Killinger N. Menyuk W.E. DeFeo	
5939	Lateral Epitaxial Growth of InP Over PSG Films for Oxide-Confined Optical Waveguides	P. Vohl F.J. Leonberger F.J. O'Donnell	Electronic Materials Conf., Ft. Collins, Colorado, 23-25 June 1982
5958	Direct-Write Metallization of Si MOSFETs Using Laser Photodeposition	J.Y. Tsao D.J. Ehrlich D.J. Silversmith R.W. Mountain	
5967	Zone-Melting-Recrystallized Si Films: Characteristics and Prospects for Device Applications	B-Y. Tsaur J.C.C. Fan M.W. Geis R.L. Chapman D.J. Silversmith R.W. Mountain G.W. Turner	
5976	Control of Subboundaries in Zone-Melting Recrystallized Si Films	M.W. Geis H.I. Smith* B-Y. Tsaur J.C.C. Fan D.J. Silversmith R.W. Mountain	

*Author not at Lincoln Laboratory.

MS No.			
5940	Laser Photochemical Processing for Microelectronics	D.J. Ehrlich T.F. Deutsch J.Y. Tsao	Industrial Liaison, Symp., M.I.T., 4 May 1982
5960A	Liquid-Phase Epitaxy	Z.L. Liao	Optical Information Systems, Inc., Elmsford, New York, 16 July 1982
6019	Atmospheric Transmission Measurement Limitations Due to Temporal Correlation	N. Menyuk D.K. Killinger C.R. Menyuk*	Annual Review Conf. on Atmospheric Transmission Models, Air Force Geophysics Laboratory, Hanscom AFB, Bedford, Massachusetts, 18-20 May 1982
6032	Buried Heterostructure GaInAsP/InP Lasers Fabricated Using Thermally Transported InP	Z.L. Liao J.N. Walpole	Device Research Conf., Ft. Collins, Colorado, 21-23 June 1982
6033	Heterodyne and Direct Detection at 10 μ m with High-Temperature p-Type HgCdTe Photoconductors	D.L. Spears	IRIS Specialty Group on IR Detectors, San Diego, California, 27-29 July 1982
6035	High-Quality Hg _{1-x} Cd _x Te Epilayers Grown by Open-Tube VPE	P. Vohl D.L. Spears	
6041	Effects of Ionizing Radiation on SOI MOSFETs Fabricated in Zone-Melting-Recrystallized Si Films	B-Y. Tsaur J.C.C. Fan G.W. Turner D.J. Silversmith	Nuclear and Space Radiation Effects Symp., Las Vegas, Nevada, 20-22 July 1982
6094	High-Efficiency Solar Cells	J.C.C. Fan	DOE Energy Research Advisory Panel, Solar Energy Research Institute, Golden, Colorado, 1 July 1982

*Author not at Lincoln Laboratory.

ORGANIZATION

SOLID STATE DIVISION

A.L. McWhorter, Head
I. Melngailis, Associate Head
J.F. Goodwin, Assistant

P.E. Tannenwald, Senior Staff
B. Lax, Visiting Scientist

QUANTUM ELECTRONICS

A. Mooradian, Leader
P.L. Kelley, Associate Leader

Barch, W.E.	Johnson, B.C.*
Belanger, L.J.	Killinger, D.K.
Brueck, S.R.J.	Lenth, W.
Burke, J.W.	Menyuk, N.
Bushee, J.F.	Moulton, P.F.
Coulombe, M.J.	Murphy, D.V.
DeFeo, W.E.	Parker, C.D.
Deutsch, T.F.	Peck, D.D.
Ehrlich, D.J.	Sedlacek, J.
Feldman, B.	Sullivan, D.J.
Fetterman, H.R.	Tsao, J.Y.
Hancock, R.C.	Welford, D.

ELECTRONIC MATERIALS

A.J. Strauss, Leader
J.C.C. Fan, Assistant Leader
J.G. Mavroides, Senior Staff
H.J. Zeiger, Senior Staff

Anderson, C.H., Jr.	Kolesar, D.F.
Branz, H.M.*	Krohn, L., Jr.
Button, M.J.	Mastromattei, E.L.
Chapman, R.L.	Metze, G.M.
Chen, C.K.	Nitishin, P.M.
Davis, F.M.	Owens, E.B.
Delaney, E.J.	Palm, B.J.
Fahey, R.E.	Pantano, J.V.
Finn, M.C.	Salerno, J.P.*
Foley, G.H.	Tracy, D.M.
Gale, R.P.	Tsaur, B-Y.
Iseler, G.W.	Turner, G.W.
King, B.D.	Vohl, P.

APPLIED PHYSICS

R.C. Williamson, Leader
F.J. Leonberger, Assistant Leader
T.C. Harman, Senior Staff
R.H. Kingston, Senior Staff
R.H. Rediker, Senior Staff

Armiento, C.A.*	Groves, S.H.	Paladino, A.E.
Becker, R.A.	Hovey, D.L.	Plonko, M.C.
Carter, F.B.	Johnson, L.M.	Schloss, R.P.*
Chinnock, C.B.	Lattes, A.L.*	Spears, D.L.
DeMeo, N.L., Jr.	Liau, Z.L.	Tsang, D.Z.
Diadiuk, V.	Lind, T.A.	Walpole, J.N.
Donnelly, J.P.	McBride, W.F.	Woodhouse, J.D.
Ferrante, G.A.	O'Donnell, F.J.	Yap, D.*
Foyt, A.G.	Orr, L.*	

*Research Assistant

ANALOG DEVICE TECHNOLOGY

E. Stern, Leader
J.H. Cafarella, Assistant Leader
R.W. Ralston, Assistant Leader

Anderson, A.C.	Holtham, J.H.	Ryser, M.A.*
Arsenault, D.R.	Kernan, W.C.	Sage, J.P.
Behrmann, G.J.	Leung, I.	Slattery, R.L.
Brogan, W.T.	Macedo, E.M., Jr.	Withers, R.S.
Dolat, V.S.	Macropoulos, W.	Wright, P.V.
Fischer, J.H.	Melngailis, J.†	Yao, I.
Fitch, G.L.*	Oates, D.E.	
Flynn, G.T.	Reible, S.A.	

MICROELECTRONICS

W.T. Lindley, Leader
F.J. Bachner, Associate Leader
N.P. Economou, Assistant Leader
R.A. Murphy, Assistant Leader

Bozler, C.O.	Flanders, D.C.	Nichols, K.B.
Bromley, E.I.	Gatley, J.S.*	Pang, S.W.
Burke, B.E.	Geis, M.W.	Piacentini, W.J.
Cabral, S.M.	Goodhue, W.D.	Pichler, H.H.
Calawa, A.R.	Gray, R.V.	Rabe, S.
Chiang, A.M.	Hansell, G.L.§	Randall, J.N.
Chu, A.	Lincoln, G.A., Jr.	Rathman, D.D.
Clifton, B.J.	Lyszczarz, T.M.	Reinold, J.H.*
Daniels, P.J.	Mahoney, L.J.	Shaver, D.C.
DeGraff, P.D.	Manfra, M.J.	Silversmith, D.J.
Durant, G.L.	McClelland, R.W.	Smythe, D.L., Jr.
Efremow, N.N., Jr.	McGonagle, W.H.	Vigilante, J.L.
Elta, M.E.	Mountain, R.W.	Vojak, B.A.
Felton, B.J.	Mroczkowski, I.H.	Wilde, R.E.

*Co-op Student

†Part Time

§Research Assistant

1. SOLID STATE DEVICE RESEARCH

1.1 Coherently Coupled Waveguide Bends

Low-loss waveguide bends are essential elements for the efficient interconnection of components in optical guided-wave circuits. We have achieved low bending losses in single-mode Ti:LiNbO_3 channel waveguides by utilizing coherent coupling effects between closely spaced abrupt bends. This technique was originally described theoretically by Taylor.⁽¹⁾ The measured losses are found to be substantially less than the losses through comparable numbers of otherwise identical isolated bends. These bend geometries are particularly useful since they are compatible with conventional photomask pattern generators. Losses as low as 0.08 dB per coupled 1° abrupt bend as compared to 0.8 dB per isolated 1° abrupt bend have been measured. Taylor showed that the loss through a dielectric waveguide structure of closely spaced abrupt bends is a strong oscillatory function of the distance L between each bend because of coupling between the guided and unguided modes. The bending loss was shown to be minimized when

$$L = \frac{(2m + 1)}{2 \Delta n} \lambda \quad (m = 0, 1, 2, \dots)$$

where λ is the free space optical wavelength and Δn is the difference between the effective index of the guided mode and the weighted average effective index of the unguided modes excited at the bends.

A variety of coherently coupled single-mode waveguide structures has been fabricated and tested. The devices were formed by Ti diffusion in X-cut LiNbO_3 with waveguide propagation in the Y direction. The devices were tested by endfire-coupling TE polarized light at $0.633 \mu\text{m}$.

Waveguide structures of the geometry illustrated in Fig. 1-1(a) were investigated to determine the interconnection length L yielding maximum transmission between two abrupt 1° bends. Each device consists of two pairs of closely spaced abrupt bends isolated by a 4-mm-long straight waveguide section. The measured optical transmission through a single bend-pair, taken as the square root of the transmission of the bend structure relative to

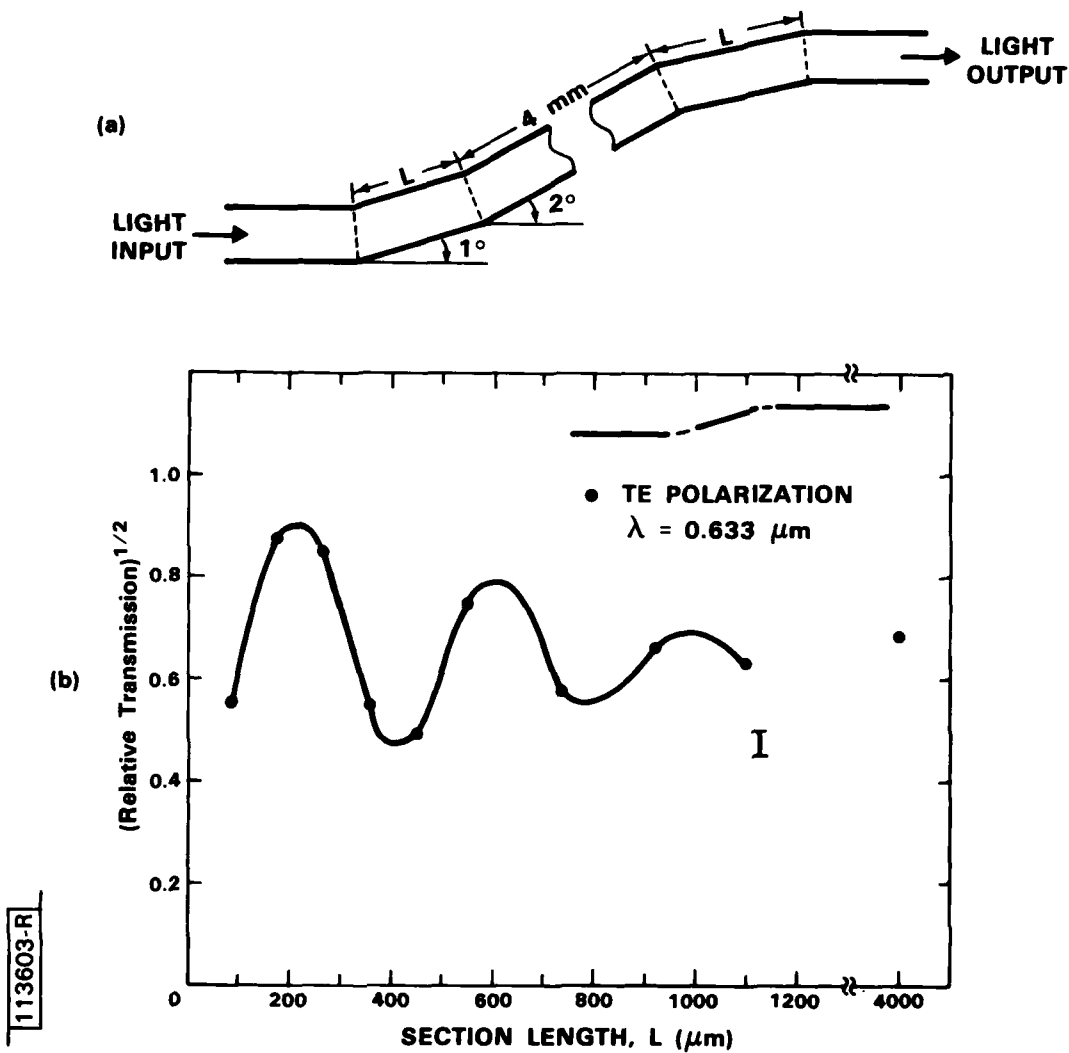


Fig. 1-1. Waveguide structure (a) consisting of two single-section coupled-bend devices and (b) plot of measured transmission of single devices relative to straight guides as a function of interconnection length L .

straight guides interspersed on the same substrate, is plotted in Fig. 1-1(b). A qualitative curve is drawn through the data points. As expected, the optical transmission is oscillatory, with the variation becoming damped with increasing L . The measured bend-pair loss is as low as 0.7 dB at $L = 180 \mu\text{m}$ and as high as 3 dB at $L = 450 \mu\text{m}$. In a separate experiment the loss through an otherwise identical isolated 1° bend was measured to be ~ 0.8 dB.

Multisection bend structures of the geometry shown in Fig. 1-2(a) have also been fabricated and tested. These devices are nearly optimally coupled by setting $L = 180 \mu\text{m}$. Figure 1-2(b) shows the relative optical transmission for $N = 1$ through $N = 5$ sections. The transmission drops very slowly, with N indicating coupling beyond nearest-neighbor bends.

More complicated bend structures consisting of 60, 32, 30, and 32 one-degree bends with $180\text{-}\mu\text{m}$ spacing and with the equivalent of two, two, three, and four curvature reversals, respectively, have also been evaluated to aid in designing devices with many coupled bends (see Fig. 1-3). The 60-bend structure, which has been utilized in an integrated optical temperature sensor,⁽²⁾ has a measured total bend loss of only ~ 6 dB, as compared to an estimated loss based on the results described above of ~ 50 dB through 60 isolated 1° bends. The 32-bend structure with two curvature reversals has a measured bend loss of 3.6 dB. Comparing this result with the 60-bend structure loss indicates a residual loss per coupled 1° bend of ~ 0.08 dB. Combining these results with the measured losses of 4.3 dB and 5.1 dB for the 30- and 32-bend devices with three and four curvature reversals, respectively, indicates a ~ 0.7 dB curvature reversal loss. This is analogous to the well-known mode-conversion losses at curvature discontinuities in smoothly curved guides. In addition, the loss due to a pair of straight-curved transitions is estimated to be ~ 0.3 dB.

Theoretical analysis to date⁽³⁾ on simplified structures shows qualitative agreement with the experimental results. Additional analysis is in progress.

L.M. Johnson
F.J. Leonberger

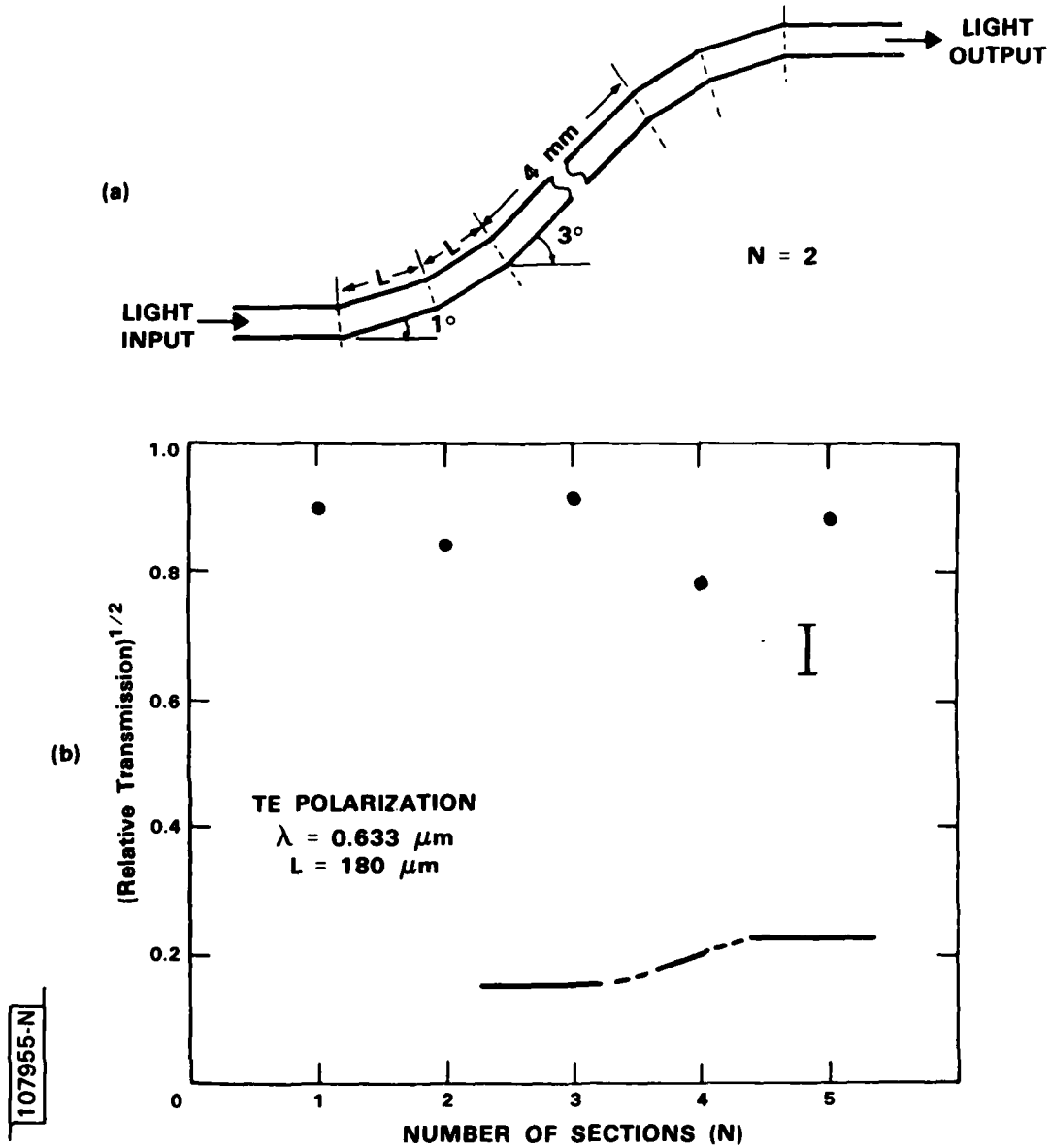


Fig. 1-2. Typical waveguide structure (a) consisting of two multi-section coupled-bend devices and (b) plot of measured transmission relative to straight guides of single devices with $N = 1$ to $N = 5$ sections with $L = 180 \mu\text{m}$.

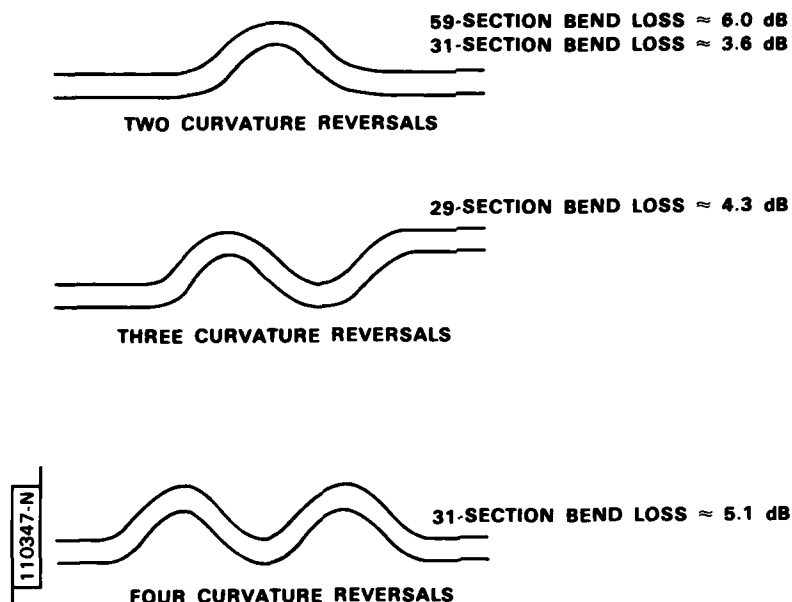


Fig. 1-3. Waveguide structures consisting of 60, 32, 30, and 32 one-degree bends with 2, 2, 3, and 4 curvature reversals, respectively, with interconnection length of 180 μ m.

1.2 Effect of Threading Dislocations on the Dark Current of InP APDs

Dislocation etch studies were carried out on high performance InP APDs fabricated with epitaxially grown junctions on moderate-dislocation-density substrate ($\sim 5000/\text{cm}^2$). Threading dislocations were found not to influence the dark current, in marked contrast to previously reported results on devices with junctions formed by diffusion.

The devices investigated in this study were InP n-p⁺ inverted-mesa structures fabricated using liquid phase epitaxial (LPE) growth and standard photolithographic techniques. The structure and device parameters are shown in the inset of Fig. 1-4. The (100), p⁺ substrate (grown by the liquid-encapsulated Czochralski method and doped with Zn to the $1-2 \times 10^{18} \text{ cm}^{-3}$ level) is used without a buffer layer. However, an equilibrium atmosphere of phosphorus from PH₃ is maintained in the growth tube to prevent thermal etching before and after growth, and an in-situ etch under In, removing

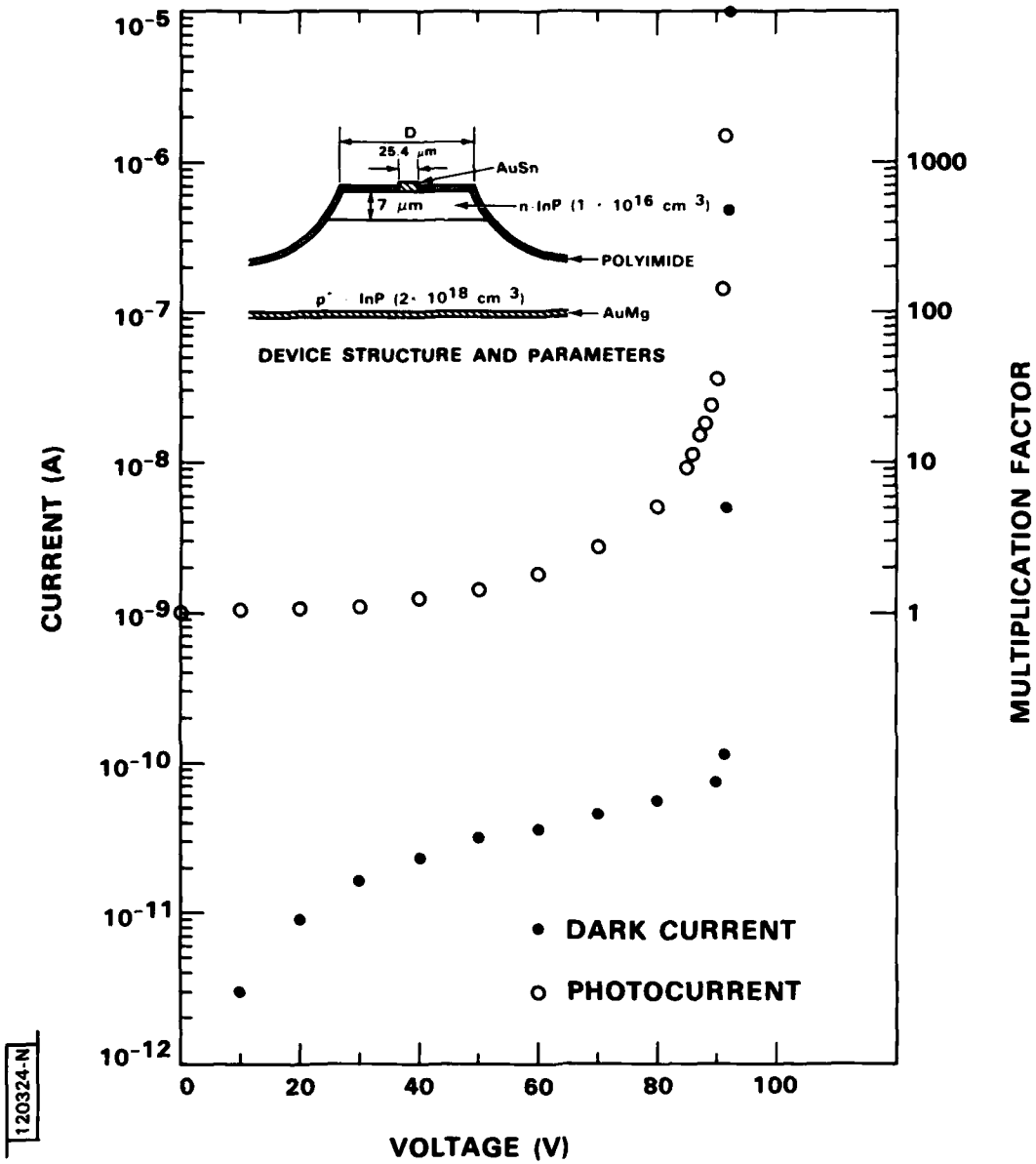


Fig. 1-4. I-V characteristics in the dark and with 1 nA of incident photocurrent; multiplication factor is also shown.

5-10 μm , precedes the growth. This simple technique yields devices that are as good or better than those with an epitaxially grown, p^+ buffer layer. The n layer is not intentionally doped and has $\sim 1 \times 10^{16}$ net donors/ cm^3 . The thin n^+ cap layer (Sn doped to $\sim 1 \times 10^{18} \text{ cm}^{-3}$), usually grown to avoid surface band-bending effects and for ease of contacting, was omitted for clarity in revealing the dislocations; the alloyed AuSn contacts were, nevertheless, verified to be ohmic. The absence of the n^+ layer, though affecting the quantum efficiency,⁽⁴⁾ did not have any effect on the dark current characteristics. Prior to device fabrication, the wafers were etched with the H etch⁽⁵⁾ to reveal dislocations. Mesas of six different diameters were then fabricated, and the etch pits, still visible on the mesas, could then be counted for each device. The devices were passivated with polyimide⁽⁶⁾ and exhibited very low dark current densities on the order of $2 \times 10^{-6} \text{ A/cm}^2$ at $0.9 V_b$ (V_b = breakdown voltage).

Typical reverse I-V characteristics, with and without light, are shown in Fig. 1-4, together with the multiplication factor (M), or gain, obtained with a primary photocurrent (I_{po}) of $\sim 1 \text{ nA}$. The photocurrent was measured by illuminating the device from the front with $0.6328\text{-}\mu\text{m}$ light from a He-Ne laser. The maximum M exhibited an inverse square-root dependence on I_{po} , in agreement with the gain saturation model of Melchior and Lynch.⁽⁷⁾ Edge breakdown was eliminated by the use of the inverted-mesa configuration, and the photoresponse was uniform over the entire area up to the maximum gain, as established by raster scanning the devices. There was no evidence of microplasmas appearing either as kinks in the I-V curves or spikes in the scans.

Figure 1-5 shows the number of dislocation etch pits on $100\text{-}\mu\text{m}$ -diameter devices plotted against the voltage at which the device exhibited 50 nA of dark current. For the best devices, this voltage was 90-92 V [where $V_b = V(5 \text{ }\mu\text{A}) = 92 \text{ V}$]. Within this category were devices with as many as 20 dislocation etch pits. Similar plots were obtained for devices with larger and smaller diameters, including some with zero etch pits. We conclude that the presence of dislocations does not increase the dark current.

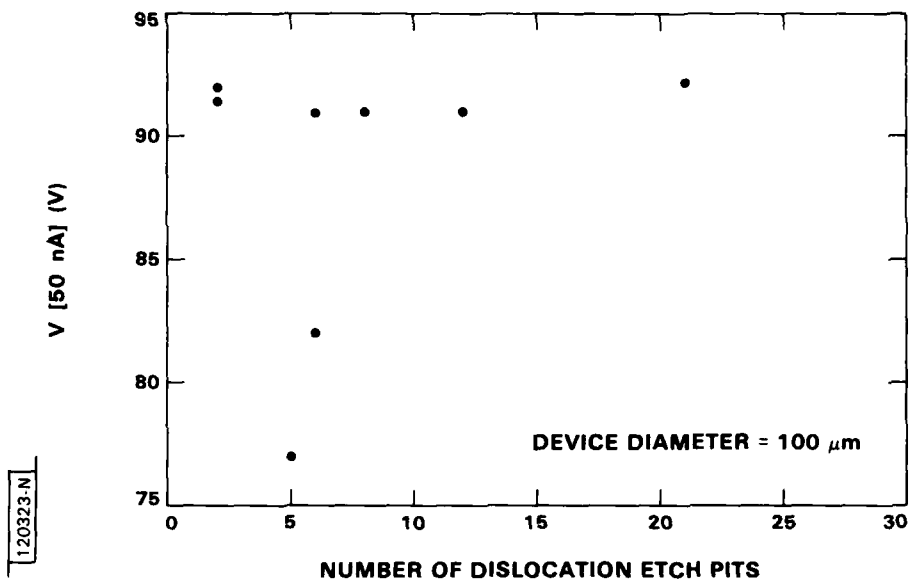


Fig. 1-5. Voltage at which devices draw 50 nA of dark current vs number of dislocation etch pits.

This result is in contrast to that of a previous report for diffused-junction structures⁽⁸⁾ in which the dark current versus voltage curves exhibited discontinuities when dislocations were present (a break point was observed for every dislocation). Furthermore, the breakdown occurred at lower voltages than expected for devices with dislocation etch pits. No such behavior was observed in this study; no discontinuities in the I-V curves were observed, and the breakdown voltage was the same for devices of all sizes and ranging in etch pit count from 0 to 32. (Diffusion is very small for the LPE-grown junction, given that the metallurgical and electrical junctions coincide to within $\sim 0.1 \mu\text{m}$.)

From this clear difference between our devices and those of Lee and Burrus,⁽⁸⁾ it is possible to hypothesize that when the junction is formed by diffusion, the dislocations act as channels for enhanced diffusion. This would lead to nonplanar p-n junctions with localized high-field regions that

could give rise to microplasmas, high dark current, and premature reverse bias breakdown.

V. Diadiuk
S.H. Groves

1.3 Spatial Light Modulation Using Electroabsorption in a GaAs Charge-Coupled Device

High speed one- and two-dimensional spatial light modulation may be carried out using the electroabsorption (Franz-Keldysh) effect in a GaAs buried channel charge-coupled device (CCD). For photon energies slightly lower than the energy gap, the transmission through or along the surface of a CCD structure may be controlled by the signal charge in the wells, through the change of electric field with charge. The modulator is thus electrically addressable and promises optical quality sufficient for coherent applications. Experimental measurements on a specially designed GaAs CCD structure with semitransparent gates have verified the predicted performance.⁽⁹⁾

R.H. Kingston
B.E. Burke
K.B. Nichols
F.J. Leonberger

References

1. H.F. Taylor, Appl. Opt. 13, 642 (1974).
2. L.M. Johnson, F.J. Leonberger, and G.W. Pratt, Jr., Appl. Phys. Lett. 41, 134 (1982).
3. L.M. Johnson, Ph.D. thesis, M.I.T., Cambridge, MA 1981 (unpublished).
4. V. Diadiuk, C.A. Armiento, S.H. Groves and C.E. Hurwitz, Solid State Research Report, Lincoln Laboratory, M.I.T. (1981:4), p. 7.
5. A. Huber and N.T. Linh, J. Crystal Growth 29, 80 (1975).

6. V. Diadiuk, C.A. Armiento, S.H. Groves and C.E. Hurwitz, Electron Devices Lett. EDL-1, 177 (1980).
7. H. Melchior and W.T. Lynch, IEEE Trans. Electron Devices ED-13, 829 (1966).
8. T.P. Lee and C.A. Burrus, Appl. Phys. Lett. 36, 587 (1980).
9. R.H. Kingston, B.E. Burke, K.B. Nichols and F.J. Leonberger, Appl. Phys. Lett. 41, 413 (1982).

2. QUANTUM ELECTRONICS

2.1 Simultaneous Heterodyne And Direct Detection CO₂ Lidar Measurements

A dual-CO₂ laser differential-absorption LIDAR (DIAL) system has been developed that incorporates both direct detection and heterodyne detection of the same LIDAR returns. This system has been used to compare experimentally the signal-to-noise ratios and statistical/temporal characteristics of the DIAL returns in order to quantify the differences between the two detection methods.

Figure 2-1 is a schematic of the dual-laser DIAL system. Two tunable, nonstabilized hybrid-TEA CO₂ lasers provide the pulsed single-frequency 10 μ m radiation. The TEA laser operates at a PRF of 100 Hz, with an output energy of 10 mJ per pulse and a pulse length of approximately 200 ns. The low pressure gain cell is operated slightly above threshold at a cw output laser power of about 100 mW.

The frequency of the hybrid-TEA laser is adjusted to an offset frequency of approximately 20 MHz relative to that of the stabilized CO₂ laser local oscillator (LO). A room temperature HgCdTe detector and a 1 μ s gated frequency counter were used to monitor the heterodyne beat frequency between the cw portion of the hybrid-TEA laser radiation and the local oscillator; this value was found to be within 1-2 MHz of that obtained with a precision frequency counter and transient digitizer which measured the frequency of the pulsed portion of the heterodyne LIDAR return. The measurements established that the pulse-to-pulse frequency stability of the hybrid-TEA laser was approximately 10 MHz and the intrapulse stability (chirp) was approximately 1 MHz. The TEA discharge disrupted the lasing of the cw gain cell, which limited the PRF of the system to approximately 100 Hz, dependent upon discharge and gas-mixture conditions.

The outputs from the two lasers were combined with a 50/50 beamsplitter, expanded by a x10 beam expander, and directed out the laboratory window. The backscattered LIDAR radiation from selected targets was collected using a Cassegrain telescope and split with a 50/50 beamsplitter. Half of the



Fig. 2-1. Dual-laser DIAL system.

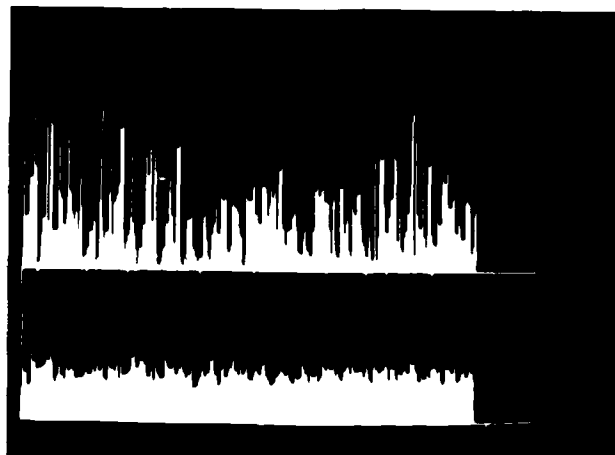
returned beam was directed toward a cooled direct-detection HgCdTe detector, and the other half was mixed with the CO₂ local oscillator output and directed toward a cooled heterodyne-detection HgCdTe detector. The output signals from the detectors were sent to a high-speed data acquisition system. This system monitored the frequency offset of each laser pulse to ensure that it fell within the 50 MHz bandpass of the detector amplifiers, normalized the LIDAR returns to the laser pulse energy, and calculated the statistical and temporal characteristics of the returns. Heterodyne returns have been obtained from topographic targets at ranges up to 10 km and from atmospheric aerosols at ranges of approximately 0.5 km.

The carrier-to-noise ratio, C/N, which represents the average intensity of the LIDAR returns, was measured for several targets at different ranges. With a flame sprayed aluminum plate serving as a diffusely reflecting target at a range of 2.7 km, the direct-detection (C/N) ratio was about 10 and the heterodyne-detection (C/N) ratio was approximately 10,000. The difference in these two values is in reasonable agreement with theory; the NEP for the noncoherent detector is 4×10^{-9} W and the estimated noise for the heterodyne detector is approximately 2×10^{-12} W.

The difference in the statistical characteristics of the LIDAR returns for the two detection techniques is shown in Fig. 2-2. As expected, the speckle-induced fluctuations for heterodyne-detection are increased compared to those for aperture-averaged direct-detection returns. Measured standard deviations of the LIDAR return fluctuations from targets at a range of 2.7 km were 20% and 100% for diffuse target returns, and 70% and 120% for retroreflector returns, respectively, for direct detection and heterodyne detection. These values are consistent with theoretical predictions⁽¹⁾ and indicate the differences in the intrinsic accuracy of heterodyne-detection DIAL systems compared to direct-detection.

Figure 2-3 shows results of the measurement of the temporal pulse-pair correlation coefficient, ρ , of the dual-laser heterodyne returns from a diffuse target as a function of the pulse separation time between the two laser pulses. These results are similar to those obtained for direct

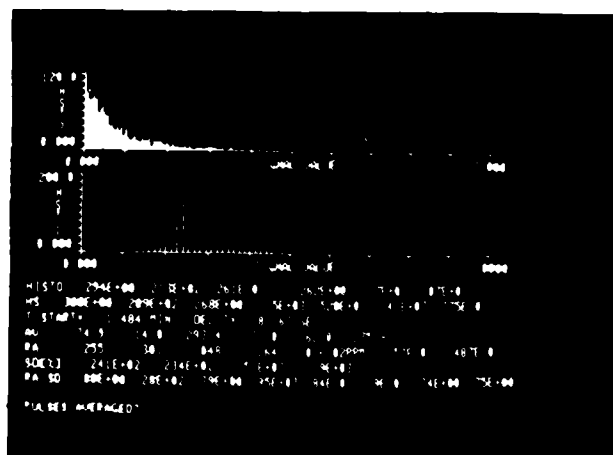
TEMPORAL HISTORY OF LIDAR RETURNS



HETERODYNE

DIRECT

HISTOGRAM AND STATISTICAL DATA OF LIDAR RETURNS



HETERODYNE

DIRECT

Fig. 2-2. Computer display showing temporal and statistical data of LIDAR returns from a diffuse target at a range of 2.7 km.

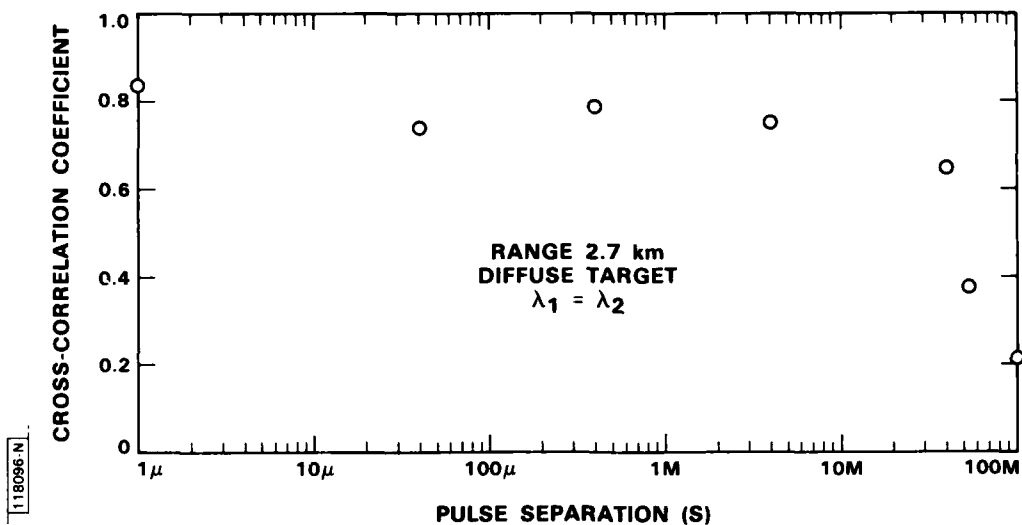


Fig. 2-3. Temporal correlation of two heterodyne LIDAR returns as a function of LIDAR pulse separation time.

detection.⁽²⁾ However, when the wavelengths of the two heterodyne lasers pulses were not equal (i.e., different by 4 cm^{-1}), a very significant decrease in the value of ρ at short delay times was observed; such a decrease was not observed for returns from retroreflectors. These results are in qualitative agreement with theoretical predictions⁽³⁾ and indicate the degree to which a dual-laser DIAL system is able to compensate for the atmospheric turbulence induced perturbations on the LIDAR returns.

D.K. Killinger
N. Menyuk
W.E. DeFeo

2.2 $\text{Ti:Al}_2\text{O}_3$ - A New Solid State Tunable Laser

Excited-state absorption (ESA) affects the operation of a number of transition-metal-doped tunable solid state lasers. ESA reduces laser gain

and efficiency when the laser wavelength is capable of inducing transitions between the upper laser energy level and higher lying levels. Laser efficiency is also reduced by ESA when the pump radiation can induce such transitions. For lamp-pumped lasers, the higher lying levels that cause the ESA are nevertheless useful in creating absorption bands which permit coupling to the full spectrum of pump radiation. In resonantly pumped laser schemes in which pump radiation is supplied by another laser and is resonant with the ground state to first-excited-state absorption band, the higher lying levels are not necessary and can only serve to produce ESA. All of the transition-metal ions which have been used in lasers (V^{2+} , Cr^{3+} , Co^{2+} , and Ni^{2+}) have numerous d-electron energy levels above the first excited state. In at least three systems using these ions, $Ni:MgF_2$,⁽⁴⁾ $V:MgF_2$,⁽⁴⁾ and $Cr:BeAl_2O_4$,⁽⁵⁾ ESA apparently has an effect on performance.

One ion, Ti^{3+} , which has previously not been used in lasers, has essentially only two d-electron energy levels in a crystalline environment. The degenerate energy levels of the Ti^{3+} single d-electron in free space are split by an octahedral crystal field into a 2T_2 triply degenerate lower level and a doubly degenerate 2E upper level. In crystals with site symmetries lower than octahedral, the two basic levels are split further, but generally the splitting is small compared to the 2T_2 - 2E splitting. Because the latter splitting is due entirely to the crystal field, coupling between the energy levels and the lattice is strong; absorption and fluorescence occur primarily in broad bands separated by a Stokes shift. Because of the strong coupling, four-level laser operation using the two d-electron levels is possible, but ESA to higher d-electron levels is eliminated. The possibility of ESA to higher non-d-electron states, such as p-states or charge-transfer states still exists, but usually such levels are too high in energy to have any effect.

The measured d-electron, π -polarized absorption, and fluorescence bands⁽⁶⁾ from $Ti:Al_2O_3$ at 300 K are shown in Fig. 2-4. Structure in the absorption band is due to Jahn-Teller splitting of the 2E upper level. The

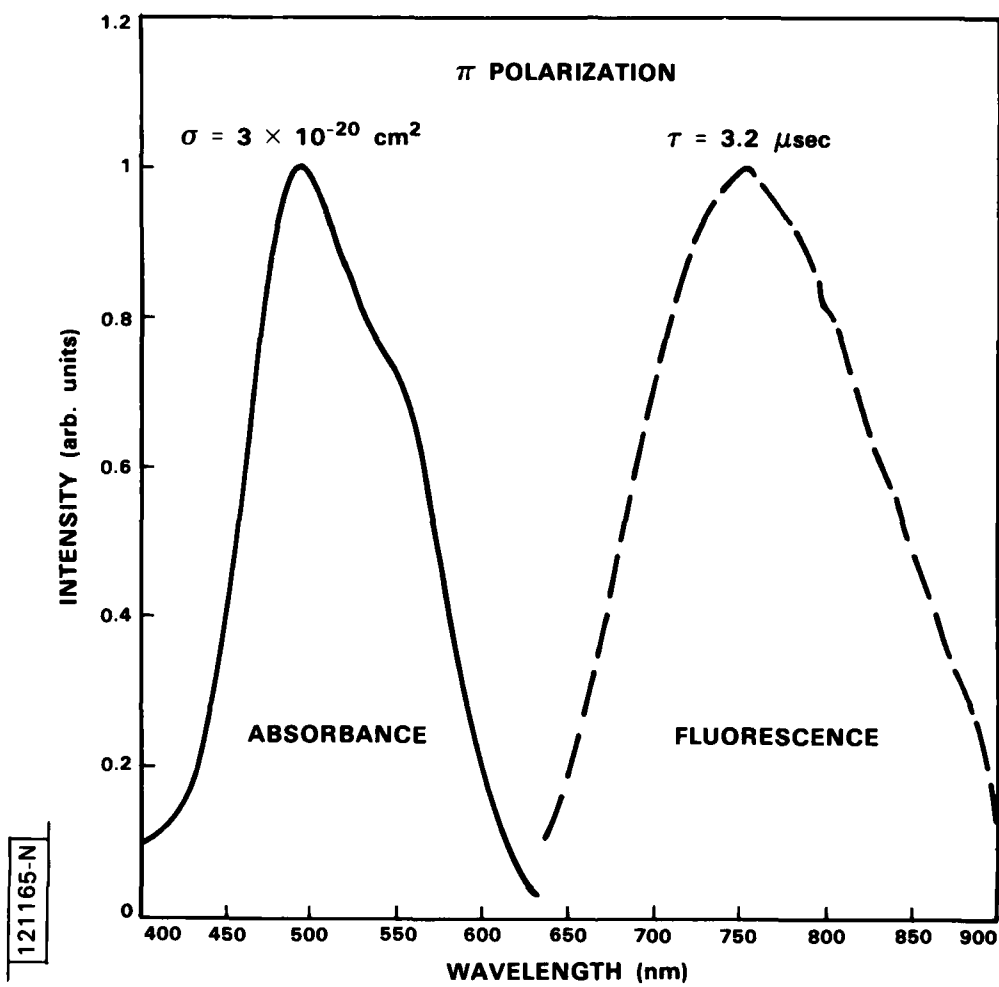
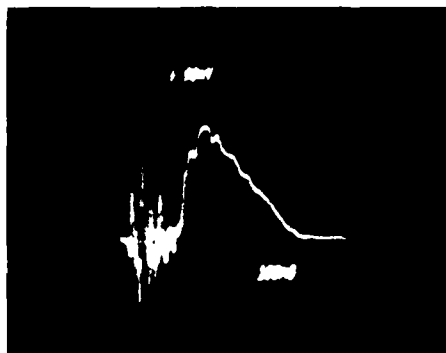


Fig. 2-4. π -polarized absorbance and fluorescence from $\text{Ti:Al}_2\text{O}_3$ at 300 K.

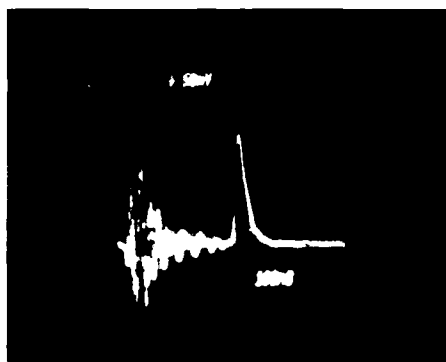
doping level of the sample studied was measured by X-ray fluorescence techniques to be approximately 0.1 wt% Ti_2O_3 ; from this the peak absorption cross section was determined to be at least $3.2 \times 10^{-20} \text{ cm}^{-2}$. (Since some of the impurity ions could be in the Ti^{4+} state, it is possible that this cross section could be higher.) If the dipole moments for absorption and emission were assumed equal (unlikely because of the large Stokes shift), a stimulated emission cross section three times greater would be obtained because of level degeneracies. The fluorescence lifetime was found to be 3.2 μs at 300 K, increasing to 3.8 μs at 77 K.

An optical gain measurement in $\text{Ti:Al}_2\text{O}_3$ was made by optically pumping a crystal with an argon-ion laser at 514.5 nm and probing the pumped region with the 672.8-nm line from a krypton-ion laser. The peak cross section at 750 nm was determined to be approximately $2 \times 10^{-19} \text{ cm}^2$. If such a value is used in the Einstein relation between lifetime and stimulated emission cross section, the predicted lifetime is about 3.6 μs , in good agreement with the measured value. Thus the radiative quantum efficiency of $\text{Ti:Al}_2\text{O}_3$ appears to be quite high.

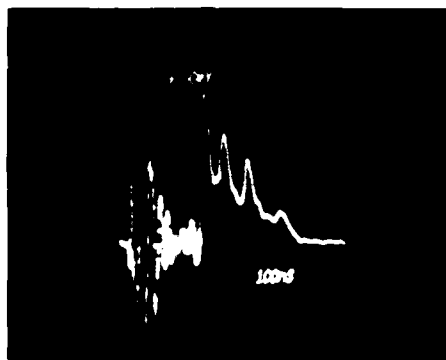
Laser operation was obtained from a 9-mm-long $\text{Ti:Al}_2\text{O}_3$ crystal at room temperature, pumped longitudinally by a coaxial-flashlamp-pumped dye laser operating at 503 nm. The uncoated crystal was of poor optical quality, exhibiting considerable scattering and optical distortion; however, the high gain of the ${}^2\text{E} \rightarrow {}^2\text{T}_2$ transition overcame the crystal losses. Figure 2-5(a) shows the pulse shapes of the pump laser and Figures 2-5(b) and 2-5(c) those of the $\text{Ti:Al}_2\text{O}_3$ laser at two pump levels above threshold at the operating wavelength of 756 nm. The optical cavity used consisted of an 8% transmission flat mirror and a 15% transmission concave mirror (with a radius of 75 cm) spaced by 26 cm. Threshold fluence was estimated to be 2 J/cm^2 , and the crystal absorbed ~80% of the pump radiation. The pulsed or "spiking" behavior of the $\text{Ti:Al}_2\text{O}_3$ laser is consistent with the long upper-laser-level lifetime compared to the cavity lifetime. Further experiments with a different flat mirror (~18% transmission) yielded a single-ended output energy of nearly 1 mJ at a pump input energy of 36 mJ.



(a) DYE LASER PUMP PULSE
 $\lambda = 504 \text{ nm}$



(b) $\text{Ti:Al}_2\text{O}_3$ LASER OUTPUT
 $\lambda = 750 \text{ nm}$
 $1.6 \times \text{THRESHOLD}$



(c) $3.6 \times \text{THRESHOLD}$

118216-R-01

Fig. 2-5. Output pulse shapes.

As a preliminary attempt at tuning the $\text{Ti:Al}_2\text{O}_3$ laser, the flat mirror was replaced by a Littrow-mounting diffraction grating, and output was observed from the zeroth order. Although the surface of the grating was damaged by the first $\text{Ti:Al}_2\text{O}_3$ laser pulse, laser operation was still observed on subsequent pulses and the output could be tuned over the range 718-770 nm.

It is expected that with higher quality crystals, improvements in all aspects of the $\text{Ti:Al}_2\text{O}_3$ laser will be observed. Given the superior thermal and mechanical properties of the host crystal, it is likely that this laser will be capable of high-average-power operation and, with the lack of any ESA for the laser radiation, tuning over the full fluorescence region (with half power points at 680 and 850 nm) should be possible. The broad absorption band centered at 500 nm overlaps the output lines of the argon-ion, Cu-vapor, and doubled Nd-laser systems to allow pumping by any of those sources. Flash-lamp pumping may also be possible, but for full energy storage in Q-switched operation, lamp pulse widths will have to be 3 μs or less. The gain cross section of the $\text{Ti:Al}_2\text{O}_3$ laser transition is sufficiently high to allow short pulse Q-switched operation without excessive cavity fluences, unlike other tunable transition-metal lasers.

Operation of Ti^{3+} -ion lasers in different host crystals is possible. Crystals with Al^{3+} or Ga^{3+} ions are potential hosts; these include YAG, $\text{Gd}_3\text{Ga}_5\text{O}_{12}$, or other garnets; BeAl_2O_4 , and spinels such as MgAl_2O_4 . While all of these materials are not as ideal as Al_2O_3 with respect to thermo-mechanical properties, the sensitivity of the ${}^2\text{E}-{}^2\text{T}_2$ splitting to crystal field would result in a wide variation in operating wavelengths with host crystal. Also, longer upper-state lifetimes (and subsequent small gain cross sections) are likely to be observed in crystals with higher site symmetries than Al_2O_3 , which might allow flash-lamp-pumped operation with more conventional ($\sim 100 \mu\text{s}$) pulse widths.

Finally, operation analogous to that with Ti^{3+} might be achieved with the Cu^{2+} ion. That ion has nine d-electrons, or one less than a filled d-shell, and because of the complementarity principle,⁽⁷⁾ the ion has a similar level structure to the Ti^{3+} ion, except that the ${}^2\text{E}$ level is lowest in

(The Cu^{2+} ion can be viewed as having a single hole state.) Likely host crystals for the Cu^{2+} ion are the rutile- and perovskite-structure fluoride materials such as MgF_2 , ZnF_2 , and KMgF_3 , and oxides containing the Mg^{2+} ion.

P.F. Moulton

2.3 Laser Microchemical Deposition of Conducting Links for Restructurable VLSI

In conjunction with Laboratory efforts in laser restructurable VLSI (RVLSI) and electron beam testing, a series of experiments has been initiated to adapt recently developed laser direct-wiring techniques to discretionary deposition of conducting links on silicon-integrated circuits. The initial objectives have been to evaluate several possible approaches based on the new techniques. In particular, a new laser chemical deposition technique is being explored for this application; doped poly-Si conducting films have been deposited with high spatial resolution and their electrical and physical properties have been characterized. We have also tested a previously developed laser photochemical metal deposition process using a variety of link structures. A preliminary report comparing the two new methods is given here. We have found that both methods show promise for discretionary routing on simple single-level-metal structures without a requirement for prefabrication of a special thin-film link structure. However, our limited initial experiments on advanced circuit restructuring apparatus show that process and exposure conditions must be carefully controlled; a good gap structure has yet to be developed, and exposure levels and pointing accuracies have not yet been refined to an extent allowing dependable link formation.

In poly-Si LCVD, a laser is used to locally heat a substrate in the presence both of a semiconductor-bearing gas (e.g., SiH_4) and of a dopant-bearing gas [e.g., $\text{B}(\text{CH}_3)_3$]. The heat drives a local chemical reaction, which results in the deposition of heavily doped semiconductor links. The relevant mechanism and kinetics of poly-Si deposition have been described.⁽⁸⁾

To adapt the poly-Si deposition process to RVLSI, heavy p-type doping is desirable for low-resistance contacts to Al metallization. In a first series of experiments, such heavily doped Si was deposited from silane mixed with volatile boron-encapsulating compounds and its properties characterized.

A focused, 15 W (multiline), Ar-ion laser was used to irradiate silicon substrates. Focusing was with an achromatic doublet used at $\sim f/10$, or with a three-element lens used at $\sim f/2.7$. The substrates were enclosed within a 1-cm-long gas cell containing 100-200 Torr of electronic-grade SiH_4 and were translated perpendicular to the optical axis at rates of 90-440 $\mu\text{m/s}$. Several millimeter-square samples for diagnostics were prepared by raster scanning. Typical focal spot diameters were 2.5 to 10 μm , resulting in intensities of $\sim 0.5\text{--}20 \text{ MW/cm}^2$ at the focus. The substrates were (111) and (100) Si with surfaces covered by 10-20 Å of native oxide, or with 3000-5000 Å of thermally grown SiO_2 . In some cases, runs were made on Si substrates stripped of native oxide using buffered HF. Samples were degreased in organic solvents, placed into the gas cell, and then passivated by exposure to several hundred Torr of SiH_4 . Following the reaction, samples were characterized by measuring thicknesses with a mechanical stylus and by scanning electron microscopy (SEM), and the crystal morphology was determined by Raman spectroscopy and X-ray diffraction.

Low resistivity films were deposited by adding various doping gases to the SiH_4 gas fill. It was found necessary to use an additive with a pyrolysis rate reasonably close to that of SiH_4 . For example, $\text{Al}(\text{CH}_3)_3$ was found to be depleted selectively from the cell. Excellent results, however, were obtained with BCl_3 and $\text{B}(\text{CH}_3)_3$.

Resistivity measurements were made on 1.5-mm-long, 1-2 μm -thick, 30- μm wide Si strips written on 1000-2000 $\Omega\text{-cm}$ Si substrates using three partially overlapped 90- $\mu\text{m/s}$ scans. The resistance of the films was then measured using two probes separated by varying distances. Measurements were made both before and after a 15-minute 900°C furnace anneal in dry H_2 . No open-circuited strips due to fissures in the deposited films were found.

Figure 2-6 shows resistivity as a function of the pressure of the boron dopant gas in 200 Torr of SiH_4 . Note that the resistivity values for pure SiH_4 are only lower limits because of the finite substrate resistivity. With $\text{B}(\text{CH}_3)_3$ the best films have resistivities $\sim 1.5 \times 10^{-3} \Omega\text{-cm}$, within the range of currently used Si interconnects. The variation in resistivity with additive pressure is relatively weak, and the additive does not change the deposition rate or film morphology. A modest increase in resistivity occurs after the H_2 anneal. Doping with BCl_3 produces films of 10X higher resistivity, although the resistivity decreases with the anneal. We conclude that sharply defined, low-resistivity, 1-2 μm conductors can be made using the Ar-ion laser.

In a second series of experiments, it has been demonstrated that an alloyed ohmic contact can be made directly to Al films by careful control of the Ar-ion laser intensity, although the conditions for good contact depend on underlying SiO_2 and Al metallization thicknesses, on the metallization geometry, and on the beam spot-size and confocal parameter of the laser focusing optics.

The test structures we have used in applying LCVD to forming conducting links are shown in Fig. 2-7. Preliminary results using a mechanically shuttered, 1-100 ms pulse-length Ar-ion laser focused to a several micrometer spot are shown in Table 2-1. There is a narrow window in laser power within which good, conducting (100 Ω) links are formed without oxide damage. This window shifts to lower powers if the laser pulse is lengthened or if multiple pulses are used. However, there is also a lower bound to the laser power which will provide good links; below this power the (unsintered) contact resistances between the doped semiconductor and the Al pads become very large.

The second process we have investigated is UV laser photodeposition,⁽⁹⁾ in which a metal bearing compound is dissociated by a focused laser beam to write conducting metal links. This technique has the additional advantage of being an extremely low temperature technique, and therefore nondisruptive to closely placed active device elements. With this approach we have formed Zn and Cd links with resistances of 3-10 $\Omega \mu\text{m gaps}$.

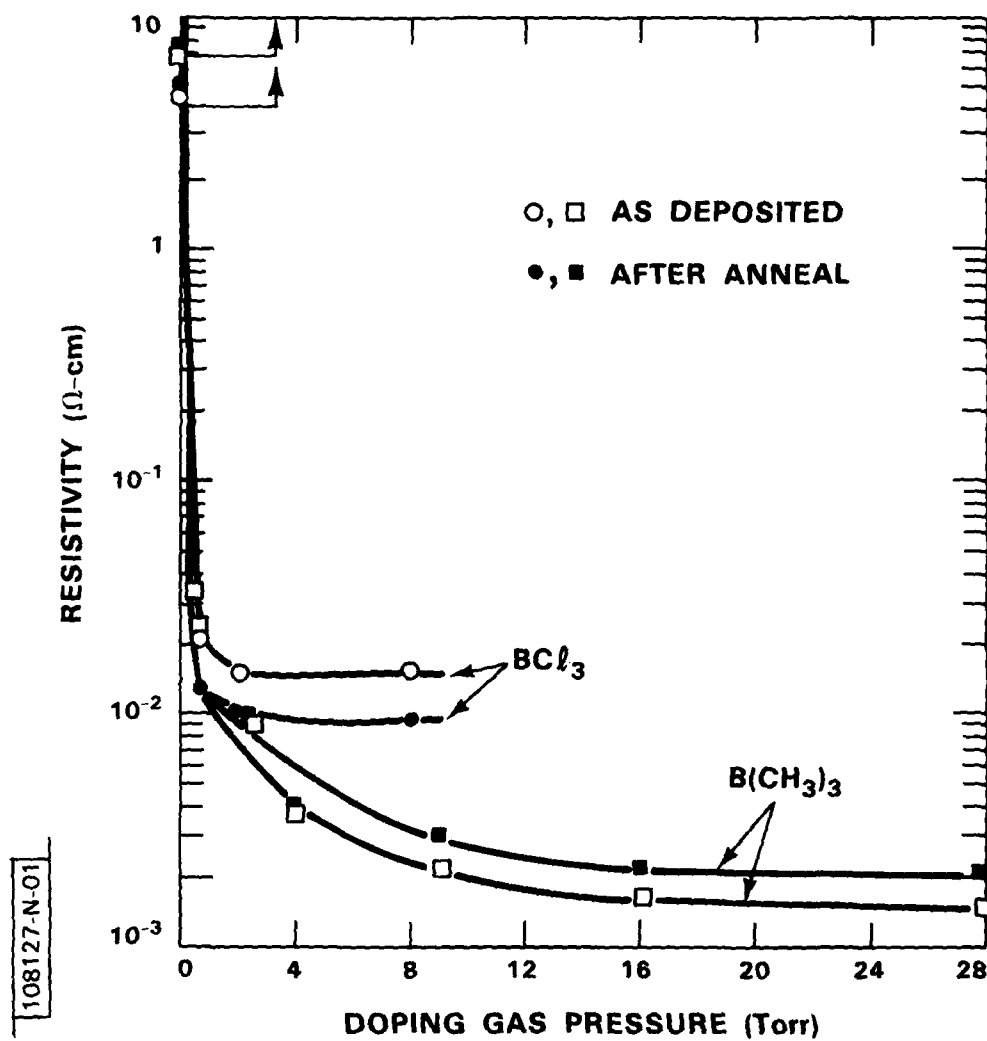


Fig. 2-6. Resistivity vs. boron-dopant gas pressure for films deposited using 200 Torr SiH_4 (f/10 focusing, 2 W). Values for undoped SiH_4 are lower limits.

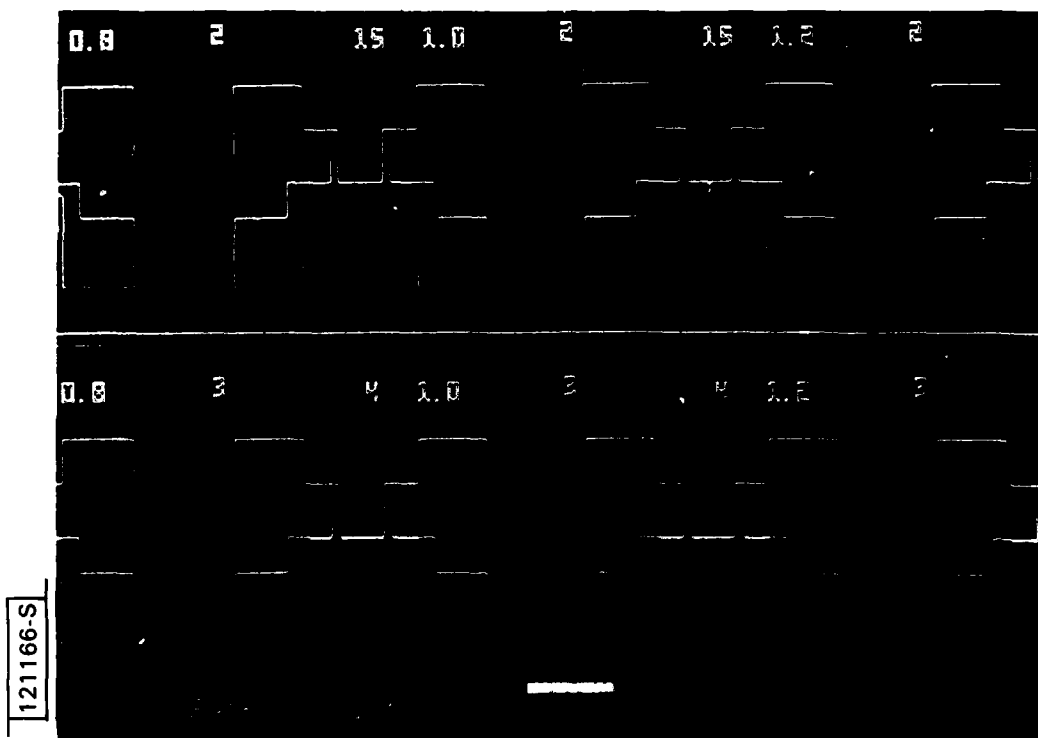


Fig. 2-7. Test structures for deposition and evaluation of RVLSI links.

TABLE 2-1		
COMPARISON OF TWO LASER MICROCHEMICAL LINKING TECHNIQUES		
	Laser CVD	Laser Photodeposition
<u>Process Characteristics</u>		
Link Material	Doped Poly-Si ($10^{-3} \Omega\text{-cm}$)	Cd, Zn ($10^{-4} \Omega\text{-cm}$)
Peak Local Temperature	600°-1500°C	20°-50°C
Spatial Resolution	2-20 μm	0.7-50 μm
<u>Linking Results</u>		
Resistance (typical)	10-200 Ω^*	3-10 Ω^{**}
Ohmic Contact	Al	Au, Al
Laser Exposure	50 ms/link	10 s/link
<u>Comments</u>	Sensitive to laser power and geometry; insensitive to surface preparation and gas handling	Sensitive to surface preparation; insensitive to laser power and link geometry
*2-3 μm gaps **10 μm gaps		

A comparison of the two processes is given in Table 2-1. We have found that both laser deposition techniques are capable of producing useful RVLSI links. Both approaches are potentially reversible and offer very high spatial resolution with low processing temperatures. The LCVD process has a greater speed and a lower sensitivity to surface conditions and is probably preferable to the UV process when a moderate (600°-1200°C) peak local temperature rise is allowable. Experiments are presently in progress to develop a gap structure, determine parameter sensitivities, and establish equipment and process requirements for reliable LCVD of doped poly-Si links.

D.J. Ehrlich	G.H. Chapman*
J.Y. Tsao	D.J. Silversmith
B.P. Mathur*	

2.4 Single Mode Waveguide Multiplication and Mixing at Submillimeter Frequencies

To generate tunable radiation at power levels suitable for use as a heterodyne local oscillator, a submillimeter crossed-guide doubler has been developed. Based upon designs scaled from lower frequencies,¹⁰ this doubler has fundamental waveguide both at 1 mm and 0.5 mm, separated by a coaxial choke to isolate the harmonics. The device was tested in three modes of operation. First, when pumped by 10 mW of 285 GHz carcinotron radiation, it radiated over 700 μW at the second harmonic. As a harmonic mixer at 570 GHz, it yielded a noise temperature of 23,000 K DSB with only 2 mW of input pump power at 285 GHz. Finally, tested as a fundamental-guide radiometric mixer at 600 GHz with a laser LO, it had a noise temperature of 2,800 K, better than the lowest results obtained with quasi-optical corner reflectors. This is the first fundamental-guide mixer that gives state-of-the-art performance at 600 GHz. The device, when pumped by solid state sources, is likely to provide broadly tunable LOs and high sensitivity detectors at submillimeter wavelengths.

H.R. Fetterman
N.R. Erickson†

*Group 23.

†Five College Radio Astronomy Observatory, U. Massachusetts, Amherst, MA.

References

1. J.H. Shapiro, B.A. Capron and R.C. Harney, *Appl. Optics* 20, 3292 (1981).
2. D.K. Killinger and N. Menyuk, *IEEE J. Quantum Electron.* QE-17, 1917 (1981).
3. G. Parry, in *Laser Speckle and Related Phenomena*, edited by J.C. Dainty (Springer-Verlag, New York, 1975), p. 100.
4. Solid State Research Report, Lincoln Laboratory, M.I.T. (1981:3), pp. 15-21.
5. J.C. Walling et al., *IEEE J. Quantum Electron.* QE-16, 1302 (1980).
6. Previous absorption measurements are reported in the following articles: D.S. McClure, *J. Chem. Phys.* 36, 2757 (1962); G.A. Keig, *J. Crystal Growth* 2, 356 (1968). An earlier measurement of fluorescence, which places the peak emission wavelength at 700 nm, is reported by B.F. Gachter and J.A. Koningstein, *J. Chem. Phys.* 60, 2003 (1974).
7. S. Sugano, Y. Tanabe and H. Kamimura, *Multiplets of Transition-Metal Ions in Crystals* (Academic Press, New York, 1970), p. 86.
8. D.J. Ehrlich, R.M. Osgood, Jr. and T.F. Deutsch, *Appl. Phys. Lett.* 39, 957 (1981).
9. D.J. Ehrlich, R.M. Osgood, Jr. and T.F. Deutsch, *J. Vac. Sci. Technol.* 21, 23 (1982).
10. N.R. Erickson, *Digest IEEE International Microwave Symposium*, Washington, D.C. (1980).

3. MATERIALS RESEARCH

3.1 Lateral Epitaxial Overgrowth of GaAs by Organometallic Chemical Vapor Deposition

Several new device structures have recently been prepared at Lincoln Laboratory by using chemical vapor deposition to grow epitaxial GaAs layers laterally over oxide⁽¹⁻³⁾ or metal⁽⁴⁾ films on GaAs substrates. The lateral growth was seeded by epitaxial deposits initially formed on exposed regions of the substrate. Growth was carried out by the $\text{AsCl}_3\text{-GaAs-H}_2$ technique, which uses HCl in the deposition process. Utilization of organometallic chemical vapor deposition (OMCVD) for lateral overgrowth would offer two important advantages over the halide technique. First, since OMCVD does not use HCl, it can be used with reactants or substrates that are adversely affected by reaction with HCl. Second, OMCVD permits convenient deposition of layers of ternary and quaternary alloys. In this report we describe the first observations of lateral epitaxial overgrowth by OMCVD.

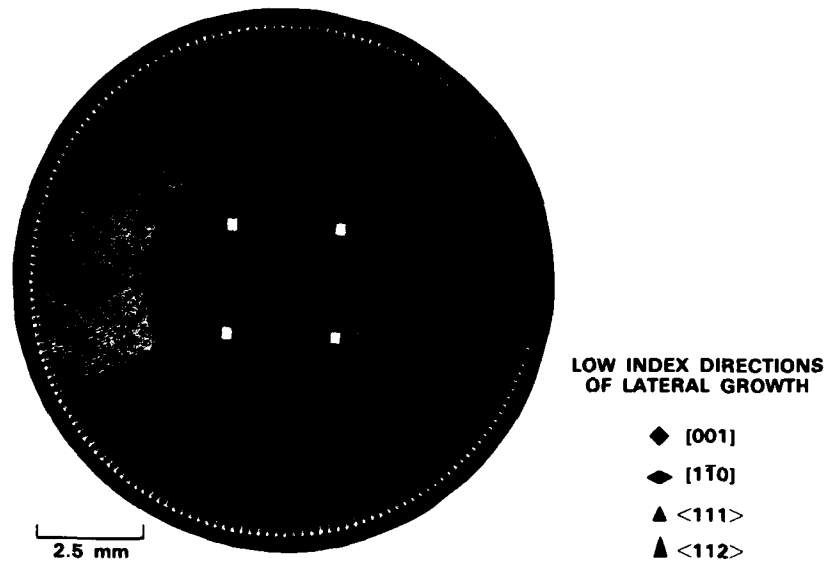
The system used for OMCVD growth of GaAs is typical of reactors employing RF induction heating.⁽⁵⁾ The quartz reactor tube is mounted horizontally, and the upper surface of the graphite susceptor is parallel to the reactor tube and gas flow. Trimethylgallium (TMGa) is maintained at constant temperature in a bubbler with hydrogen used as the carrier gas. The arsenic source is a 5% mixture of arsine in hydrogen. The streams of each source and carrier gas, which are electronically controlled, are combined in a manifold before entering the reactor at atmospheric pressure.

The substrates were GaAs (110) wafers. After being polished, cleaned, and etched, each had 1000 Å of CVD SiO_2 deposited on its front surface. A pattern of narrow stripes was then opened in the oxide by standard photolithographic techniques. Lateral overgrowth was investigated for growth temperatures between 680°C and 850°C and for growth times between 15 and 120 minutes. The TMGa mole fraction was normally 1.2×10^{-4} , which gave an average vertical growth rate of 3 $\mu\text{m/h}$, and the AsH_3 mole fraction was normally 3.6×10^{-3} .

To investigate the dependence of overgrowth on the orientation of the stripe openings in the SiO_2 with respect to the substrate, we used an oxide test pattern formed by etching 360 pairs of parallel stripe openings 3 μm wide and 20 μm apart, indexed at 1° intervals, which radiated from a central circle where the SiO_2 remained intact.⁽⁶⁾ Figure 3-1(a) is a photograph of the surface of a patterned sample after a GaAs growth run at 750°C . The lateral growth is strongly orientation-dependent, exhibiting the double twofold symmetry of the (110) plane. The light areas in Fig. 3-1(a) are smooth GaAs surfaces, the gray areas are SiO_2 , and the fine dark spots in the gray areas are polycrystalline GaAs nucleated directly on the SiO_2 .

To determine the quantitative dependence of lateral growth on orientation, we measured the total width of the GaAs layer originating within each stripe opening. Figure 3-1(b) is a polar plot showing these widths as a function of the angular positions of the openings. Overgrowth minima occur for openings corresponding to the 12 low-index growth directions indicated in Fig. 3-1(a), with the least overgrowth for the two [110] openings, which have their long axis normal to the [110] direction. For the openings close to the two [001] openings, the surface morphology is rough. Maximum overgrowth and good surface morphology are obtained for the openings over the angle range between 2° and 26° on either side of the [110] openings. The largest ratio of lateral to vertical growth rates is 5.

After each growth run, cross sections of the overgrown layers were prepared by etching the GaAs from an annular ring concentric with the test pattern. Figures 3-2(a) and 3-2(b) are scanning electron micrographs showing such cross sections for two layers, with angles of 4° from a [110] opening and 4° from a [111] opening, which were grown on the same substrate at 700°C for 21 min. In Fig. 3-2(a) the etch completely removed the GaAs layer from the annular ring, revealing the 3 μm opening in the SiO_2 and the GaAs underneath. The layer in Fig. 3-2(b) was thicker, however, and some of the layer remained to obscure the opening. Although the two layers had different vertical growth rates, they had the same volume, as given by the product of their height and width. This observation implies that the volume of material deposited was limited by mass transport in the gas phase.



(a) PHOTOGRAPH AFTER GROWTH FOR 18 min AT 750°C

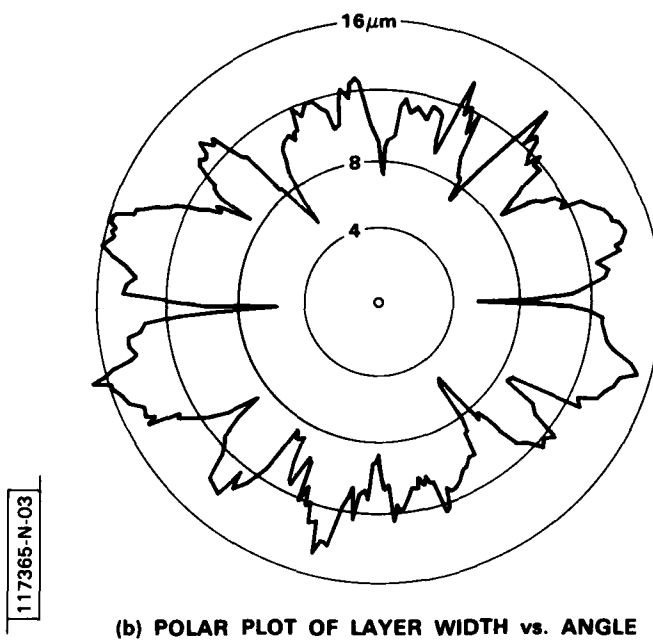


Fig. 3-1. OMCVD growth of GaAs on patterned substrate. Light squares in central circle and at pattern perimeter are GaAs deposits formed by vertical epitaxial growth on exposed square areas of the substrate.



→ / ← 3 μm
(a) 4° CLOCKWISE FROM [110]



→ / ← 3 μm
(b) 4° COUNTERCLOCKWISE FROM [111]

Fig. 3-2. Scanning electron micrographs at 87° tilt, showing cross sections of GaAs layers with lateral growth directions of 4° clockwise from [110] and 4° counter-clockwise from [111]. Upper area of each micrograph shows as-grown surface. Layers were grown for 21 min. at 700°C.

Figure 3-2 has two other significant features. First, both layers exhibit faceted growth. Second, for each layer the lateral growth rates are different on the two sides of the stripe opening. These features, as well as the orientation dependence illustrated in Fig. 3-1, show that the rate of two-dimensional growth by OMCVD is limited by surface kinetics, as well as by mass transport in the gas phase. As in the case of the $\text{AsCl}_3\text{-GaAs-H}_2$ process, lateral growth by OMCVD is a consequence of the orientation dependence of growth rate associated with surface kinetics. However, there is a significant difference between the two growth processes. In the halide process, there is a dynamic equilibrium between the solid and gas phases, and the dependence of the attachment kinetics on orientation makes an important contribution to lateral growth. In the OMCVD process, the sticking coefficient for Ga is unity, so that the attachment kinetics are independent of orientation. Once deposited, the Ga atoms can diffuse along the top and side surfaces of the growing layer before their incorporation at fixed lattice sites. Lateral overgrowth and faceting result because the diffusing atoms are preferentially incorporated into the different GaAs crystallographic surfaces.

The effect of temperature on lateral growth by OMCVD is shown in Fig. 3-3, where the total width of the GaAs layer obtained by growth for 15 min. is plotted against temperature for the $[110]$ stripe opening and for two non- $[110]$ openings. Below 700°C , lateral growth decreases because of competition from polycrystalline GaAs deposits that are formed on the SiO_2 film between the openings. Above 700°C , the lateral growth rate for the $[110]$ opening is almost independent of temperature because vertical growth is also taking place in a $\langle 110 \rangle$ direction. In this range the rates for the other openings decrease toward the $[110]$ value with increasing temperature, consistent with surface-kinetic-limited growth.

Our primary motivation for investigating overgrowth by OMCVD is to develop a method for fabricating ultrathin, wide-bandgap photovoltaic cells by the CLEFT (cleavage of lateral epitaxial films for transfer) process.^(1,2) Bonding one or two such cells to a lower bandgap cell would yield a cascade structure that could have conversion efficiencies up to 30% at AM1.⁽⁷⁾

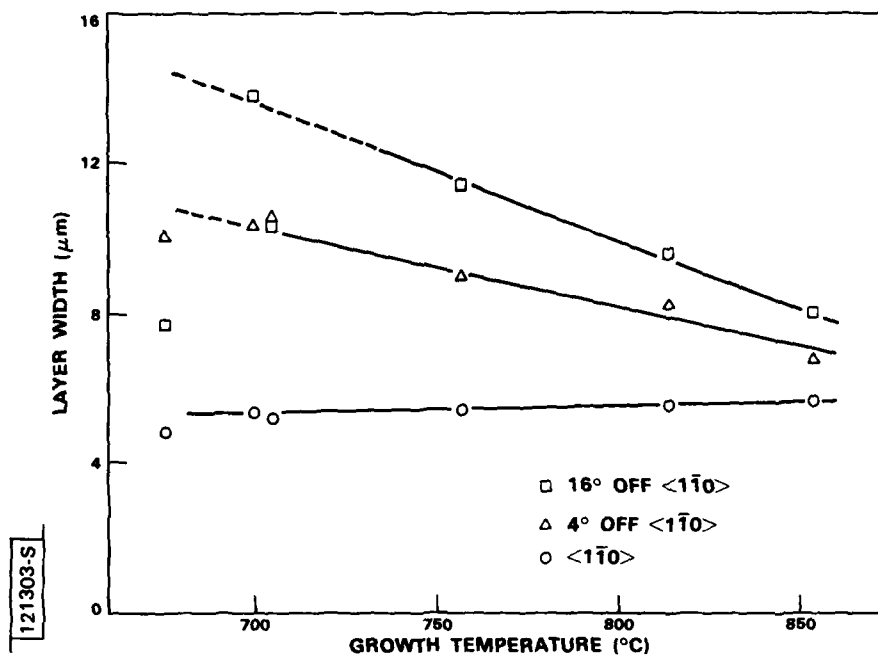


Fig. 3-3. Width of GaAs layers obtained by growth for 15 min, plotted as a function of growth temperature for three lateral growth directions. Dashed line is layer width in absence of GaAs nucleation on SiO_2 .

In an initial experiment to demonstrate the applicability of OMCVD to the CLEFT process, we used a substrate mask consisting of successive films of carbonized photoresist and $\text{SiO}_2^{(6)}$ patterned with parallel $4\text{-}\mu\text{m}$ openings, on $10\text{-}\mu\text{m}$ centers, for lateral growth at 20° from $[110]$. A smooth, continuous epitaxial layer $3\text{ }\mu\text{m}$ thick was obtained by growth at 750°C for 67 min. This layer, which measured $1.0 \times 1.6\text{ cm}$, was bonded to a $250\text{-}\mu\text{m}$ -thick glass substrate and cleaved intact from the GaAs substrate.

On the basis of our observations of lateral OMCVD growth of GaAs, it is very probable that such growth can also be achieved for the other III-V compounds and alloys (e.g., $\text{Ga}_{1-x}\text{Al}_x\text{As}$) that have been prepared by OMCVD. Lateral overgrowth structures incorporating these materials could have a variety of important applications, including waveguides for optical signal processing and semiconductor-on-insulator devices for high-speed operation.

R.P. Gale J.C.C. Fan
R.W. McClelland C.O. Bozler

3.2 Liquid-Encapsulated Czochralski Growth of InP Crystals from In-Rich Melts

The growth of InP crystals by the liquid-encapsulated Czochralski (LEC) method has been described in an earlier report.⁽⁸⁾ As starting material we use polycrystalline InP synthesized from the elements in the form of nominally undoped, n-type ingots produced by directional solidification of In-rich solutions under controlled P pressure. If the crystals are not intentionally doped, they too are n type, but at 77 K the electron concentration n_{77} is always higher and the mobility μ_{77} always lower for the pulled crystals than for the charge material.

We have recently been investigating the LEC growth of nominally undoped InP boules from charges prepared by adding elemental In to polycrystalline ingot material. As the In content of the melt is increased, there is a marked decrease in n_{77} and increase in μ_{77} . For one sample, μ_{77} is $5.7 \times 10^4 \text{ cm}^2 \text{ V}^{-1} \text{ s}^{-1}$, the highest value reported to date for any LEC InP crystal. In experiments at magnetic fields up to 15 T, we found that the Hall coefficient at room temperature exhibits the field dependence characteristic of homogeneous samples. This observation indicates that the changes in carrier concentration and mobility with increased In content of the melt are due to a reduction in donor concentration, rather than to measurement anomalies resulting from the presence of In inclusions.

For "nonstandard" boules grown from charges to which elemental In has been added, as well as for "standard" boules grown from charges consisting of polycrystalline ingot material without added In, we use LEC growth conditions similar to those described previously.⁽⁸⁾ The nonstandard charges weigh from 100 to 200 g, the standard ones generally from 250 to 300 g. The nonstandard boules usually consist of 4 to 10 large grains, although we believe that a high yield of single-crystal boules could be grown from In-rich melts by optimizing the growth conditions, particularly the temperature gradient at the crystal-melt interface.

In the first experiments using In-rich melts, three boules were grown from charges in which the atom fraction of In (x in $\text{In}_x \text{P}_{1-x}$) was nominally 0.56. The nominal values of x are calculated by taking the polycrystalline

ingot material to be stoichiometric, with $x = 0.5$, although the ingots contain a small amount of metallic In occluded at grain boundaries. Table 3-1 lists the values of room temperature carrier concentration (n_{300}), n_{77} , and μ_{77} found by resistivity and low-field Hall coefficient measurements on single-crystal samples cut from the first-to-freeze portions of these nonstandard boules, together with the corresponding values for the two standard boules grown just before them. (Values of the room temperature mobility have not been tabulated since these values are essentially the same for all samples.) For the nonstandard boules, n_{300} and n_{77} are considerably lower and μ_{77} considerably higher than the values for the standard boules. Even the lowest μ_{77} for any of the nonstandard boules, $4.2 \times 10^4 \text{ cm}^2 \text{V}^{-1} \text{s}^{-1}$, is equal to the highest value obtained for any of the more than 40 standard boules we have grown to date. The highest μ_{77} , $5.7 \times 10^4 \text{ cm}^2 \text{V}^{-1} \text{s}^{-1}$, significantly exceeds the value of $4.7 \times 10^4 \text{ cm}^2 \text{V}^{-1} \text{s}^{-1}$ measured for the test sample that was cut from the polycrystalline ingot used to provide starting material.

Table 3-1				
ELECTRICAL PROPERTIES OF InP BOULES				
LEC boule	Melt composition (atom fraction In)	n_{300} (10^{15} cm^{-3})	n_{77} (10^{15} cm^{-3})	μ_{77} ($10^4 \text{ cm}^2 \text{V}^{-1} \text{s}^{-1}$)
442	0.5	4.9	3.8	3.1
449	0.5	4.5	3.9	3.5
452	0.56	2.7	2.0	5.7
454	0.56	2.5	2.3	4.2
455	0.56	2.9	2.5	4.6

To make a more detailed study of the effect of melt composition on the electrical properties of the LEC boules, three successive growth runs were made using charge material from the same polycrystalline ingot, with In being added to the charge for the first and third runs. For a test sample cut near the first-to-freeze end of the ingot, n_{77} was $6.8 \times 10^{14} \text{ cm}^{-3}$, and μ_{77} was $6.4 \times 10^4 \text{ cm}^2 \text{ V}^{-1} \text{ s}^{-1}$. Since there is generally an increase in n_{77} and a decrease in μ_{77} with increasing distance from the first-to-freeze end of such an ingot, the ingot was cut into three side-by-side longitudinal sections, and one section was used for each run. After completion of each run, samples for electrical measurements were cut near the top, middle, and bottom of the boule. For the two nonstandard boules, the melt composition corresponding to each sample location was calculated from the weights of the polycrystalline charge material, the In added to the charge, and the portion of the boule that had solidified, taking both the polycrystalline material and the grown boule to be stoichiometric.

The results for the three additional boules, which are given in Table 3-2, confirm the dependence of electrical properties on melt composition. All the values of n_{300} and n_{77} are much lower and all the values of μ_{77} much higher for the nonstandard boules than for the standard boule. Furthermore, the carrier concentrations decrease and the mobility increases from the top to the bottom of the nonstandard boules (except that n_{77} is slightly lower for the middle sample of boule 470 than for the top sample). This variation can be attributed to the increase in the In content of the melt as the boule solidifies, since the opposite variation in carrier concentration and mobility is exhibited by the standard boule and by all other standard boules for which we have data. The variation along a standard boule occurs because impurities with distribution coefficients of less than unity segregate toward the bottom of the boule.

To find an explanation for the difference in electrical properties between the nonstandard and standard boules, we have investigated the possibility that the values of the Hall coefficient R_H measured at low fields for the nonstandard boules are anomalously high (i.e., $R_H > 1/ne$) because these boules contain metallic In inclusions incorporated during their

Table 3-2 ELECTRICAL PROPERTIES OF InP BOULES GROWN FROM SAME CHARGE MATERIAL						
Boule	Sample	Melt composition (atom fraction In)	n_{300} (10^{15} cm^{-3})	n_{77} (10^{15} cm^{-3})	μ_{77} ($10^4 \text{ cm}^2 \text{ V}^{-1} \text{ s}^{-1}$)	
470	T	0.58	2.5	2.2	4.9	
	M	0.62	2.5	2.1	4.8	
	B	0.65	2.0	1.7	5.6	
471	T	0.5	4.9	4.0	3.2	
	M	0.5	5.4	4.1	2.8	
	B	0.5	6.1	4.8	2.7	
472	T	0.61	2.4	1.9	4.1	
	M	0.65	1.7	1.5	5.1	
	B	0.67	1.6	1.3	5.5	

growth from the In-rich melts. For GaAs, it has been found that Ga inclusions can result in such anomalous R_H values in which case the magnetic field dependence of R_H is also anomalous.⁽⁹⁾ We have therefore measured R_H at room temperature as a function of field for samples from both nonstandard and standard boules. The results for one sample of each type are shown in Fig. 3-4, where the ratio of R_H at each field to R_H at 15 T is plotted against field.

The two plots in Fig. 3-4, which are almost identical, have the form characteristic of a homogeneous semiconductor. We conclude that the improvement in the electrical properties of the nonstandard boules is not due to the presence of In inclusions that result in measurement anomalies. Our failure to find any opaque areas when we examined samples from these boules using an infrared microscope with a resolution of 1-2 μm is consistent with this conclusion. Therefore the reduction in carrier concentration and increase in mobility for the nonstandard boules can be attributed to a change

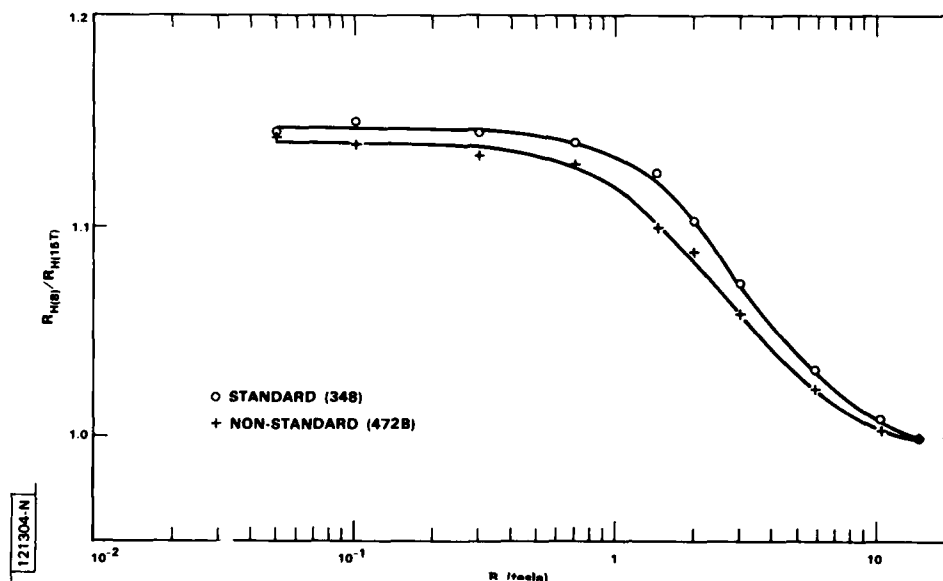


Fig. 3-4. Room temperature Hall coefficient ratio $R_H(B)/R_H(15T)$ vs. magnetic field B for two InP samples.

in the concentration of electrically active centers--in particular, to a reduction in the concentration of shallow donors. The degree of acceptor compensation is so low in both standard and nonstandard boules that the change in acceptor concentration, if any, cannot be determined from the carrier concentration and mobility data. The identity of the donor or donors associated with the change in electrical properties has not been established. One possibility is the native antisite defect consisting of a P atom located on an In site, whose concentration will be reduced by growth from an In-rich melt. The other principal possibility is an impurity, such as Si, that is a donor when located on an In site.

G.W. Iseler
M.S. Taylor
J.V. Pantano
E.J. Delaney

3.3 Simultaneous Formation of a Shallow Silicon p-n Junction and a Shallow Silicide/Silicon Ohmic Contact by an Ion Implantation Technique

The stable and reliable characteristics of silicide-Si contacts have led to increasing use of silicides as metallization materials in integrated electron devices. Unfortunately, such contacts formed by thermal annealing of as-deposited refractory metal films on Si generally exhibit poor surface morphology and irreproducible electrical characteristics, because native oxides at the metal-Si interface interfere with silicide formation.⁽¹⁰⁾ However, the effect of interface contamination can largely be suppressed by ion implantation through the metal-Si interface.⁽¹¹⁻¹³⁾ Implantation leads to dispersion of impurity atoms at the interface and also to intermixing of the metal and Si. Uniform silicide layers with smooth surface morphology can then be obtained by annealing.⁽¹¹⁻¹⁴⁾

In this report we describe a new technique, based on the ion implantation method, that produces both a shallow silicide/Si ohmic contact and a shallow Si p-n junction located directly below the contact. The principle of the technique is illustrated in Fig. 3-5. A p-Si substrate is coated with a thin layer of a refractory metal, then with several pairs of

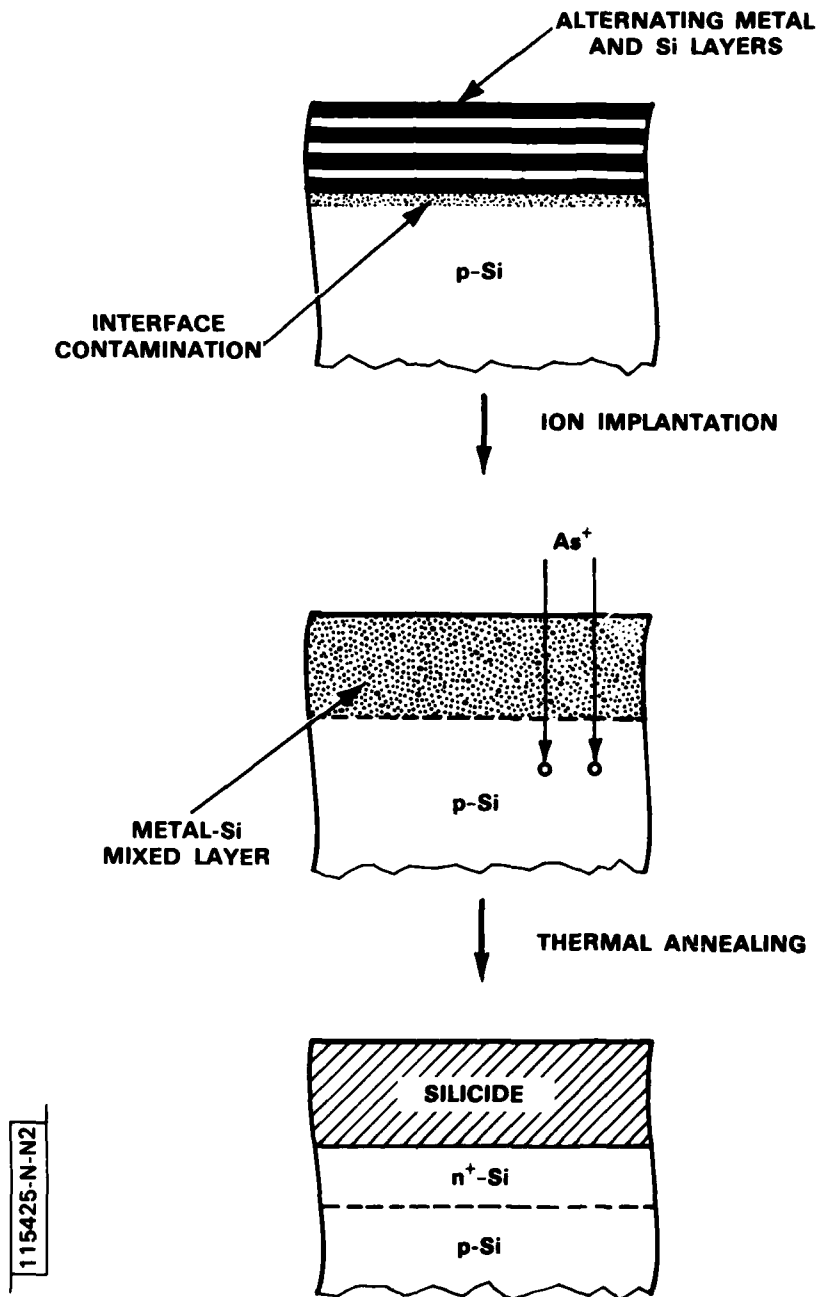


Fig. 3-5. Formation of shallow silicide/Si contact and shallow p-n junction by ion implantation followed by thermal annealing.

alternating layers of Si and the metal. to form the structure shown in the top diagram. For the paired layers, the ratio of Si to metal thickness is chosen to yield the composition of the desired silicide phase. A similar metal-Si structure has been utilized for the formation of shallow PtSi/Si Schottky barrier contacts.⁽¹⁵⁾ With this structure the depth of the silicide/Si contact is fixed by the thickness of the first metal layer, which determines the thickness of Si that will be consumed from the substrate in silicide formation, while the total thickness of silicide can be adjusted by varying the number of paired layers. Next, the coated Si substrate is bombarded with As⁺ ions having sufficient energy to penetrate the substrate. As shown in the middle diagram, this bombardment causes intermixing of the metal and Si layers, dispersion of the contaminant atoms at the interface between the first metal layer and the substrate, and implantation of As ions in the substrate. Finally, the sample is thermally annealed under conditions that result in the formation of the silicide from the metal-Si mixture and simultaneously in the formation of a thin n-Si layer by activation of the implanted As donors, as shown in the bottom diagram. The depth of the p-n junction can be adjusted by varying the initial energy of the As⁺ ions and/or the thickness of the metal and Si layers.

The refractory metal used in the present experiments was tungsten (W). The Si substrates were 2-inch-diameter, 1 Ω -cm p-type, (100) wafers. The wafers were chemically cleaned by conventional procedures, rinsed in dilute HF (100:1), and loaded in a single e-gun, multihearth evaporation system. A W layer approximately 50 Å thick and three pairs of alternating Si layers (~250 Å) and W layers (~100 Å) were deposited sequentially without breaking the vacuum. The thickness ratio of 2.5 corresponds to the composition WSi₂. The samples were then implanted with 180-keV As⁺ ions to a dose of $1 \times 10^{16} \text{ cm}^{-2}$ at room temperature or at ~350°C. The implanted samples were annealed at 600°C for 30 min and subsequently at 950°C for 30 min in a quartz-tube furnace with flowing N₂ ambient. P-n junction mesa diodes were fabricated on several wafers.

According to x-ray diffraction data for the as-deposited W and Si layers, the former are polycrystalline while the latter are amorphous. Rutherford backscattering (RBS) measurements show that As^+ ion implantation causes complete intermixing of these layers. In fact, according to electron diffraction data, implantation results in the formation of WSi_2 , which is amorphous for samples implanted at room temperature and polycrystalline for those implanted at 350°C . (Thus Fig. 3-5 is oversimplified, since it indicates that silicide formation does not take place until post-implantation annealing.)

A TEM micrograph and an electron diffraction pattern of the WSi_2 phase are shown in Fig. 3-6(a) for a room temperature sample and in Fig. 3-6(b) for a 350°C sample. The grain size in the 350°C sample ranges from 150 to 400 Å. The diffraction pattern for this sample shows that the WSi_2 formed is not the stable tetragonal phase⁽¹⁶⁾ but a hexagonal phase (probably metastable) that appears to be isostructural with a hexagonal phase reported for MoSi_2 .⁽¹⁷⁾ The electron diffraction pattern for the amorphous WSi_2 obtained by room temperature ion bombardment consists of a strong halo centered around $2\theta = 42^\circ$ and a weak halo centered around $2\theta = 27^\circ$. These angles are the same as those for the strongest and second strongest lines for the hexagonal phase, indicating that the short-range order is similar for the amorphous and hexagonal phases.

Annealing of the implanted samples at 600°C results in transformation of the amorphous WSi_2 into the hexagonal phase, while the hexagonal phase in the 350°C samples remains unchanged in structure. Subsequent annealing at 950°C leads to transformation of the hexagonal phase in both room temperature and 350°C samples into the stable tetragonal phase. Figure 3-7(a) shows a TEM micrograph and an electron diffraction pattern of the tetragonal phase, which has a grain size of 500 to 800 Å. The As^+ ion implantation produces an amorphous layer in the Si substrate adjacent to the WSi_2/Si interface. Annealing causes recrystallization of this layer and activation of the implanted As donors to form an n^+ region. A TEM micrograph and an electron diffraction pattern of the recrystallized layer, obtained after removing the

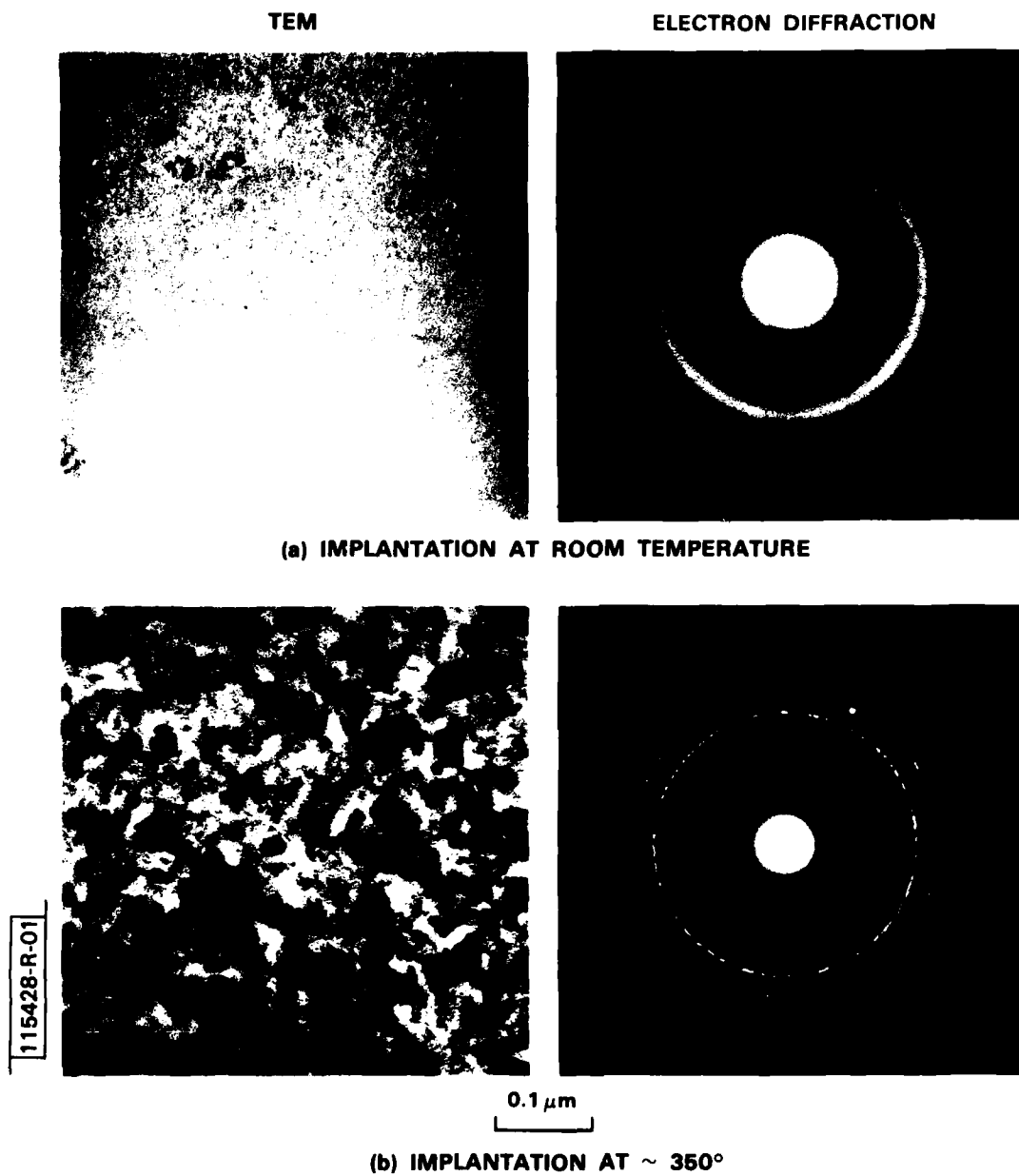


Fig. 3-6. TEM micrographs and electron diffraction patterns of (a) amorphous WSi_2 phase obtained by implantation at room temperature and (b) hexagonal polycrystalline WSi_2 phase obtained by implantation at $\sim 350^\circ\text{C}$.

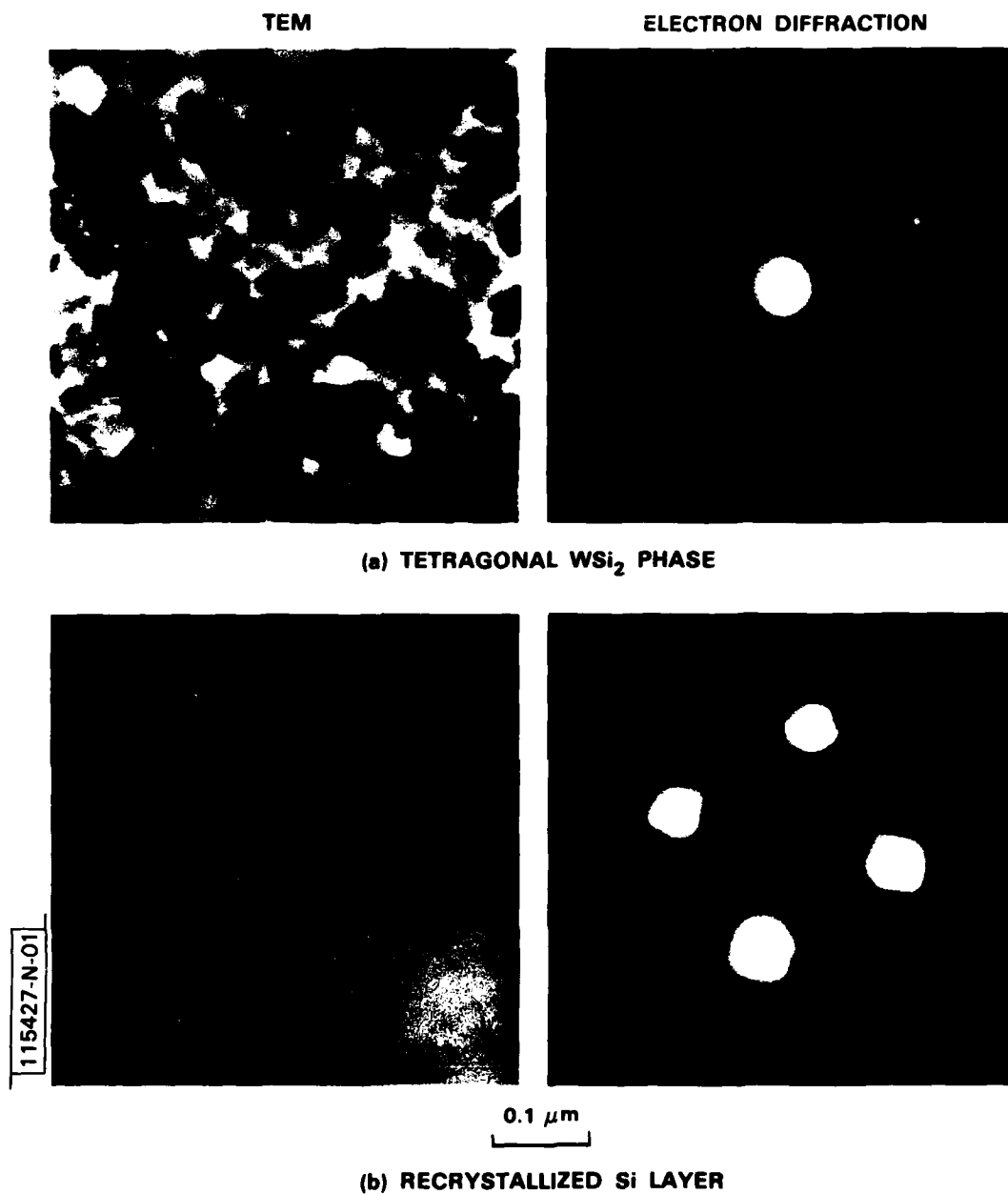


Fig. 3-7. TEM micrographs and electron diffraction patterns of (a) tetragonal WSi_2 phase obtained by annealing and (b) recrystallized Si layer.

WSi₂ by selective etching, are shown in Fig. 3-7(b). No defects are detected in this layer by TEM. RBS measurements made after annealing indicate that the WSi₂/Si interface is sharp, with a depth of about 150 Å, which is the calculated thickness of Si consumed in forming WSi₂ by reaction with the 50 Å layer of W initially deposited on the substrate. The RBS measurements also indicate that annealing resulted in a slight diffusion of the As atoms into the substrate. The estimated depth of the p-n junction, obtained by extrapolating the RBS data for As, is about 0.2 μm below the WSi₂/Si interface.

Figure 3-8 shows the I-V characteristics of an unpassivated p-n junction mesa diode, 380 μm in diameter, that was fabricated from a wafer with the WSi₂/n⁺-Si(As)/p-Si<100> structure. Closely similar characteristics were measured for more than 50 such devices randomly selected from several wafers. Over the current range from 10⁻¹⁰ to 10⁻⁴ A, the forward characteristic fits the expression $I = I_0 [\exp(qV/nkT) - 1]$ with $n = 1.15$. The near-unity value of n indicates that the junction is of good quality, with current transport dominated by diffusion. The reverse current density is 7×10^{-8} A/cm² at -10 V, and the breakdown voltage exceeds -30 V. The generation lifetime deduced from the reverse current density is ~1.3 μs, which should be considered a lower limit since the diode was unpassivated. The relatively high lifetime value confirms the high junction quality.

The ion implantation technique should be useful in the fabrication of metal-oxide-semiconductor field-effect transistors for large-scale integrated circuits. In these devices, shallow source and drain p-n junctions are necessary in order to reduce the short-channel effects frequently observed in small-dimension devices. Moreover, the use of silicide contacts is desirable to reduce transistor size and hence increase packing density and speed.⁽¹⁴⁾

B-Y. Tsaur
C.H. Anderson, Jr.

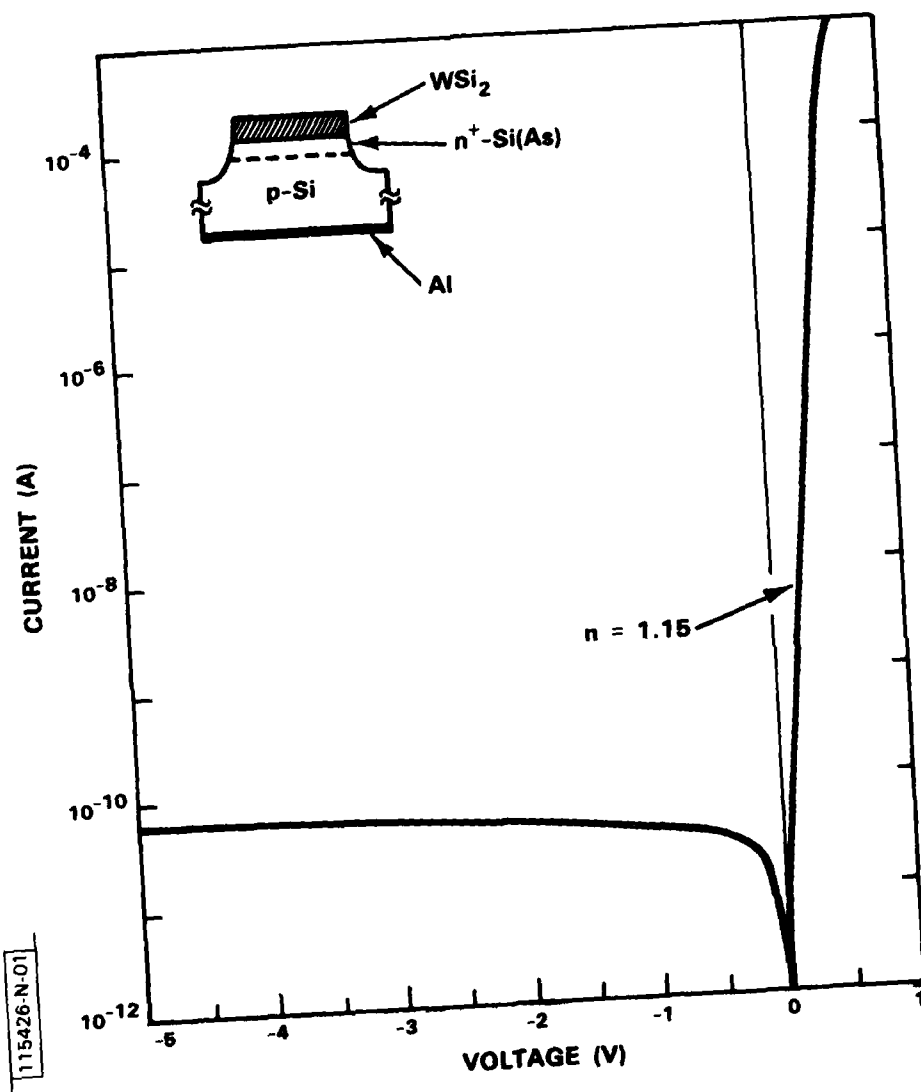
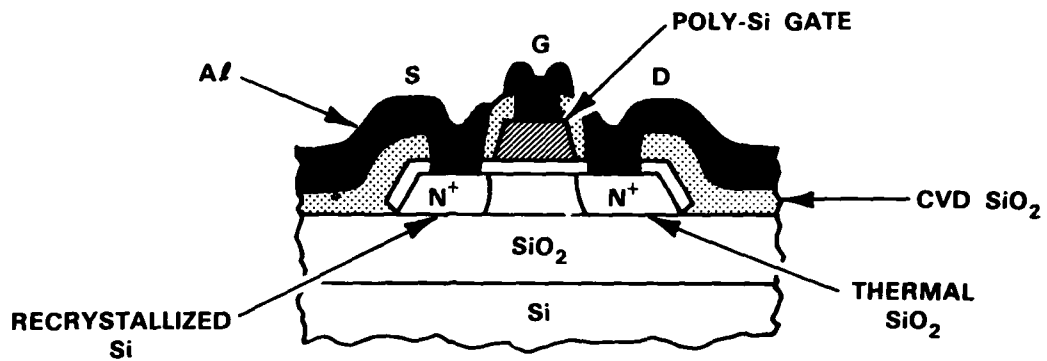


Fig. 3-8. I-V characteristics of typical mesa diode fabricated from wafer with WSi₂/n⁺-Si (As)/p-Si<100> structure.

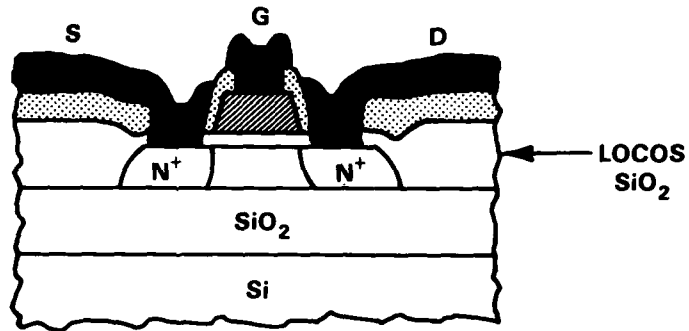
3.4 Effects of Ionizing Radiation on N-Channel MOSFETs Fabricated in Zone-Melting-Recrystallized Si Films on SiO₂-Coated Si Substrates

As part of a program to develop silicon-on-insulator technology utilizing Si films prepared by zone-melting recrystallization of poly-Si deposited on SiO₂-coated Si substrates, we recently investigated the effects of ionizing radiation on the electrical characteristics of metal-oxide-semiconductor field-effect transistors (MOSFETs) fabricated in such recrystallized Si films.⁽¹⁸⁾ For devices in which the active region was defined by complete-island-etch (CIE) isolation, it was found that the adverse consequences of irradiation with 1.5-MeV electrons could be largely suppressed by applying a moderate negative bias to the Si substrate during irradiation and device operation in order to reduce the effect of charge trapping in the SiO₂ coating. In an extension of the earlier investigation, we have now obtained similar results for irradiation with Co-60 γ -rays and for MOSFETs with local-oxidation-of-Si (LOCOS) isolation. To make a more detailed study of the manner in which radiation effects are suppressed by substrate biasing, we have also measured the electrical properties of CIE- and LOCOS-isolation devices for which the substrate was biased only during irradiation or only during device operation.

N-channel MOSFETs with a gate width of 50 μm were fabricated in the zone-melting-recrystallized Si films, and also in the Si films of commercial silicon-on-sapphire (SOS) wafers, by a technique described previously.⁽¹⁸⁾ Figure 3-9 schematically shows the structures of the recrystallized-Si devices with CIE and LOCOS isolations. The MOSFETs were irradiated with either a 1.5-MeV electron beam from a Van de Graaff generator or γ -rays from a Co-60 source. The electron doses ranged from 3×10^{10} to $3 \times 10^{13} \text{ cm}^{-2}$, corresponding to ionizing doses from 10^3 to 10^6 rad(Si) . The γ -ray dose was fixed at 10^6 rad(Si) . During irradiation the devices were biased with drain voltage $V_D = 5 \text{ V}$ and gate voltage $V_G = 0 \text{ V}$. For the recrystallized-Si devices, the substrate voltage V_B was 0 or -15 V. Subthreshold leakage current and threshold voltage measurements were performed within 20 min. after exposure. Unless otherwise noted, the V_D and V_B values were the same during the measurements as during irradiation.



(a) CIE ISOLATION



(b) LOCOS ISOLATION

Fig. 3-9. Schematic of MOSFETs fabricated in recrystallized Si films on SiO_2 by CIE and LOCOS isolations.

Figure 3-10 shows typical subthreshold source-drain I-V characteristics before and after electron irradiation for 6- μm -gate-length LOCOS-isolation SOS and recrystallized-Si MOSFETs. Similar results were obtained for devices irradiated with γ -rays. After 10^6 rad(Si) irradiation, the SOS device exhibits a three-order-of-magnitude increase in the leakage current, a significant increase in subthreshold slope, and a knee in the I-V curve. For the recrystallized-Si devices, the characteristics depend strongly on whether the substrate was biased. For a dose of 10^6 rad(Si), the devices with $V_B = 0$ become extremely leaky and cannot be turned off even with a large negative gate bias. For the same dose, the subthreshold slope for the devices with $V_B = -15$ V remains sharp and the leakage current remains in the pA range. The effect of irradiation is only a little greater than that observed when the same substrate bias was applied to similar CIE-isolation devices.

For the recrystallized-Si MOSFETs, as well as for the SOS devices, exposure to ionizing radiation produces an increase in leakage current

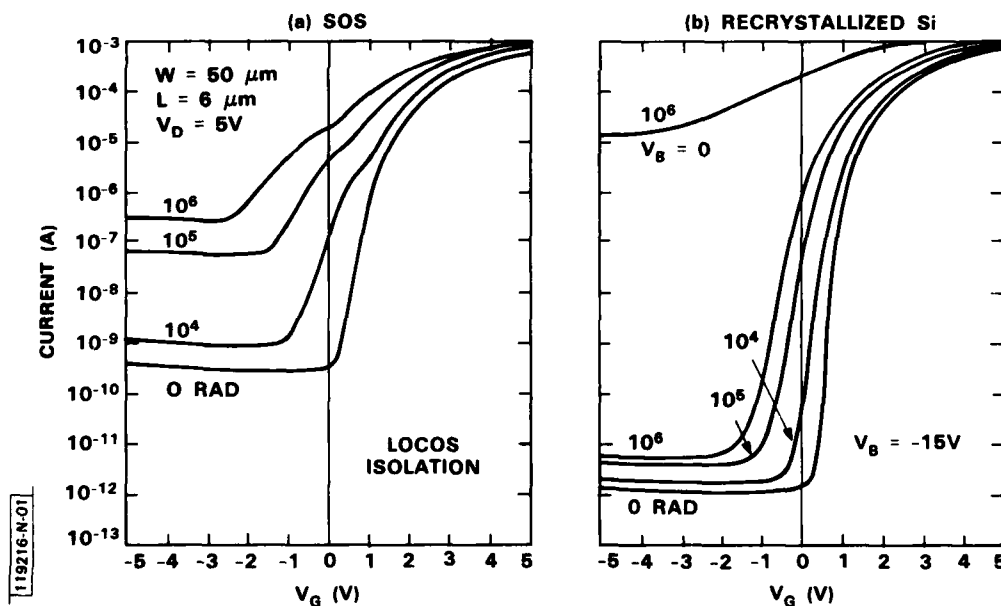


Fig. 3-10. Subthreshold source-drain current vs. gate voltage before and after irradiation of LOCOS-isolation SOS and recrystallized-Si MOSFETs.

because the insulating layer below the Si film (and surrounding the Si film, for the LOCOS-isolation devices) becomes positively charged, inducing a conducting inversion channel in the Si near the Si-insulator interface. Positive charging occurs because holes generated by the radiation are more readily trapped than the more mobile electrons, which are largely swept out of the insulator by the electric field between the source and drain.

For the recrystallized-Si MOSFETs, as discussed previously,⁽¹⁸⁾ applying a moderate negative bias to the Si substrate has two effects that together greatly reduce the increase in leakage current produced by ionizing radiation. First, because of the electric field due to the bias, more of the holes generated by the radiation are removed from the SiO₂ layer before they can be trapped, so that the density of positive charge in the layer is reduced. Second, during device operation, the electric field counteracts the tendency of the trapped positive charge to induce an inversion channel in the Si film.

To assess the two effects of substrate bias separately, we have performed a series of experiments on recrystallized-Si MOSFETs in which the substrate was biased during irradiation but not during measurement and vice versa. The results obtained after 10⁶ rad(Si) are summarized in Table 3-3. For the CIE-isolation devices, as shown schematically in Fig. 3-11(a), biasing during irradiation almost eliminates charge trapping in the SiO₂ layer below the Si film, since in this case the leakage current was almost as low when the substrate was not biased during measurement as when it was. For such devices that are not biased during irradiation, an electric field applied during measurement is very effective in counteracting the trapped charge, since in this case the leakage current was only 10⁻¹⁰ A, compared to 10⁻⁵ A without substrate bias. For the LOCOS-isolation devices, on the other hand, substrate biasing during irradiation was much less effective in decreasing the amount of charge trapping, since the leakage current rose to 10⁻⁷ A when bias was applied during irradiation but not during measurement. We believe that in this case, as shown in Fig. 3-11(b), charge is trapped mainly in the edge oxides, where the applied field is expected to have much less influence on the motion of the holes generated by the radiation.

Table 3-3			
LEAKAGE CURRENT FOR RECRYSTALLIZED Si MOSFETs AFTER 10^6 RAD(Si) IRRADIATION			
V_B (V)		Leakage Current (A)	
During Irradiation	During Measurement	CIE Isolation	LOCOS Isolation
0	0	-5 10	-4 -5 10 -10
-15	0	-11 10	-7 10
0	-15	-10 10	-10 10
-15	-15	-11 -12 10 -10	-11 -12 10 -10

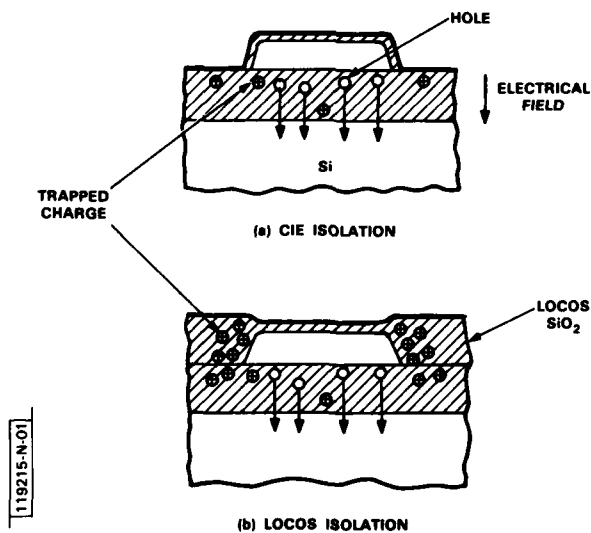


Fig. 3-11. Charge trapping in recrystallized-Si MOSFETs irradiated with substrate bias for CIE and LOCOS isolations.

However, a substrate bias applied to the LOCOS-isolation devices during measurement is very effective in counteracting the trapped charge in the edge oxides as well as in the SiO_2 layer below the Si film, since this bias reduced the leakage current to 10^{-10} A even when the substrate was not biased during irradiation, and to 10^{-11} - 10^{-12} A when it was. In any event, because in practice the substrate bias can be maintained during both irradiation and operation, low leakage currents can be achieved in both CIE-isolation and LOCOS-isolation MOSFETs.

B-Y. Tsaur
J.C.C. Fan
G.W. Turner
D.J. Silversmith

References

1. R.W. McClelland, C.O. Bozler, and J.C.C. Fan, Appl. Phys. Lett. 37, 560 (1980).
2. C.O. Bozler, R.W. McClelland, and J.C.C. Fan, Proceedings of the 8th International Symposium on GaAs and Related Compounds, Vienna, 1980 (Institute of Physics, London, 1981), p. 283.
3. F.J. Leonberger, C.O. Bozler, R.W. McClelland, and I. Melngailis, Integrated and Guided-Wave Optics Technical Digest (IEEE, New York, 1980), p. 28.
4. C.O. Bozler and G.D. Alley, IEEE Trans. Electron Dev. ED-27, 1128 (1980).
5. S.J. Bass, J. Cryst. Growth 31, 172 (1975).
6. C.O. Bozler, R.W. McClelland, J.P. Salerno, and J.C.C. Fan, J. Vac. Sci. Technol. 20, 720 (1982).
7. J.C.C. Fan, C.O. Bozler, and R.W. McClelland, Proceedings of the 15th IEEE Photovoltaic Specialists Conference, Kissimmee, Florida, 1981 (IEEE, New York, 1981), p. 666.
8. G.W. Iseler, J. Crystal Growth 54, 16 (1981); Solid State Research Report, Lincoln Laboratory, M.I.T. (1980:3), p. 21, DTIC AD-A094075.
9. C.M. Wolfe and G.E. Stillman, in Semiconductors and Semimetals, edited by R.K. Willardson and A.C. Beer (Academic Press, New York, 1975), Vol. 10, p. 175.

10. C.S. Petersson, J.E.E. Baglin, F.M. d'Heurle, J.J. Dempsey, J.M.E. Harper, C.M. Serrano, and M.Y. Tsai, in Thin-Film Interfaces and Reactions, edited by J.E.E. Baglin and J.M. Poate (Electrochemical Society, Princeton, 1980), p. 290.
11. B-Y. Tsaur and L.S. Hung, Appl. Phys. Lett. 37, 922 (1980).
12. S.W. Chiang, T.P. Chow, R.F. Reihl, and K.L. Wang, J. Appl. Phys. 52, 4027 (1981).
13. L.S. Wielunski, C-D. Kien, B-X. Liu, and M-A. Nicolet in Proceedings of Symposium on Metastable Materials Formation by Ion Implantation, edited by S.T. Picraux and W.J. Choyke, Materials Research Society Meeting, Boston 1981 (to be published).
14. M. Morimoto, E. Nagasawa, H. Okabayashi, and M. Kondo in Proceedings of the International Electron Devices Meeting, Washington, DC (1981), p. 655.
15. B-Y. Tsaur, D.J. Silversmith, R.W. Mountain, L.S. Hung, S.S. Lau, and T.T. Sheng, J. Appl. Phys. 52, 5243 (1981).
16. J.E.E. Baglin, J.J. Dempsey, W. Hammer, F.M. d'Heurle, C.S. Petersson, and C. Serrano, J. Electron. Mater. 8, 641 (1979).
17. For example, S. Yanagisawa and T. Fukuyama, J. Electrochem. Soc. 127, 1150 (1980).
18. B-Y. Tsaur, J.C.C. Fan, G.W. Turner, and D.J. Silversmith, IEEE Electron Dev. Lett. EDL-3, 195 (1982); Solid State Research Report, Lincoln Laboratory, M.I.T. (1982:2)

4. MICROELECTRONICS

4.1 Charge-Coupled Devices: Time-Integrating Correlator

A CCD implementation of a time-integrating correlator capable of high-speed operation was described in previous reports.^(1,2) In contrast to previously reported CCD correlators, most of which are really programmable transversal filters (PTFs), tap-weight errors in this TIC device can be removed by simple post-processing. In contrast, it is difficult if not impossible to remove these errors in a PTF because they become convolved with the (unknown) signal. Furthermore, this new device incorporates a unique balanced input structure which completely eliminates signal-dependent offsets and reduces reference-code-dependent offsets to a second order term.

A photomicrograph of this 5.9-mm-square chip is shown in Fig. 4-1. By combining on a single chip binary-analog charge multiplication, charge integration, and subtraction of the integrated bias charge, we have been able to fabricate the first reported all-CCD time-integrating correlator.

This report discusses preliminary electrical evaluation of some devices from the first run of wafers. All design features of the correlator have been verified at 5 MHz, including the clock levels which we predicted on the basis of simulations.⁽²⁾ An example of device operation at a code clock rate of 2 Mbps is shown in Fig. 4-2, which shows correlation and anti-correlation of a 511-bit M-sequence. In this case the correlator was clocked at 2 MHz and, therefore, provides correlations spaced one code bit apart. The integration time was 511 clock periods, so that the ideal correlation output would be a single peak with uniform sidelobes.

The extremely low level of fixed pattern noise, which is independent of the input signal (as shown in Fig. 4-2), can be removed by one of the schemes discussed in a previous report.⁽²⁾ Assuming that the pattern noise can be removed by such post-processing, the dynamic range of this device would be limited by the random thermal noise at the output. This residual noise has been measured to be at least 50 dB below the correlation peak, so that with appropriate fixed-pattern noise cancellation this device should be capable of excellent dynamic range.

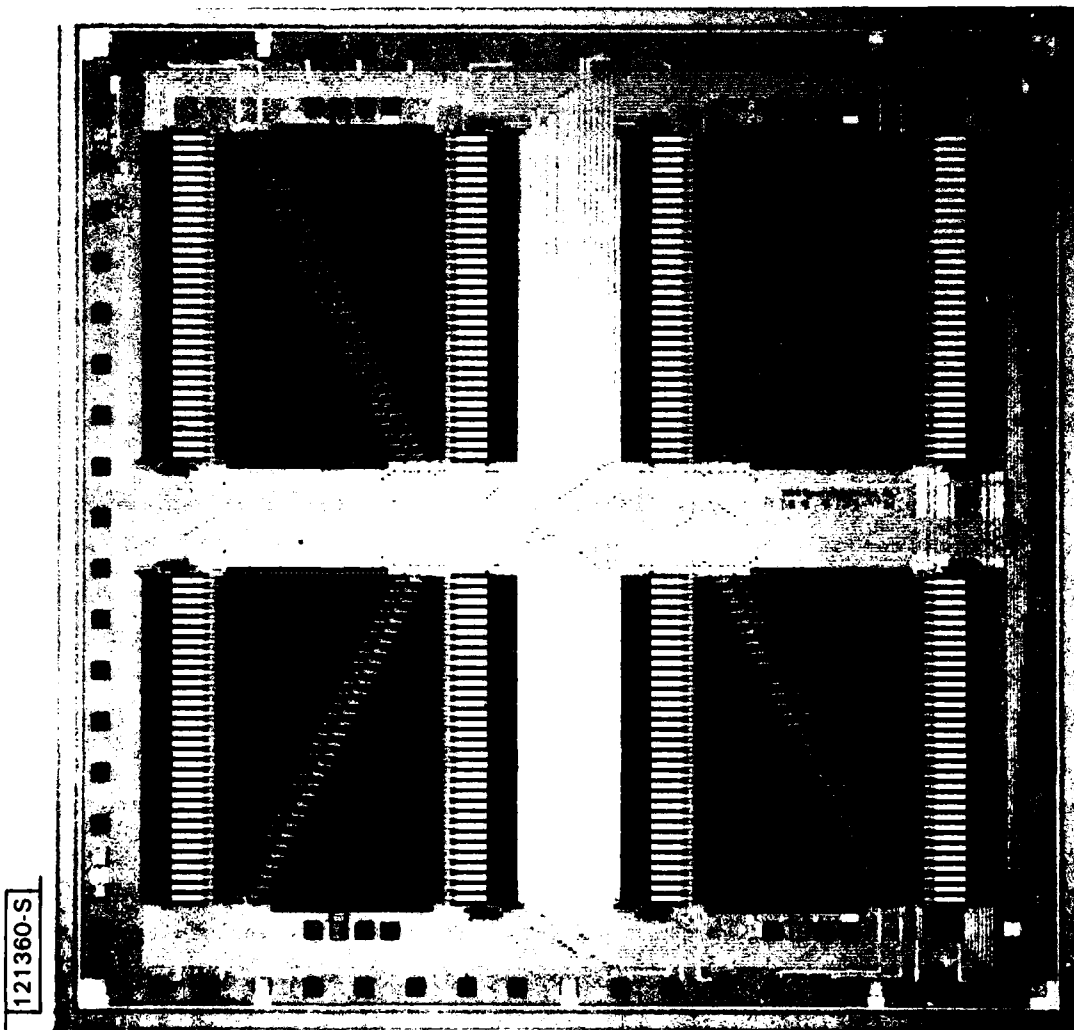


Fig. 4-1. Photomicrograph of CCD time-integrating correlator.

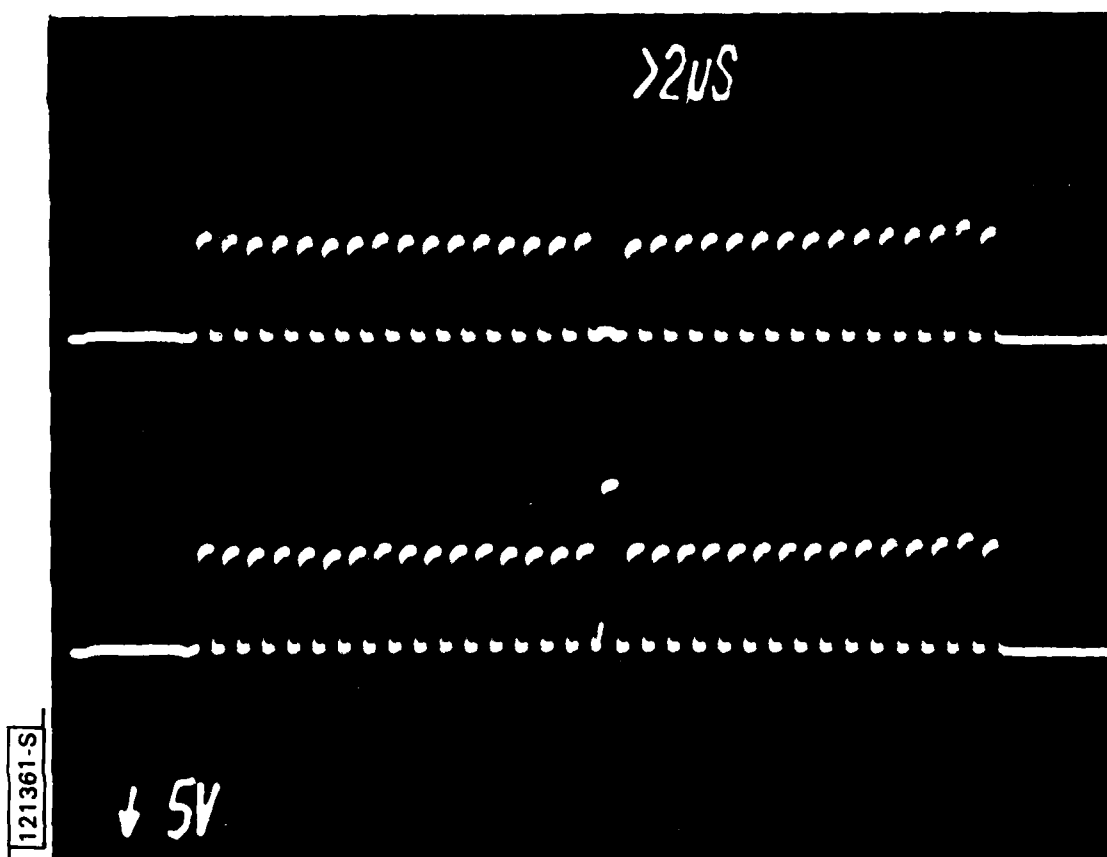


Fig. 4-2. CCD time-integrating correlator output waveform at an input data rate of 2 MHz. Output data rate is 1.4 MHz.

Although these devices were fabricated using a 25-MHz CCD chip architecture and wafer fabrication process, they could not be tested at frequencies higher than 5 MHz because the high clock capacitance (500 pF) of the eight correlators in parallel exceeded the capacitive drive capability of the available clock generators. Attempts to resonate this clock capacitance to 20 MHz with an inductor were frustrated by a parasitic series resistance of 10-20 ohms.

In the future we plan to attack this clocking problem on three fronts. The interconnect patterns on the chip can be modified to provide separate high-speed clocks for each pair of correlators. Further modification of the chip layout is expected to reduce the high-speed clock capacitance by about a factor of two. Finally, the source of the parasitic series resistance will be studied to make it feasible to use resonant sine-wave clocks.

B.E. Burke
D.L. Smythe

4.2 Dry Etching of Gold Using SF₆

One-micrometer-wide gaps have been etched in thin films of Au on GaAs substrates using SF₆ gas in a reactive ion etching (RIE) system. Although SF₆ has been used by others to etch Si, SiO₂ and W,^(3,4,5) this is the first use of this gas to etch either Au or the underlying GaAs. The process reported here is being developed for a self-aligned processing sequence for the fabrication of a GaAs power FET. Vertical wall profiles and clean and smooth etched surfaces have been achieved. An etch rate of ~150 Å/min for Au was obtained with a power density of 0.47 W/cm² at a pressure of 10 mTorr. Damage to the underlying GaAs surface by SF₆ etching has been evaluated and compared to the damage caused by Ar sputter etching. Because the dc bias voltage can be much lower when etching Au in SF₆, less damage to the GaAs is expected.

The RIE apparatus used in this experiment is shown schematically in Fig. 4-3. The positioning of the gas inlet on the side of the chamber is believed to cause the asymmetric profiles seen in both SF₆ and Ar etched samples. The system is initially pumped down into the 10⁻⁶ Torr range and

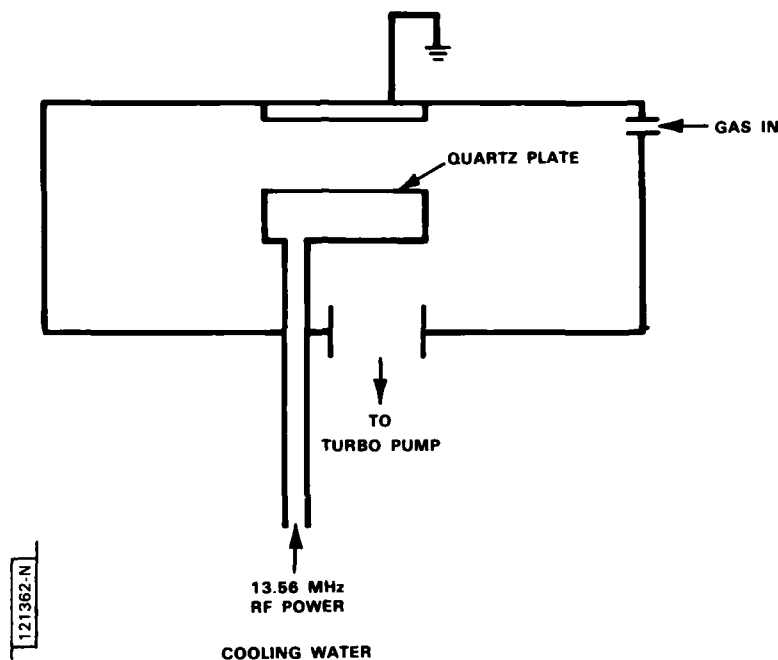


Fig. 4-3. Schematic of RIE chamber. Gas inlet on right leads to asymmetries in Figs. 4-4 and 4-5.

backfilled to a pressure of 10^{-2} Torr for both SF_6 and Ar etching. All samples are placed on a fused quartz plate on the bottom electrode. Power density during these experiments was varied from 0.32 W/cm^2 to 0.63 W/cm^2 , with a dc bias voltage variation from 100 V to 300 V.

For etch rate measurements and profile studies, n-type GaAs substrates were used. Three thousand Å Au films and 1000 Å Ni films for a mask were sequentially evaporated on the samples, and the Ni was then patterned by standard photolithographic and wet etching techniques. Etch-depth measurements were made with a diamond stylus profilometer. Both optical and scanning electron microscopy were used to look at the etched surface textures and the wall profiles.

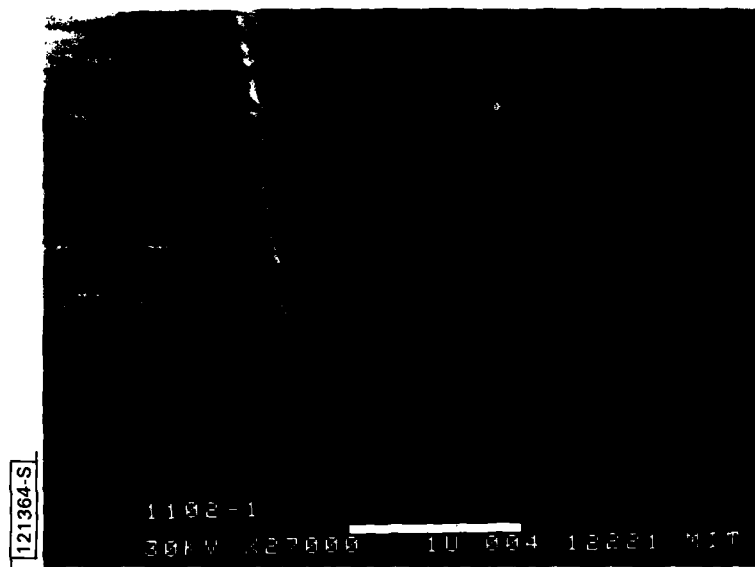
The samples used for damage studies consisted of 5000 Å of VPE, n-type GaAs grown upon an n^+ substrate. After etching the n-GaAs with SF_6 or Ar, an ohmic contact was applied to the back of the n^+ substrate, and a 12-mil-diameter Ti-Au Schottky barrier diode was fabricated on the damaged n-GaAs

layer. Current-voltage measurements were made on samples etched at various power levels, as well as on control samples that had not been etched.

Sulfur hexafluoride etches Au at low bias voltages and low power levels, giving straight walls with no undercut and smooth etched surfaces. Nickel etches slowly ($\sim 30 \text{ \AA/min}$) and works well as a masking material. Figures 4-4(a) and 4-4(b) show $1\text{-}\mu\text{m}$ -wide gaps etched in Au at different power densities. The left wall in both figures is slightly sloped, which is an artifact of our system caused by the positioning of the gas inlet. The etched surface is smooth and clean. Figure 4-5 shows a $1\text{-}\mu\text{m}$ -wide gap in Au that was sputter-etched in Ar. The profile is the same as the SF_6 -etched profile, including the sloped left wall. The Ar sample, however, has bumps distributed all over the etched surface.

In Fig. 4-6 the etch rates of Au and GaAs as a function of dc bias voltage for both SF_6 and Ar are plotted. Both Au and GaAs are removed at higher rates by SF_6 , and much lower bias voltages can be used to achieve the desired rates and profiles when using SF_6 as opposed to Ar. We also found that the etch rates in Ar vary significantly with feature size: large geometries etch much more slowly than small features. Sulfur hexafluoride etched more uniformly across a sample, regardless of geometry.

Figure 4-7 shows a small gap etched in GaAs with SF_6 . The etched surface is smooth and the profile good. Figure 4-8 shows a second GaAs sample etched in Ar. Here the GaAs surface is very rough and there is a slight build-up at the base of the etched walls. While the SF_6 -etched GaAs has a better appearance than the surface etched in Ar, it is important to determine the relative levels of damage introduced by the two etching gases. The ideality factor n of the forward-biased Schottky barrier diode characteristic gives a qualitative measure of the etching damage. An unetched and a SF_6 -etched GaAs surface both have $n \sim 1.09$, indicating that the amount of damage being done to the GaAs by the SF_6 is small. In contrast, GaAs surfaces etched in Ar have $n \sim 1.5$.



(a) 0.32 W/cm² POWER DENSITY



(b) 0.47 W/cm² POWER DENSITY

Fig. 4-4. 1- μ m-wide gaps etched in 3000- \AA -thick Au film using SF_6 gas at 0.32 W/cm² and 0.47 W/cm² power densities. Sloped left wall is due to positioning of gas inlet in RIE system (see Fig. 4-3).

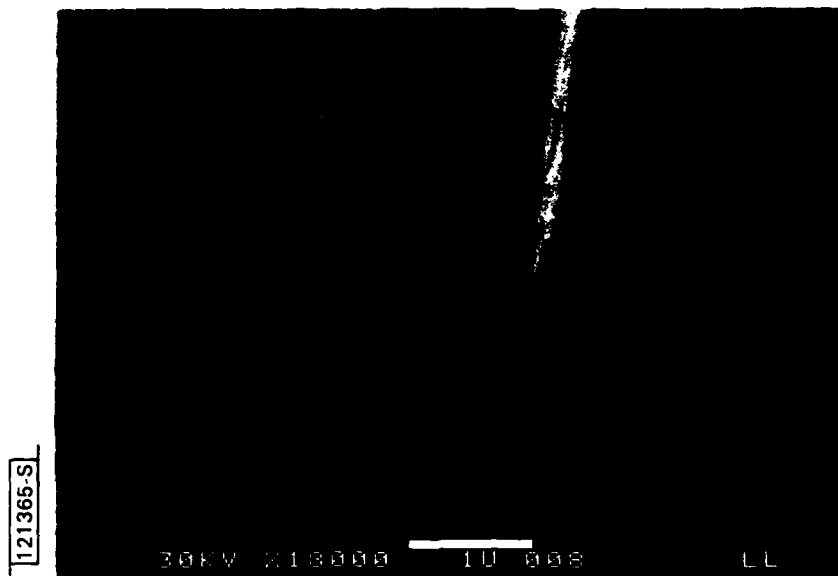


Fig. 4-5. 1- μ m-wide gap etched in 3000-Å-thick Au film using Ar gas at 0.47 W/cm² power density. Sloped left wall is due to positioning of gas inlet in RIE system.

This ability to etch GaAs with minimal damage to the etched surface allows multistep processing with SF₆ in GaAs device application. Our particular application is the GaAs, self-aligned FET where the 1- μ m-wide gap between source and drain defines the gate length. Therefore, precise reproduction of the gap is necessary. Also, because many cells are connected in a device, a uniform etching process is important.

The fabrication steps are shown in Fig. 4-9. The Au layer is etched by use of a Ni mask. The SF₆ then etches quickly through the Ge layer (>1000 Å/min). When the second Ni layer is reached, it may be removed with a standard wet etch. We have found, however, that SF₆ can be used to continue through the thin Ni layer down into the GaAs, without any of the surface roughening that is typically seen when going from a slowly etching material to a faster etching one. Slight undercut of the Ge occurs while the Ni layer is being removed. With the source and drain defined by the SF₆ etching, the gate may then be evaporated into the gap.

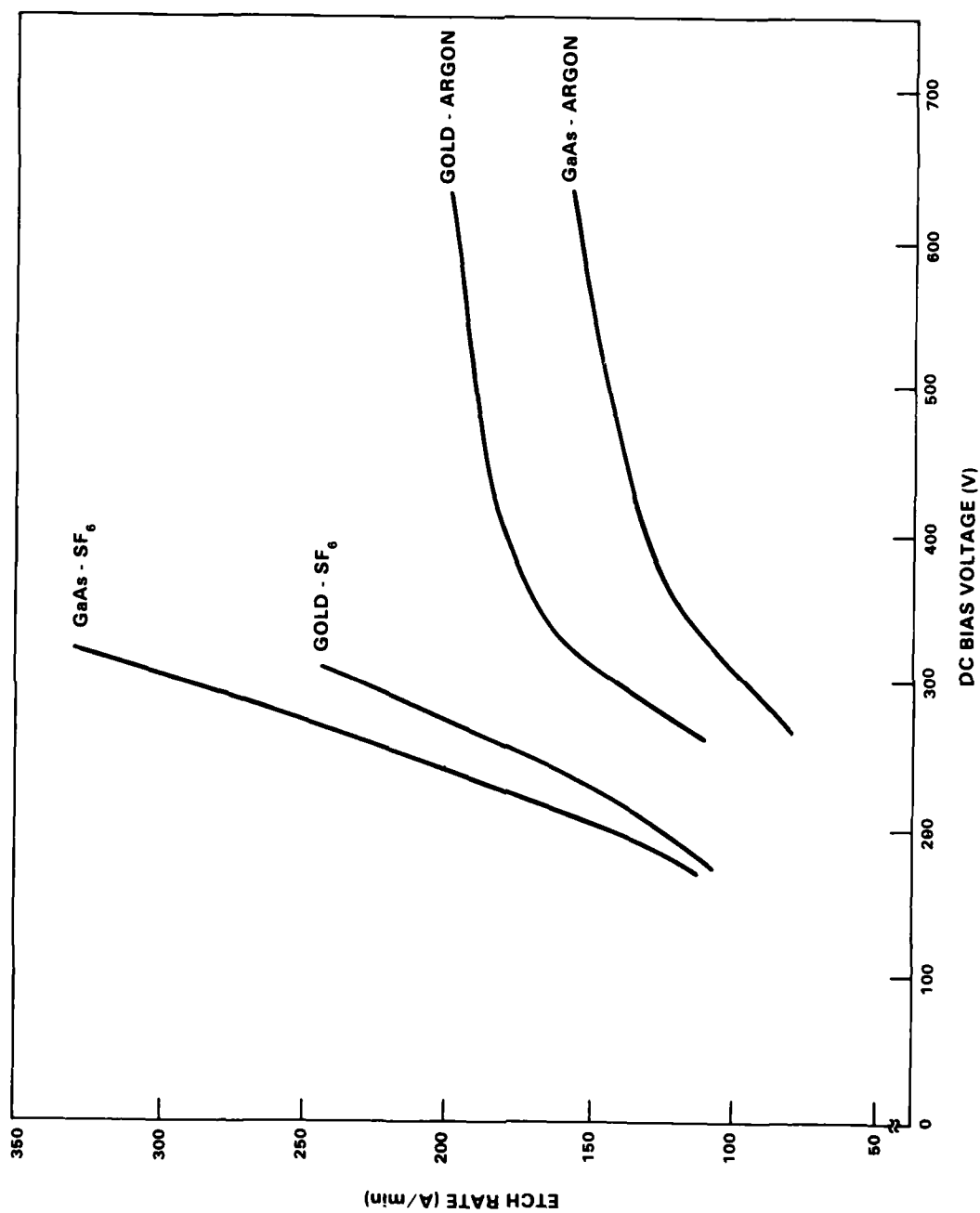


Fig. 4-6. Au and GaAs etch rates as a function of dc bias voltage for etching with both SF_6 and Ar.

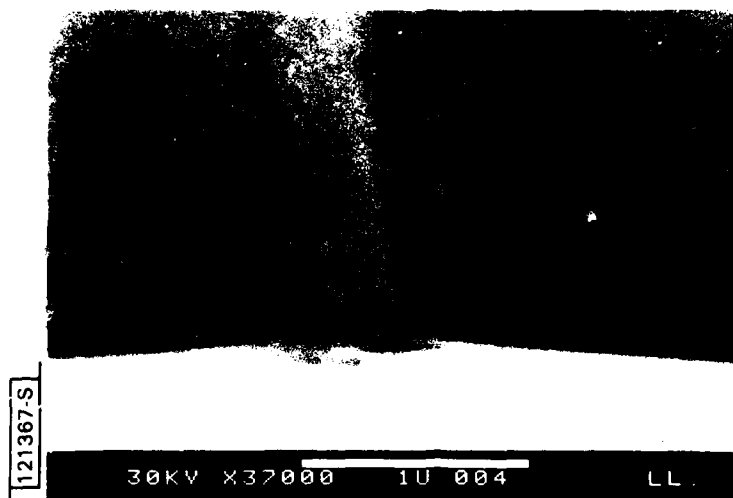


Fig. 4-7. Submicrometer gap etched in GaAs with SF_6 at 0.47 W/cm^2 power density.



Fig. 4-8. Submicrometer gap etched in GaAs with Ar at 0.47 W/cm^2 power density.

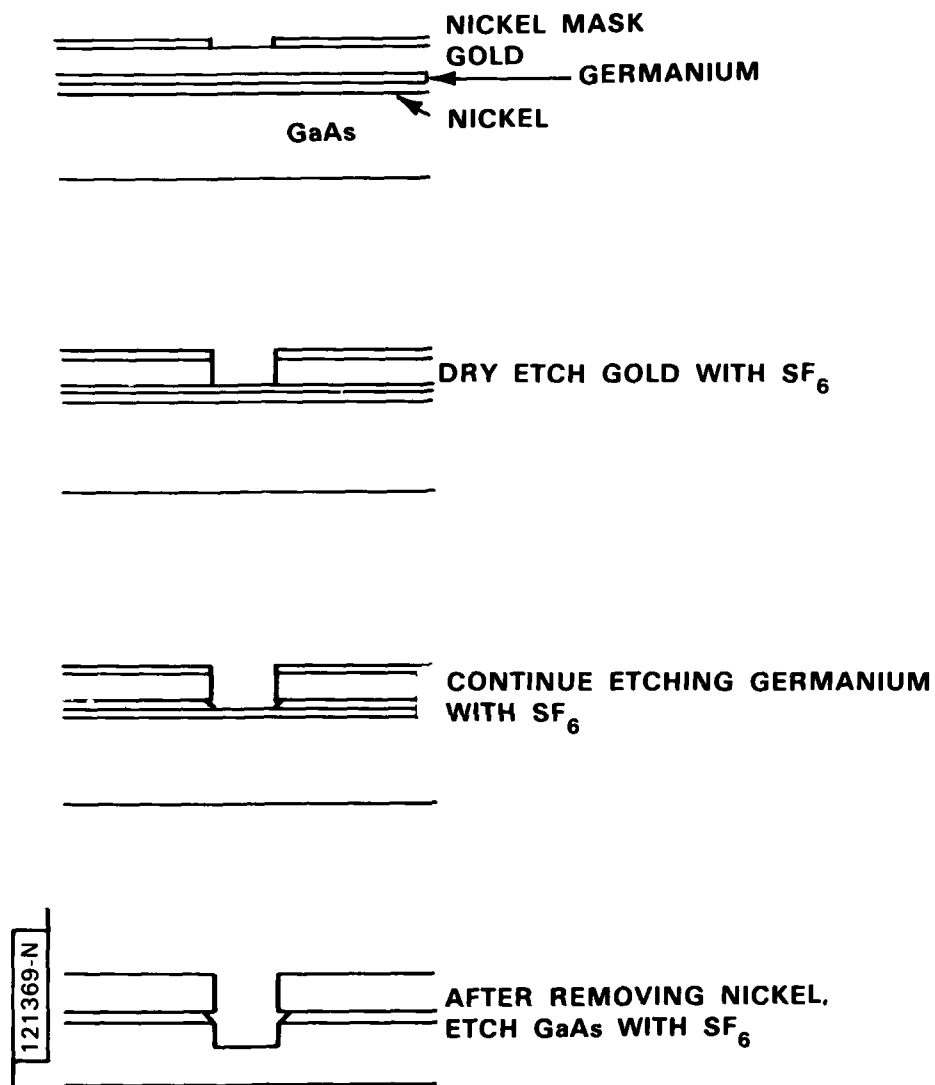


Fig. 4-9. Steps for fabricating gate recess of self-aligned GaAs FET.

The mechanisms involved in the SF_6 etching of Au are not clear. No stable, volatile gold fluorides have ever been observed. It may be possible, however, that some unstable, short-lived volatile gold fluoride does exist. But even if the process is a sputtering process, the higher etch rates at low voltage levels, smooth and clean structures, uniformity of etch, and minimal damage make SF_6 etching a viable alternative to Ar sputter etching.

S.M. Cabral
M.E. Elta
A. Chu
L.J. Mahoney

References

1. Solid State Research Report, Lincoln Laboratory, M.I.T. (1981:3) pp.45-49, DTIC AD-A112696.
2. Solid State Research Report, Lincoln Laboratory, M.I.T. (1982:2).
3. P. Rai-Choudhury, J. Electrochem. Soc. 118, 266 (1971).
4. R. d'Agostino and D. Flamm, J. Appl. Phys. 52, 162 (1981).
5. J. Randall and J. Wolfe, Appl. Phys. Lett. 39, 742 (1981).

5. ANALOG DEVICE TECHNOLOGY

5.1 MNOS Nonvolatile Analog Memory

MNOS devices have been developed for the nonvolatile storage of sampled analog data. Data obtained from discrete MNOS capacitors⁽¹⁾ and the results of a theoretical model of the tunneling process have been presented previously.⁽²⁾ Nonvolatile storage of analog signals was later demonstrated in an integrated 32-sample MNOS/CCD.⁽³⁾ The speed, erase/write (E/W) endurance, fixed-pattern noise, and binary/analog memory correlation performance of this device were subsequently documented.⁽⁴⁾ In this report we supplement earlier discussions of device linearity and signal retention after extensive E/W cycling. We also document the performance of a 256-sample MNOS/CCD analog memory.

5.1.1 32-Sample MNOS/CCD

Figure 5-1 shows the output of a 32-sample MNOS/CCD after storage of a ramp input. The output was acquired and stored digitally; a least-squares fit of a ramp to this output, which spans 5 V, has an RMS deviation of 28 mV. This is indicative of the fixed-pattern noise of the device and implies a linear dynamic range of 39 dB for short-term memory.

Typical retention data of the 32-sample memory are shown in Fig. 5-2. Ten neighboring cells in a device were written such that their initial output levels covered the 5-V range. The output levels, relative to that of one cell which is used as a reference, are plotted vs the logarithm of the storage time. The data in Fig. 5-2(a) were obtained from a device which had undergone 10^5 E/W cycles and are essentially identical to the results obtained from an uncycled device. The decay of the full memory window (defined as the difference between the maximum and minimum output levels) is initially 180 mV/decade or, normalized to the initial window of 4.9 V, 37 mV/dec V. In fact, the decay rate of a given cell is proportional to the initial value of the stored signal sample, a result elucidated previously

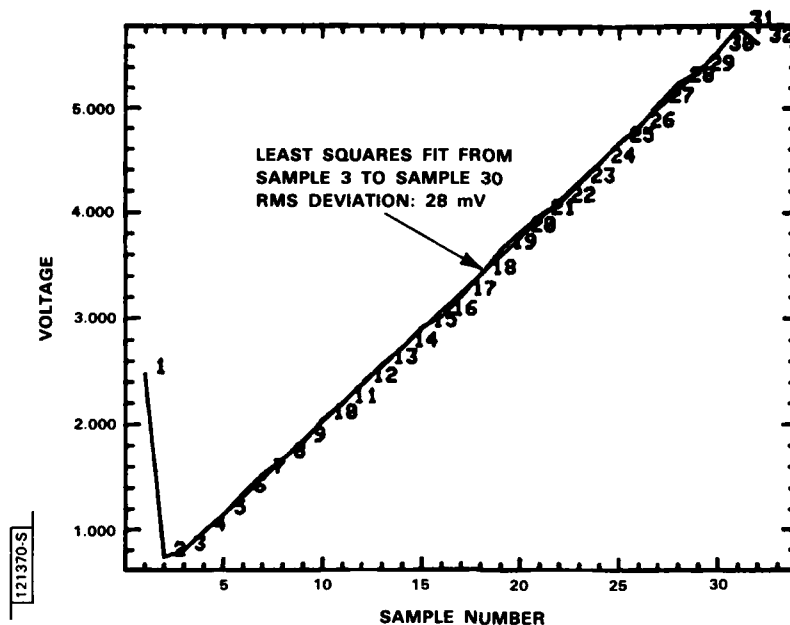


Fig. 5-1. Output of analog memory after storage of a ramp.

with respect to discrete devices,⁽⁵⁾ and which has the fortunate consequence that stored signals are attenuated in time but do not become distorted. We had previously demonstrated a dynamic range of 33 dB after 100 hours of storage.⁽³⁾

After 10^3 to 10^4 seconds of storage, the decay rate increases significantly. As this is also the turn-around point of the reference cell in this device [i.e., $d(V_T)/d(\log t)$ becomes positive], we believe that the rate of loss of stored holes at this point exceeds that of stored electrons.

The device was subjected to 10^7 E/W cycles and the retention test repeated [Fig. 5-2(b)]. The decay rate has increased significantly, especially at the later times. We conservatively estimated 10^6 cycles as the limit for these devices as analog memories.

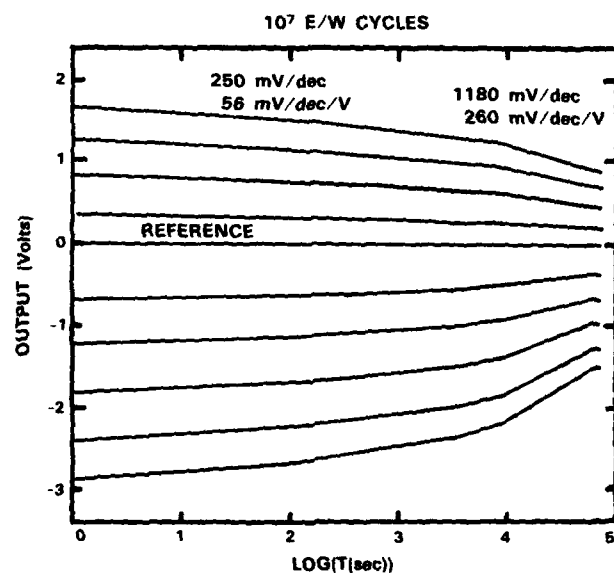
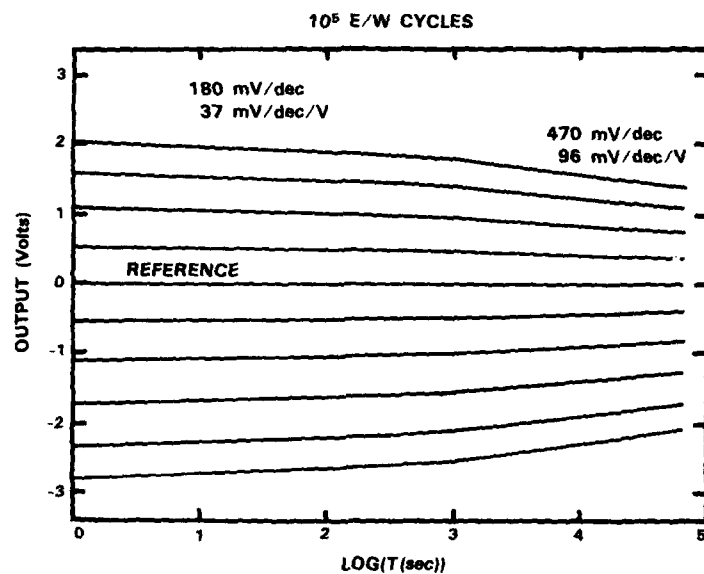


Fig. 5-2. Retention of signal charge in 32-sample MNOS/CCD.

5.1.2 256-Sample MNOS/CCD

The 32-sample MNOS/CCD was extended to a 256-sample device using a conservative design approach. Qualitatively, the unit cell structure was preserved, both in the plan and in the cross-sectional views. Design parameters have been given previously.⁽⁴⁾ The device has been designed, fabricated, and tested.

Figure 5-3 is a photograph of the output circuit and the last few stages of the device. By utilizing a three-phase CCD and reducing the gate length to 10 μm , the stage length was reduced to 30 μm , half that of the previous device. This also increased the projected clock speed to a value of 2 MHz. The CCD gate width is 60 μm , and the total stage width (CCD clock lines and wells, memory site, and readout structure) is 200 μm . The MNOS site is 10 $\mu\text{m} \times 10 \mu\text{m}$, preserving the 6:1 CCD:MNOS area ratio of the 32-sample device.

Three-layer clock electrodes, one aluminum and two polysilicon layers, are used, one layer for each clock phase. Two-layer clock electrodes are possible but would require that the gate electrodes of the CCD wells adjacent to the MNOS sites alternate from stage to stage; this would invite fixed-pattern noise from the threshold-voltage differences.

Aluminum overlays on the clock lines and parallel holding well, which was combined with the adjacent transfer gate and formed of polysilicon, were used so that the only long run of polysilicon is the transfer gate between the CCD phase 1 well and the memory sites. The parallel holding well may be accessed electrically either directly or by means of reset and source-follower transistors. This permits the correlation operation as described for the 32-sample device.⁽⁴⁾

The same n-channel process as used for the 32-sample device was employed, with the addition of the second polysilicon level deposition, doping, definition, and oxidation. The first run of these devices was lost in an attempt to plasma etch the aluminum. Because of radiation damage, the MNOS areas exhibited flatband voltages more negative than -40 V and could not be written. The final hydrogen anneal normally used in this process did not

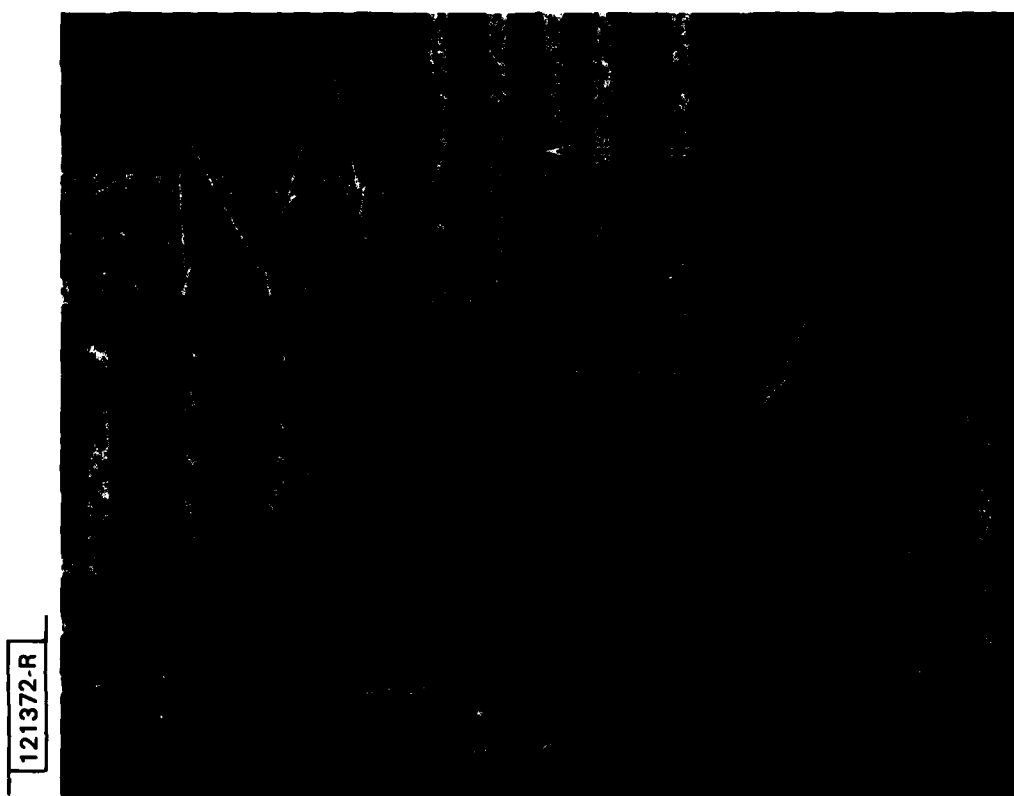


Fig. 5-3. Output circuit and several CCD/MNOS stages of 256-sample analog memory.

remove the MNOS damage, although it did cause the CCD channel areas to return to a flatband voltage of -1 V. The inability of the hydrogen to anneal the plasma-generated radiation damage in the MNOS areas is caused by its inability to diffuse through silicon nitride.⁽⁶⁾ The second run of devices was damaged by plasma clean-up of photoresist after the high-temperature hydrogen anneal. In this case the exposure to ionizing radiation was less; the high-temperature anneal was repeated, and some functional devices were obtained.

The output of one device from the second run, subsequent to the storage of eight cycles of a triangular wave, is shown in Fig. 5-4. The device was erased for several milliseconds at -23 V; writing was accomplished with a +32-V, 140- μ s pulse. The 400-mV tilt of this output is an indication of variations in threshold voltage along the length of this device. Proper processing should result in significantly improved performance.

5.1.3 Summary and Discussion

Nonvolatile storage of sampled analog signals in 32- and 256-sample charge-transfer devices has been demonstrated. The MNOS memory sites are compatible with the n-channel CCD process, requiring one additional mask step. A linear dynamic range of 33 dB is readily achievable, giving the equivalent of 5 to 6 bits of binary storage to each analog storage cell. Stored signals are retained for several days with some loss of amplitude but negligible distortion. The maximum input and output sampling rates are limited by the CCD (not the MNOS storage) to a few megahertz in the present devices but may be increased to a few tens of megahertz by the use of buried-channel techniques. (Because the MNOS storage is an inherently surface-channel phenomenon, this would require a surface-to-buried-channel transition at each memory site.) Bandwidth may be extended to a few hundred megahertz by hybridization with surface-acoustic-wave devices.

The E/W voltages of both the MNOS and floating gate devices (≈ 30 V) are higher than conventional linear device supply levels. However, the required current in the analog memories is low, the loads being capacitive, and the current could be generated by on-chip voltage multipliers.

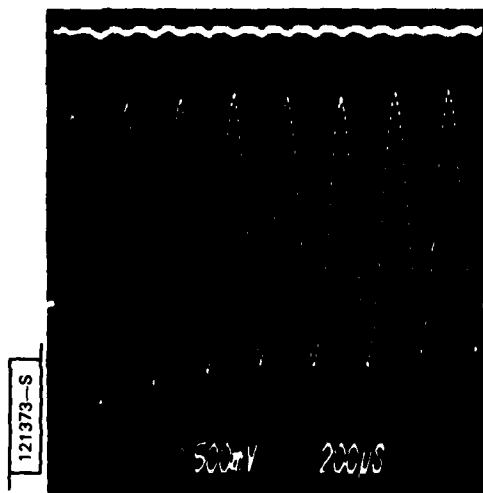


Fig. 5-4. Output of 256-sample MNOS/CCD after storage of eight cycles of a triangular wave. Write: 32 V, 140 μ s; erase: -23 V; clock rate: 167 kHz.

Further investigation into several aspects of device behavior is needed. For example, it has been observed that the written threshold levels in the integrated devices largely depend on the write voltage level on the gate, more so than in the discrete MNOS capacitors. Avalanche generation or multiplication in the regions where the transfer gate meets the memory gate and where the tunnel oxide meets the p^+ -diffused channel stop are suspected. Careful modeling of the electric field strength in the substrate is needed to verify this and to guide attempts to design around it.

Sources of and possible cures for fixed-pattern noise should be identified. Variations in the device structure (doping, dielectric thickness, nitride trap density and levels) undoubtedly play a role. It is possible that hot-carrier generation may cause charge trapping in nonmemory dielectric areas, such as below the transfer gate, thereby shifting the threshold voltage and producing fixed-pattern noise. Investigations of MNOS charge trapping and decay mechanisms, in particular how they impact analog device design and performance, would also be valuable.

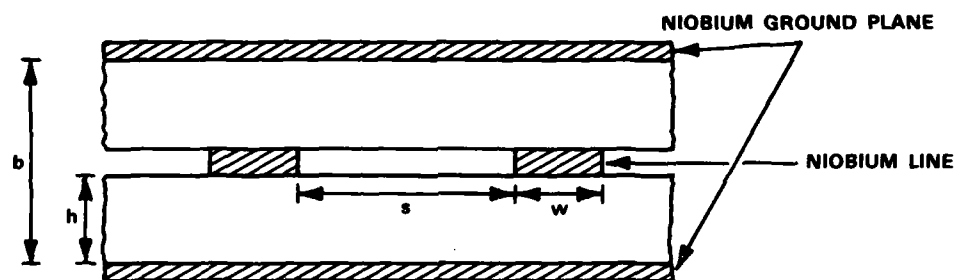
Nonvolatile analog memory is most useful not for bulk storage, but in integrated circuits where the overall size, power consumption, and weight must be minimized and/or the architecture limits the on-chip storage area. For example, in a storage correlator it may be necessary to store an analog tap weight at each cell but within a cell pitch insufficient for A/D conversion and several bits of binary storage. Analog memory could also be used in imaging arrays for background cancellation and image correlation.

R.S. Withers
D.J. Silversmith
R.W. Mountain
R.W. Ralston

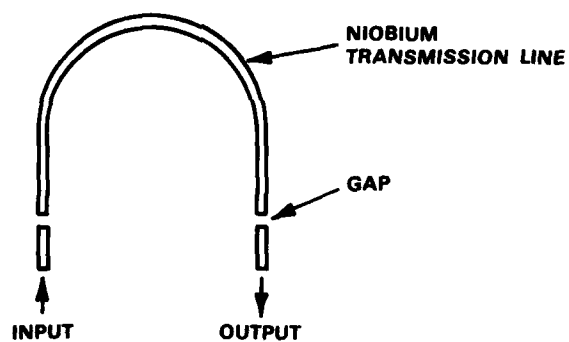
5.2 Low Loss Substrates for Superconductive Circuits

Superconductive transmission lines can provide the essential delay element for extremely wide band (to 10 GHz) analog signal-processing devices.⁽⁷⁾ Long superconductive lines are fabricated on thin substrates and packaged in a stripline configuration [see Fig. 5-5(a)]. Superconductivity provides very low conductor losses, but low-loss electromagnetic delays can only be realized when the dielectric substrates have equally low losses.

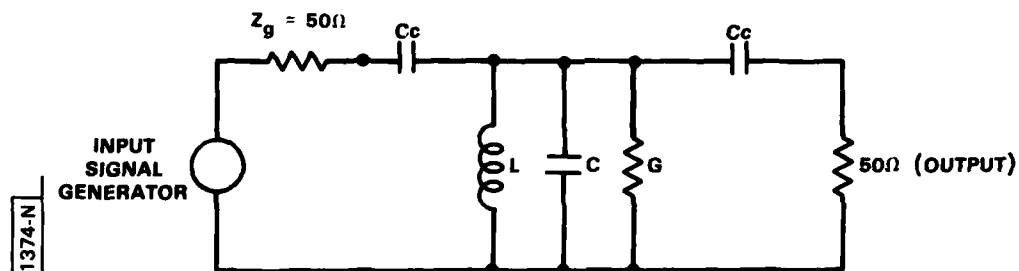
In device design, the ratio of conductor width w to total substrate height b ($\approx 2h$) is chosen to provide a characteristic transmission line impedance of 50Ω , which implies $w/b \approx 0.2$ for substrates with a relative dielectric constant of about 10. Adequate electromagnetic isolation between adjacent lines is ensured by choosing the line spacing s so that $s > 2b$. Hence, to achieve adequate delays on reasonably small substrate areas, long (10-100 m), narrow ($w = 10-100 \mu\text{m}$) lines must be fabricated on thin ($h = 10-100 \mu\text{m}$) substrates. These long, narrow lines and thin substrates, however, burden the designer of superconductive microwave circuits with unusual requirements for substrate materials. Many of the materials commonly used for room temperature microwave devices are no longer adequate if the low losses associated with superconductors are to be fully exploited. Surface voids and defects are unavoidable in polished polycrystalline oxides such as



(a) CROSS SECTION OF SUPERCONDUCTIVE STRIPLINE



(b) TOP VIEW



(c) EQUIVALENT CIRCUIT

Fig. 5-5. Niobium stripline resonator.

alumina and beryllia. Together with the light scattering in these substrates, these imperfections render the photolithography and etching of narrow lines very difficult. Also, because the lines are very long, problems with dispersion and anisotropy of the dielectric are much more severe with superconductive microwave circuits.

Although resonator measurements of niobium on sapphire in a stripline configuration indicate very low conductor and substrate losses, the anisotropy of this substrate will limit its use in certain applications. For example, in backward-coupled lines the anisotropy introduces an unwanted forward coupling, limiting directivity to 13 dB. Time-bandwidth products of tapped-delay-line filters using backward-wave couplers as the tapping elements⁽⁷⁾ are consequently limited to values of several hundred.

The high temperature necessary for depositing most of the superconductive metals excludes the use of most polymer substrates, such as Teflon. Among many evaluated materials, silicon was found to satisfy all of the requirements for superconductive microwave circuit substrates: high dielectric constant, low loss, isotropy, ruggedness, and ready availability.

Even though the use of very high resistivity silicon as a microwave circuit substrate has been reported,⁽⁸⁾ its use at room temperature is very limited because of the difficulty in maintaining its insulating properties during processing. At the low temperatures necessary for superconductive circuits, however, silicon is a much better insulator.

There is little published data about dielectric losses of silicon at low temperatures. Two mechanisms of loss can be identified. The first is loss associated with electrons excited to the conduction band. A simple calculation shows that for the 200 Ω -cm phosphorus-doped silicon, a loss tangent ($\tan \delta$) $\ll 10^{-6}$ can be obtained for temperatures below 10 K. The other mechanism that can induce losses in silicon is the hopping of electrons between localized states associated with donors or acceptors. It is very difficult to calculate the effect of this mechanism since a well-developed theory is not available. We have, however, extrapolated the results of measurements made by Pollak and Geballe⁽⁹⁾ on silicon. Dissipation factors of less than 10^{-6} below 10 K are obtained as a result of this extrapolation.

To evaluate the use of silicon as a substrate for superconductive circuits, a series of resonator experiments is being conducted. A resonator consisting of a 17-cm-long by 42- μm -wide niobium stripline with two 50- μm gaps on 200- μm -thick silicon (total thickness 400 μm) was used [Fig. 5-5(b)]. The transmission through such a structure is measured in the range of 200 MHz to 10 GHz. A series of peaks corresponding to different resonant modes is observed. The quality factor Q_m of each mode is a measure of electromagnetic losses. The manner in which multiple losses reduce Q_m is expressed by

$$Q_m^{-1} = Q_c^{-1} + Q_d^{-1} + Q_L^{-1}$$

where Q_c is the quality factor associated with conductor loss, Q_d is associated with the dielectric loss, and Q_L is determined by the loading of external or measurement circuitry. The gaps were chosen to minimize the loading, i.e., $Q_L \gg Q_m$.

The equivalent circuit shown in Fig. 5-5(c) represents the resonator. The insertion loss of the resonator at each resonant peak is

$$\frac{2}{2 + Q_L^2 Z_g G}$$

where G is the equivalent parallel conductance of the resonator, given by

$$G = \frac{\alpha_t \ell}{Z_o} + \frac{n\pi}{Z_o} \tan \delta$$

and where

- ℓ is the length of the resonator
- Z_o is the characteristic impedance of the stripline used in the resonator
- α_t is the attenuation associated with losses in the niobium
- n is the mode order = $\frac{2\ell f_n}{v_{ph}}$

AD A124 305

SOLID STATE RESEARCH(U) MASSACHUSETTS INST OF TECH
LEXINGTON LINCOLN LAB A L MCWHORTER 22 NOV 82 1987-3
ESD-TR-82-086 F19828-80-C-0002

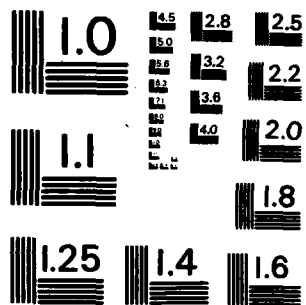
22

UNCLASSIFIED

F/G 20/12

NL

END
DATE
FILMED
3 83



MICROCOPY RESOLUTION TEST CHART
NATIONAL BUREAU OF STANDARDS-1963-A

Q_L is $\frac{1}{\omega C_c Z_g}$
 Z_g is the impedance of the generator and measuring equipment (50 Ω)
 C_c is the gap (coupling) capacitance
 f_n is the frequency of n^{th} order resonance
 v_{ph} is the phase velocity $c/\sqrt{\epsilon_r}$

The condition for low external loading of the resonant circuit is

$$2 \ll Q_L^2 Z_g G$$

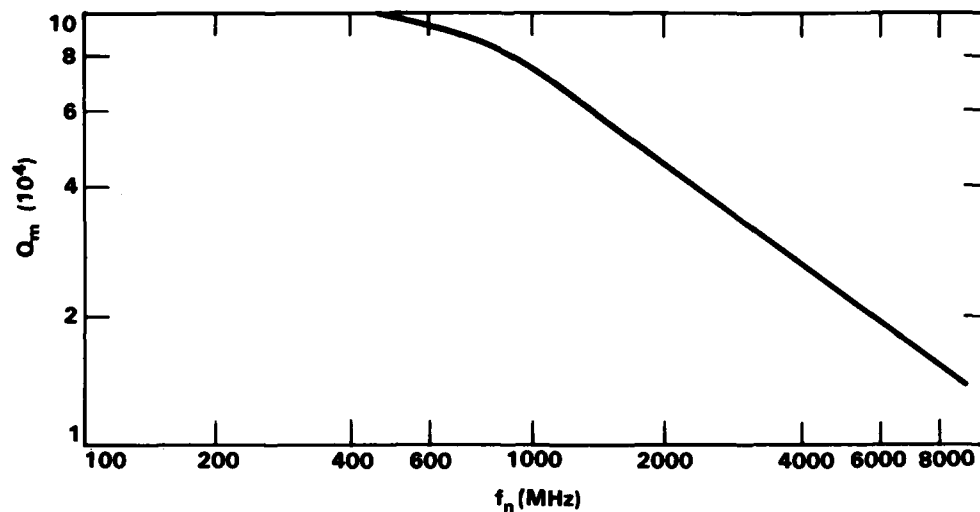
Thus insertion losses at resonance larger than 20 dB are an indication that the resonator is not being loaded appreciably.

The results of the measurements are shown in Fig. 5-6. It is seen in Fig. 5-6(a) that $Q_m > 10^4$ can be obtained at frequencies to 10 GHz using our current technology. The slope of the quality factor with frequency ($Q_m \propto \omega^{-0.74}$) is a strong indication that the losses are associated with the niobium and not with the silicon. Below 600 MHz, Q_m is constant. At these frequencies the dielectric losses appear to dominate, and the measured value of $Q_m = 10^5$ indicates a substrate loss tangent $< 10^{-5}$.

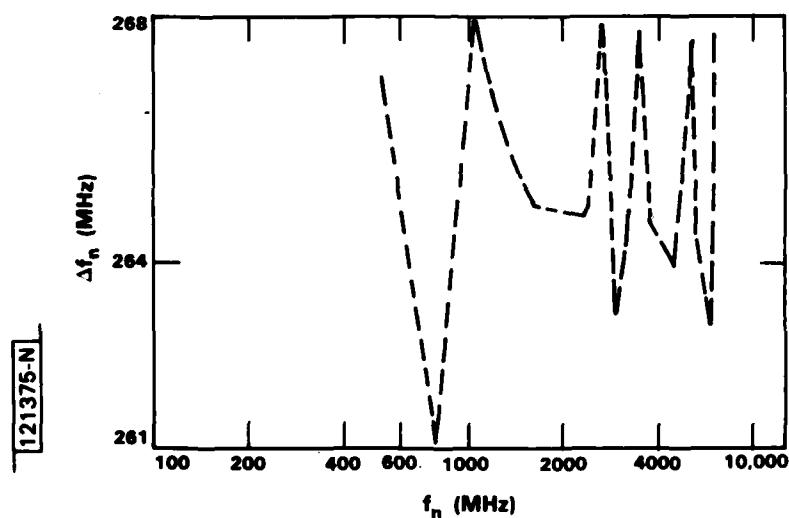
The scatter in the dispersion results of Fig. 5-6(b) is probably due to internal reflections in the resonator caused by variation in the line width known to exist in the resonator measured. The lack of a non-oscillatory dependence of the apparent phase velocity with frequency indicates a dispersionless dielectric.

The use of silicon as a substrate will permit the use of the technology developed for solar cells and imaging devices for the chemical and electrochemical machining of the substrates. Furthermore, it offers the possibility of integrating silicon devices with superconductive circuits in the development of a new class of programmable filters.

A.C. Anderson
 R.S. Withers
 S.A. Reible



(a) PLOT OF MEASURED Q_m AS A FUNCTION OF FREQUENCY



(b) PLOT OF FREQUENCY INTERVAL Δf_n BETWEEN ADJACENT RESONANCE MODES AS FUNCTION OF FREQUENCY

Fig. 5-6. Measurements of resonator.

5.3 Considerations for an Integrated Optical Spectrum Analyzer (IOSA)

Several major problems of current IOSA designs were discussed previously.^(10,11) The limited performance achieved to date with such devices cannot be attributed to a single design area. Each component in existing IOSAs, i.e., the input lens, Bragg cell, output lens, and detector array, must be improved if better performance is to be achieved. The prospects for significantly improving the performance of all these elements in existing configurations do not appear good. This leads us to consider whether alternative configurations might be possible which would permit the fabrication of higher performance devices. In this report we consider each of the four elements of an IOSA, propose an optimum structure for each element, and suggest an integrated configuration. This configuration of optimum elements is shown in Fig. 5-7.

We begin by considering the input and output lenses. The input lens is simply a beam expander and thus need only have a narrow angular field of view. However, as previously discussed, it is desirable to amplitude weight the aperture to improve the frequency resolution of the analyzer.⁽¹⁰⁾ A constant-period oblique-incidence grating lens appears to be an ideal choice. The grating lends itself to amplitude weighting and, because of the oblique incidence, has the additional advantage that no direct laser light can enter the detector array to degrade the dynamic range. The output lens does not need to be amplitude weighted but must have a sufficiently wide field of view. A Fresnel lens appears to be a good choice. Such a lens has already been demonstrated on a glass waveguide with extremely low insertion loss (0.7 dB) and an angular field of view of 0.1 radian.⁽¹²⁾ The performance of Fresnel lenses on Ti-diffused LiNbO_3 waveguides, which are typically used in IOSAs, has not been good.⁽¹²⁾ It is thus preferable that both the input and output lenses be fabricated on glass waveguides. Two additional advantages of glass waveguides over Ti-diffused LiNbO_3 waveguides are significantly lower optical propagation loss and the likelihood that the detector array can be integrated into a glass waveguide on passivated Si.

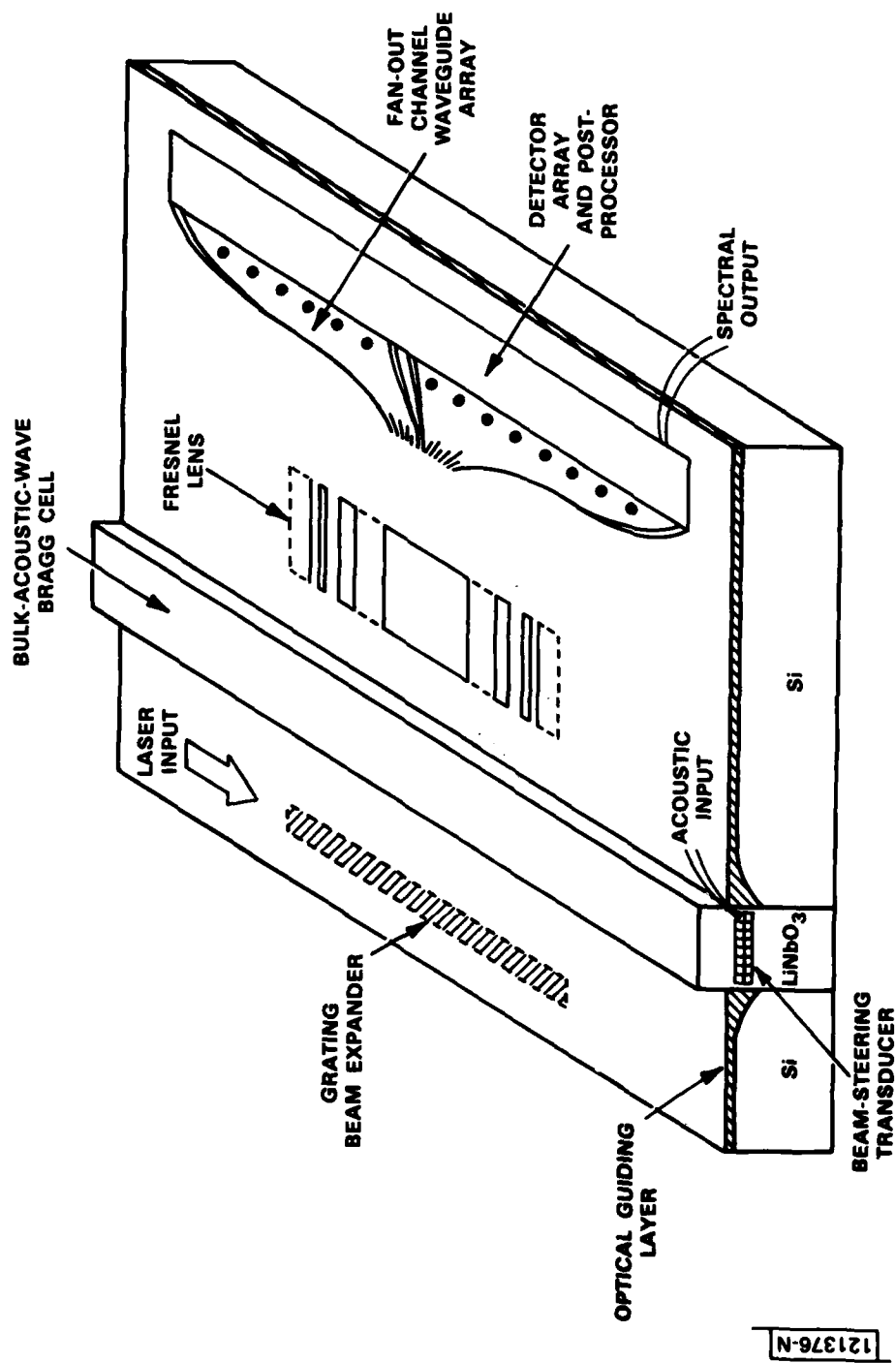


Fig. 5-7. Proposed IOSA configuration.

The typical loss of a Ti-diffused LiNbO_3 waveguide is around 0.6 dB/cm,⁽¹³⁾ limiting the maximum achievable dynamic range to ≈ 32 dB⁽¹⁴⁾ because of waveguide scattering into the detector array. Propagation losses as low as 0.01 dB/cm have been reported for laser-annealed glass waveguides.⁽¹⁵⁾ Use of such guides would raise the limit on the dynamic range to ≈ 52 dB.⁽¹⁴⁾

We now consider the detector array. As suggested above, an integrated detector array on Si is desirable. Details of such a waveguide/detector array have been discussed by Boyd and Chen.⁽¹⁶⁾ To reduce the size of an IOSA, a waveguide fan-out array⁽¹⁷⁾ could be used to feed the densely spaced optical frequency channels to a detector array of convenient pitch. Design constraints for the lenses and the pitch of the detector elements were addressed in earlier reports.^(10,11) "On-chip" post-detection processing may also be incorporated into the structure. The readout speed of existing detector arrays is not compatible with the time-bandwidth products being considered. On-chip post-detection processing can be used to eliminate the need for a high output-data rate.

The signal to be analyzed is admitted through the acoustic port, and as wide a bandwidth as possible is desired. Above 1 GHz both propagation loss and dispersion become a problem in surface-acoustic-wave (SAW) devices.⁽¹⁸⁾ In addition, transducer fabrication becomes extremely difficult. However, bulk-acoustic-wave (BAW) transducers can be fabricated for operation at very high frequencies (up to 18 GHz),⁽¹⁹⁾ and BAWs can have an order of magnitude lower propagation loss⁽²⁰⁾ with no significant dispersion. For these reasons it is preferable to use BAWs, rather than SAWs, in a high-frequency Bragg cell. For high diffraction efficiency and octave-bandwidth operation, we earlier proposed using a phased-array to achieve broad-band phase matching.⁽¹¹⁾ Previous beam-steered phased-arrays have always employed a successive phase shift between elements of $n \times 180^\circ$, where n is an integer.⁽²¹⁾ With such a feed the array pattern is symmetric about the normal to the array. So that most of the acoustic energy is radiated in the desired direction, the individual array elements must be tilted in a staircase manner, as shown in Fig. 5-8(a). This necessitates fabricating small steps on the edge of the crystal, a process that becomes increasingly

impractical at high frequencies. However, the array factor of a quadrature-fed array is not symmetric about the normal to the array [Fig. 5-8(b)]. This permits a planar array to be used. The majority of acoustic power is radiated only along the direction of the array maximum that is closest to the normal. Because the edge of the crystal does not need to be stepped, it should be possible to fabricate such a quadrature-fed planar beam-steering array at much higher frequencies than was previously possible.

Figure 5-7 represents one possible integrated configuration for an IOSA containing the desired components. The optical energy is confined to low-loss glass waveguides on passivated Si, except in the Bragg cell. The optical beam in the Bragg cell (a crystal such as LiNbO_3) is diffracted by a BAW launched with a quadrature-fed phased-array transducer. Post-detection processing is included on the device. An item still under study is the

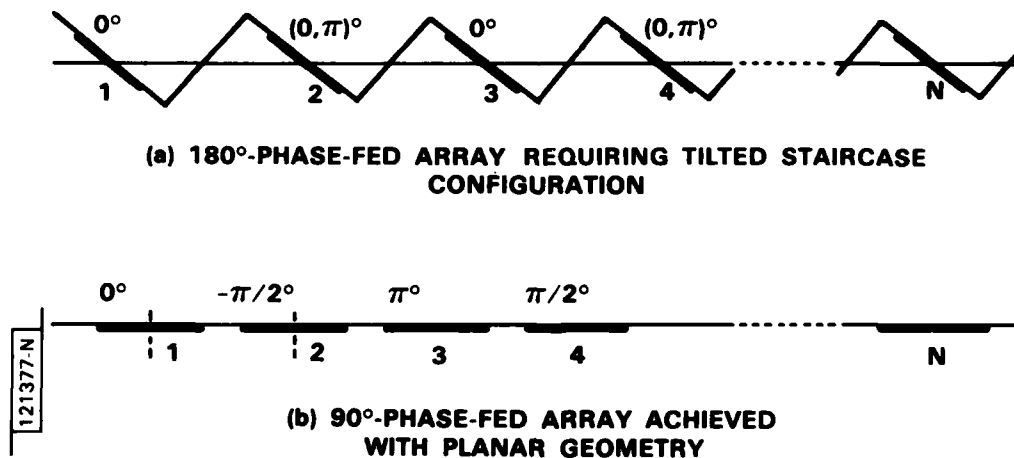


Fig. 5-8. Beam-steered transducer arrays.

mismatch in the heights of the optical and acoustic beams. A method for confining the BAW is highly desirable, as it would ensure efficient overlap of the optical and acoustic beams through the length of the Bragg cell.

P.V. Wright
D.E. Oates

References

1. Solid State Research Report, Lincoln Laboratory, M.I.T. (1972:2), p. 70, DDC AD-A07867614.
2. Solid State Research Report, Lincoln Laboratory, M.I.T. (1980:3), p. 49, DTIC AD-A094075.
3. Solid State Research Report, Lincoln Laboratory, M.I.T. (1981:1), p. 53, DTIC AD-A103887/6.
4. Solid State Research Report, Lincoln Laboratory, M.I.T. (1981:2), p. 55, DTIC AD-A110947.
5. R.S. Withers, R.W. Ralston, and E. Stern, IEEE Electron Device Lett. EDL-1, 42 (1980).
6. G. Schols, H. Maes, G. Declerck, R. Van Overstraeten, Rev. de Physique Appliquee 13, 825 (1978); H. Maes and G. Heyns, J. Appl. Phys. 51, 2706 (1980).
7. Solid State Research Report, Lincoln Laboratory, M.I.T. (1982:2).
8. M. Caulton in Topics in Solid State and Quantum Electronics, edited by W.D. Herschberger (John Wiley, New York, 1972), p. 420.
9. M. Pollak and T.H. Geballe, Phys. Rev. 122, 1742 (1961).
10. Solid State Research Report, Lincoln Laboratory, M.I.T. (1981:3), p. 63, DTIC AD-A112696.
11. Solid State Research Report, Lincoln Laboratory, M.I.T. (1982:1), p. 87, DTIC AD-A118847.
12. W.S.C. Chang, S. Fourouhiov and J.H. Delavause, Interim Scientific Report, AFOSR grant no. 80-0037, (1981).

13. D. Mergerian, E.C. Malorkey, R.P. Pautienus and J.C. Bradley, in Guided-Wave Optical and Surface-Acoustic-Wave Devices, Systems and Applications, vol. 239 (SPIE, Bellingham, Washington, 1980), p. 21.
14. J.T. Boyd and D.B. Anderson, IEEE J. Quantum Electron. QE-14, 437 (1978).
15. J.T. Boyd, S. Datta, H.E. Jackson and A. Naumaan, in Integrated Optics, vol. 269 (SPIE, Bellingham, Washington, 1981), p. 125.
16. J.T. Boyd, and C.L. Chen, IEEE J. Quantum Electron. QE-13, 282 (1977).
17. J.T. Boyd, S.H. Chang, C.L. Fan and D.A. Ramey, in High Speed Photodetectors, vol. 272 (SPIE, Bellingham, Washington, 1981), p. 98.
18. R.C. Williamson in 1974 Ultrasonics Symposium Proceedings (IEEE, New York, 1974), p. 321.
19. E.K. Kirchner and J.R. Yaeger in Acoustooptics, vol. 90 (SPIE, Bellingham, Washington, 1976), p. 4.
20. N. Uchida and N. Niizeki, Proc. IEEE 61, 1073 (1973).
21. D.A. Pinnow, IEEE Trans. Sonics Ultrasonics SU-18, 209 (1971).

UNCLASSIFIED

SECURITY CLASSIFICATION OF THIS PAGE (When Data Entered)

REPORT DOCUMENTATION PAGE		READ INSTRUCTIONS BEFORE COMPLETING FORM
1. REPORT NUMBER ESD-TR-82-086	2. GOVT ACCESSION NO. AD A124 305	3. RECIPIENT'S CATALOG NUMBER
4. TITLE (and Subtitle) Solid State Research	5. TYPE OF REPORT & PERIOD COVERED Quarterly Technical Summary 1 May — 31 July 1982	6. PERFORMING ORG. REPORT NUMBER 1982:3
7. AUTHOR(s) Alan L. McWhorter	8. CONTRACT OR GRANT NUMBER(s) F19628-80-C-0002	
9. PERFORMING ORGANIZATION NAME AND ADDRESS Lincoln Laboratory, M.I.T. P.O. Box 73 Lexington, MA 02173-0073	10. PROGRAM ELEMENT, PROJECT, TASK AREA & WORK UNIT NUMBERS Program Element No. 63250F Project No. 649L	
11. CONTROLLING OFFICE NAME AND ADDRESS Air Force Systems Command, USAF Andrews AFB Washington, DC 20331	12. REPORT DATE 22 November 1982	13. NUMBER OF PAGES 106
14. MONITORING AGENCY NAME & ADDRESS (if different from Controlling Office) Electronic Systems Division Hanscom AFB, MA 01731	15. SECURITY CLASS. (of this report) Unclassified	15a. DECLASSIFICATION DOWNGRADING SCHEDULE
16. DISTRIBUTION STATEMENT (of this Report) Approved for public release; distribution unlimited.		
17. DISTRIBUTION STATEMENT (of the abstract entered in Block 20, if different from Report)		
18. SUPPLEMENTARY NOTES None		
19. KEY WORDS (Continue on reverse side if necessary and identify by block number)		
solid state devices quantum electronics materials research microelectronics analog device technology	photodiode devices lasers imaging arrays LIDAR system	surface-wave transducers charge-coupled devices acoustoelectric devices waveguide structures
20. ABSTRACT (Continue on reverse side if necessary and identify by block number)		
<p>This report covers in detail the solid state research work of the Solid State Division at Lincoln Laboratory for the period 1 May 1982 through 31 July 1982. The topics covered are Solid State Device Research, Quantum Electronics, Materials Research, Microelectronics, and Analog Device Technology. Funding is primarily provided by the Air Force, with additional support provided by the Army, DARPA, Navy, NASA, and DOE.</p>		

UNCLASSIFIED

SECURITY CLASSIFICATION OF THIS PAGE (When Data Entered)

DATE
LME